Spherical Fly's-Eye Lens Antenna System for Wireless Communications & Sensing

Nick van Rooijen

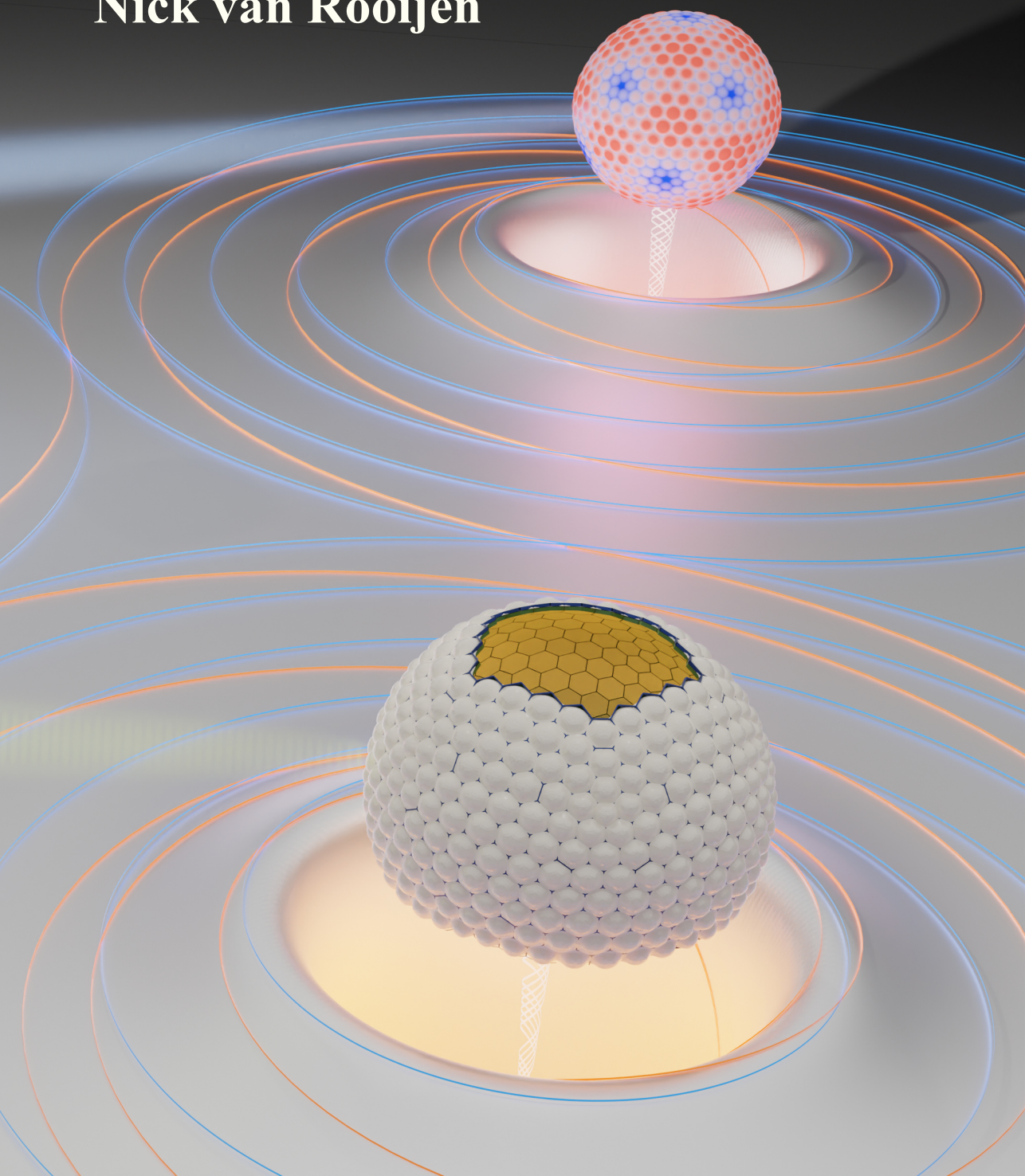

Spherical Fly's-Eye Lens Antenna System for Wireless Communications & Sensing

Spherical Fly's-Eye Lens Antenna System for Wireless Communications & Sensing

DISSERTATION

for the purpose of obtaining the degree of doctor
at Delft University of Technology
by the authority of the Rector Magnificus, Prof. dr. ir. H. Bijl,
Chair of the Board for Doctorates,
to be defended publicly on
Tuesday, 28 April 2026, 12:30

by

Nick VAN ROOIJEN

This dissertation has been approved by the (co)promotors.

Composition of the doctoral committee:

Rector Magnificus,	Chairperson
Prof. dr. ing. N. Llombart Juan	Delft University of Technology, promotor
Dr. ing. M. Spirito	Delft University of Technology, promotor
Dr. ir. M. Alonso del Pino	Delft University of Technology, copromotor
Independent members:	
Prof. dr. ing. A. Neto	Delft University of Technology
Dr. A. Clemente	CEA-LETI, France
Prof. Dr. -Ing. T. Kürner	Technische Universität Braunschweig, Germany
Prof. Dr. S. Monni	TNO, The Netherlands
Prof. dr. ing. L.C.N. de Vreede	Delft University of Technology, *Reserve member*

The work presented in this dissertation has been performed at Delft University of Technology, and financed by Huawei Technologies Sweden AB, under the Grant YBN2020045031.

Keywords:	antenna system, D-band, multi-beam, lenses, 6G, front-end integration, leaky-wave
Cover design:	Impression of a futuristic Fly's Eye system for telecommunications and radar. Cover design by N. van Rooijen using open-source software Blender.
Printed by:	Ipskamp Drukkers B. V., Enschede – The Netherlands

An electronic version of this dissertation is available at https://repository.tudelft.nl/

To my parents

Contents

Summary

Wireless Radio Frequency (RF) systems have revolutionized the way we transmit and receive information from mobile platforms. In recent decades, the number of applications relying on wireless technologies, including telecommunications, radar, and sensing, have exploded. RF engineers have pushed the technological boundaries to feed our appetite for more information through the wireless networks.

However, congestion in the low-frequency radio spectrum means that applications are in a continuous battle to be as spectrally efficient in the frequency bands allocated to them. This strategy has worked well for many wireless generations, but has added considerable challenges due to increased system complexity and decaying energy efficiency.

A promising alternative is the search for larger spectral real estate, where only moderate modulation orders are required. This frequency bandwidth is readily available above 100 GHz, where swaths of unlicensed spectra with limited atmospheric absorption are waiting for novel applications. By tapping into this unused resource, the next generation of mobile communications and sensing could unlock near unconstrained data rates or time resolutions. The high carrier frequencies furthermore enable miniaturization of the antenna systems, which in turn allows compactness for as yet unimagined applications.

Unfortunately, developing wireless systems at such frequencies is quite challenging. The shrinking wavelengths at D-band frequencies require a radical redesign of our wireless systems and networks. Integrated circuit technologies, despite showing promising developments, cannot yet offer good enough performance to overcome the large free-space propagation spreading loss at these wavelengths. High-gain, wideband antennas with narrow beams appear to be the go-to solution to meeting link budget requirements. For these antennas to be commercially successful, novel technologies for low-cost antenna packaging, integration and fabrication, and innovative antenna architectures are therefore necessary. This thesis addresses many of these challenging aspects for D-band antenna systems, and is separated into three parts.

First, a wideband high-gain lens antenna architecture is proposed, designed to be compatible with fully integrated antenna front-ends. Its feeding antenna is positioned

on a low-loss fused-silica interposer. Then, a dual-lens consisting of a high permittivity 'core' lens and a low permittivity 'shell' lens is introduced to achieve both a high front-to-back ratio with the lens feeding antenna, as well as increased degrees-of-freedom for antenna shaping. The combination of fused-silica interposer technology, and the high-density core lens, enables the propagation of leaky-wave modes, which in turn allow for highly efficient illumination of an electrically large shell lens. This elliptical shell lens is what delivers the high directivity to the free-space medium. Then, to better integrate the spherical core lens, a novel flat core lens architecture was developed and fabricated. This novel core lens design is electrically spherical, but provides a physically flat interface. The resulting core lens is very compact (less than 6 mm in diameter), and could potentially fit inside the RF packaging, thereby unlocking novel integrated lens solutions.

Then, the thesis shifts its focus towards the development of Quasi-Optical (QO) techniques for the characterization of antennas and materials. The first QO measurement contribution focuses on sub-THz probe-fed antennas, that are particularly challenging due to their sensitive mechanical and electromagnetic properties. A QO near-field measurement strategy is developed for accurate characterization of these high-gain probe-fed antennas in a planar mechanically scanned setup. Calibration and modelling techniques allow for an accurate measurement of antenna reflection-coefficient, directivity and gain. Experimental data were presented, validating the proposed approach and characterization bench. The second QO measurement contribution was made to advance the field of sub-THz material characterization. A waveguide-based, lens antenna architecture was proposed that achieves high-efficiency near-field coupling, and allows for QO Thru-Reflect-Line calibration. Wideband performance could be obtained, generating inhomogeneous plane-waves with high Gaussicity and low field spreading effects due to the high-density dielectric lens materials. Two materials-under-test were studied in full-wave simulations, indicating good characterization capabilities of the QO measurement setup.

Finally, the thesis aims for full system integration, where the developed antenna elements are now incorporated into a Fly's-Eye antenna system with hemispherical coverage. It does so by first presenting a full system-level optimization of the Fly's-Eye array topology and geometry. A novel conformal lens array architecture based on the Goldberg icosahedron is presented, together with a computationally efficient optimization method. Such optimization is performed over the full far-field hemisphere in terms of pattern uniformity, directivity and interference. The icosahedral design enables a great reduction of the number of unique elements due to the 60-fold symmetry planes. This way, improved potential for mass-fabrication and lower cost is unlocked. Next, a chapter is dedicated to the characterization of wideband flip-chip interconnects using high-accuracy Thru-Line-Reflect calibration techniques. The flip-chip components were found to be wideband and low-loss, paving the way for low-loss front-end integration with minimum impact on system performance. They enable

the full integration of D-band RF integrated circuitry on the fused-silica interposers. The latter is described in the final chapter, where the work-in-progress on front-end design strategy and fabrication is presented, demonstrating the feasibility and current challenges of the technological implementation.

Samenvatting

Draadloze Radio Frequentie (RF) systemen hebben de manier waarop we informatie versturen en ontvangen vanaf mobiele platformen gerevolutioneerd. De laatste decennia is het aantal toepassingen die afhankelijk zijn van draadloze technologieën, waaronder telecommunicatie, radar, en waarneming, enorm toegenomen. RF-ingenieurs hebben de technologische grenzen steeds opgeschoven, om ons van de groeiende vraag naar draadloze informatie te voorzien.

Echter, congestie in het laagfrequente radiospectrum, betekent dat applicaties continu in strijd zijn om zo efficiënt mogelijk om te gaan met de bandbreedte die hen is toegewezen. Deze strategie heeft voor vele draadloze technologische generaties gewerkt, maar staat nu onder druk door toenemende uitdagingen. Met name de verhoogde systeemcomplexiteit en de verminderde energie-efficiëntie zorgen voor problemen in verdere groei.

Een veelbelovend alternatief is het zoeken naar meer spectraal bandbreedte, waarmee met een verminderde modulatiegraad een gelijkwaardige of hogere datasnelheid kan worden bereikt. Deze bandbreedte is verkrijgbaar bij frequenties boven 100 GHz, waar ongelicenseerde bandbreedte met beperkte atmosferische absorptie wacht op nieuwe applicaties. De volgende generaties van mobiele communicatie en waarneming zouden met deze bandbreedte ongeëvenaarde datasnelheden en tijdsresoluties kunnen behalen. De hogere draagfrequentie met kortere golflengte, zou bovendien verdere miniaturisering van antenne systemen mogelijk maken, wat bijdraagt aan nieuwe compacte toepassingen.

Helaas is het ontwikkelen van draadloze systemen bij zulke hoge frequenties niet zonder uitdagingen. De kortere golflengtes boven 100 GHz frequenties vereisen een radicaal herontwerp van onze draadloze systemen en netwerken. Ondanks de veelbelovende ontwikkelingen in geïntegreerde schakelingen zijn de prestaties van deze schakelingen op deze frequenties nog niet voldoende om de grote verliezen door propagatiespreiding te overbruggen. Antennes met grote bandbreedte en hoge versterking, die dunne radiatiepatronen hebben, worden als oplossing gezien om alsnog het benodigde vermogensbudget te behalen. Om deze antennes commercieel succesvol te laten zijn, zijn nieuwe antenne technologieën en architecturen voor goedkope verpakkingen,

integratie en fabricage nodig. Deze doctorale thesis kaart veel van deze uitdagende aspecten voor hoogfrequente antenne systeem aan, en is onderverdeeld in drie delen.

Allereerst wordt een breedbandige lensantenne met hoge versterking geïntroduceerd. Deze lens is ontworpen om compatibel te zijn met een volledig geïntegreerde elektronische koppeling. De voedingsantenne is gepositioneerd op een intermediair kwartsglas met laag verlies. Een duale lensarchitectuur met een hoge permittiviteit 'kernlens' en lage permittiviteit 'omhulsellens' wordt gepresenteerd, waarmee zowel een hoge voor-achterverhouding kan worden behaald met de voedingsantenne, alsmede een toename in het aantal vrijheidsgraden in antennevormen. De combinatie van intermediair kwartsglas en de hoge dichtheid kernlens laat de propagatie van lekgolfmodi toe, waarmee hoogefficiënte illuminatie van de omhulsellens mogelijk is. Deze elliptische omhulsellens zorgt voor de verhoogde directiviteit in het vrije-ruimtemedium. Vervolgens, om de sferische kernlens beter te kunnen integreren met het antennesysteem, wordt een nieuwe vlakke kernlensarchitectuur ontwikkeld en gefabriceerd. Dit nieuwe ontwerp is elektrisch sferisch, maar fysiek vlak. De resulterende kernlens is met minder dan 6 mm diameter erg compact, en kan daardoor potentieel in RF-verpakkingen passen, waardoor nieuwe geïntegreerde lenstoepassingen mogelijk worden.

Vervolgens schuift de thesis de aandacht richting het ontwikkelen van Quasi-Optische (QO) technieken voor het karakteriseren van antennes en materialen. De eerste bijdrage aan QO-meetopstellingen gaat over het meten van sub-THz antennes gevoed door sondes, die bijzonder uitdagend zijn om te meten door de gevoelige mechanische en elektromagnetische eigenschappen. Een QO meetstrategie in het nabije-veld is ontwikkeld voor het nauwkeurig karakteriseren van deze sondegevoedde antennes met hoge versterking in een vlakke mechanisch gescande meetopstelling. Kalibratie- en modelleertechnieken zorgen voor een accurate meting van zowel antennreflectiecoëfficiënt en directiviteit als antenneversterking. Experimentele data wordt gepresenteerd, waarmee de voorgestelde aanpak en opstelling worden geverifieerd. De tweede contributie richting QO metingen wordt gemaakt binnen het kader van sub-THz materiaalkarakterisatie. Een op golfgeleider gebaseerde lens antenne architectuur wordt gepresenteerd, wat een efficiënte koppeling in het nabije-veld kan behalen, en daarmee een hoog accurate QO 'door-lijn-reflect' kalibratie mogelijk maakt. Breedbandige prestaties kunnen hiermee worden behaald, waarmee inhomogene vlakke golven met hoge Gaussiciteit en lage veldverspreidingseffecten kunnen worden gegenereerd dankzij de hoge diëlektrische dichtheid van de lenzen. Twee testmaterialen worden vervolgens bestudeerd in volledige golfsimulaties, en geven goede karakterisatie-eigenschappen van het QO-systeem aan.

Tot slot richt de thesis zich op de integratie van een compleet antennesysteem, waarbij de ontwikkelde individuele antenne-elementen nu geïntegreerd worden in een Fly's-Eye-antennestelsel met hemisferische dekking. Om dit te bereiken, wordt eerst een volledige optimalisatie van de Fly's-Eye-topologie en -geometrie op systeem niveau

geïntroduceerd. Een nieuwe conformele lens-antennentelselarchitectuur gebaseerd op een Goldberg icosaëder wordt gedemonstreerd, samen met een rekenkundig efficiënte optimalisatiemethode. Deze optimalisatie over de gehele verre-veldhemisfeer, is gebaseerd op uniformiteit van het stralingspatroon, directiviteit en interferentie. Het gekozen icosaëderontwerp biedt een grote reductie in het aantal unieke antenne-elementen door haar 60-voudige symmetrievlakken. Hierdoor is er een grotere potentie voor massafabricage en verminderde kosten, ten opzichte van ontwerpen met minder symmetrievlakken. Hierna wordt een hoofdstuk toegewijd aan het karakteriseren van breedbandige 'flip-chip' interconnecties met hoge accuratesse 'door-lijn-reflect' kalibratietechnieken. De flip-chip componenten zijn gekarakteriseerd als breedbandig met laag verlies, en hebben daardoor een beperkte negatieve invloed op de algehele prestaties van het Fly's-Eye systeem. Met de flip-chip kunnen de geïntegreerde RF-schakelingen op het kwartsglas worden geplaatst. Deze en andere integratiestappen worden beschreven in het laatste hoofdstuk, waar de ontwerpstrategie en fabricage van het ontwerp worden gedemonstreerd om zo de technologische mogelijkheid en huidige uitdagingen van het ontwerp aan te tonen.

Preface

This dissertation describes the research work carried out at the Terahertz Sensing Group, Department of Microelectronics, Delft University of Technology, over a period of four years (from July 2021 to July 2025). The research shown in this dissertation was supported by HUAWEI Sweden AB, under the contract YBN2020045031. Parts of the antenna integration were performed by CITC in Nijmegen, the Netherlands. Machining of metallic and dielectric parts was performed by DEMO, TU Delft. All prototypes were measured at the TU Delft, in the Earl McCune / XG Labs.

Nick van Rooijen
Delft, July 2025

Chapter 1

Introduction

1.1. A Brief History of Wireless Telecommunications

MODERN civilization is heavily dependent on efficient information gathering, communicating, and processing. It is in our nature as curious creatures to obtain information, and scientific progress would be more difficult without its efficient flow. The exchange of information over long distances is what we refer to as telecommunications. Nowadays, we take near speed of light communicating for granted. However, for most of our ancestors, telecommunicating has been a troublesome effort, constrained by the laws of nature.

All forms of communication must rely on a transmitter as a source of information, a channel in which an information carrier flows, and a receiver to receive and process such information. If successful, the information received is the same as the one transmitted. Unfortunately, some information is lost due to an unclear transmission, problems at the receiver, or simply lost in the complexities of the channel.

Transmission of information relies on a carrier that can take on many distinct forms. From a homing pigeon carrying letters, where the information is hidden in optical symbols (the alphabet in this thesis), to the gossiping aunt that uses spoken language with audio symbols, where acoustic waves carry the information as it propagates through the air. Unfortunately, both optical and mechanical (acoustic) do not carry our information very far, as such carriers attenuate the waves rapidly due to their physical nature, and are adversely affected by weather conditions.

To escape these constraints, scientists and engineers of the 19th century devised novel techniques and devices to enhance our telecommunication abilities. The electrical telegraph, arguably the most revolutionary invention in the field of telecommunications, made reliable communications over vast distances possible. Such an electric carrier enables near speed of light (299,792,458 meters-per-second)

communications, almost independent of weather conditions. While today we use optical fibers as our information backbone, such networks would still be dependent on metal or glass connections were it not for the wireless communication revolution in the 19th and 20th centuries.

Critical to this revolution was the revelation of nature's connection between electric fields, magnetic fields and light, as theoretically unified in the famous Maxwell's equations. These equations made the invisible parts of the electromagnetic spectrum, what we now call 'radio' waves, visible to those equipped with the right mathematical tools. Contrary to mechanical waves, electromagnetic waves do not rely on a medium for propagation, and can propagate even in vacuum. Such waves have highly beneficial properties for communicating over vast distances, and their interaction with matter could now be mathematically predicted, opening up possibilities for radio detecting and ranging (radar) and unique sensing applications.

The interface between our electrical devices and the free-space radio waves are known as antennas, and are vital for achieving efficient radio links. The first antennas were relatively simple metal rods or wires that converted the electromagnetic waves into electric currents, and vice versa. Because the electromagnetic waves spread spherically as a function of distance, the majority of their intensity (or power) is lost before it reaches the receiver. Progress made in the scientific field of antennas has led to antennas that are much more energy efficient, by shaping its radiative patterns according to the application's strict demands.

In parallel, advancements made in electronics enabled the generation, amplification and detection of faint electrical signals. While the list of electrical inventions required to reach today's wireless networks is too extensive for this thesis, it is in particular the invention and continued developments of the Integrated Circuit (IC) semiconductor transistor, that enabled the miniaturization and compact amplification of the faint electromagnetic signals. This has enabled the transmission of information over long-distance channels, whilst being integrated in compact everyday devices.

However, all these developments would have been fruitless without a fundamental understanding of information itself. Developed halfway the 20th century, Claude Shannon provided a mathematical framework for the modern information theory. The famous Shannon-Hartley theorem [1] provides a theoretical upper bound to the speed (in bits per second) at which information can flow over a channel, provided the average signal power and average noise power, both observed over the channel bandwidth. The ratio of signal-to-noise-power lies at the heart of any wireless system; An increase in bandwidth is directly proportional to the information-carrying capacity of such a system. For telecommunication applications, the shorter symbol duration leads to an increased wireless data capacity. For radar systems, the decreased pulse time leads to an improved range resolution. As such, most RF systems would benefit greatly from an increased RF bandwidth.

Today, developments in wireless communication and sensing have revolutionized our modern world. By enabling the transmission (TX) and the reception (RX) of information over vast distances, Radio Frequency (RF) technologies have unlocked an explosive number of applications varying across a wide range of topics. Examples include but are not limited to telecommunications, military or civilian radar, to earth or space observation. Unfortunately, spectral bandwidth is a limited resource, particularly in the heavily congested low-frequency spectrum. This has led to increased competition in bandwidth allocation between different applications. Furthermore, the rising electricity consumption of our wireless systems, together with the continued demand for increased data rates is leaving modern-day scientists and engineers faced with serious challenges in providing continued sustainable growth. This thesis hopes to be a very small part of an improved wireless world.

1.2. Wireless technologies beyond 100 GHz

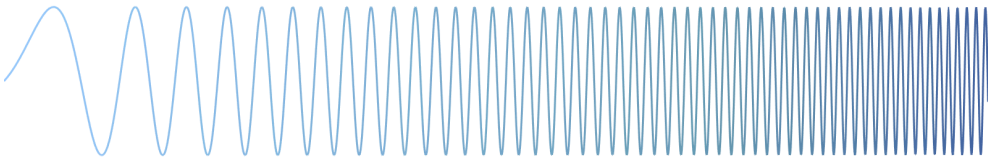

LARGE efforts have pushed wireless systems to become more spectrally efficient. Advanced modulation techniques have enabled bandwidth-limited communication systems to still obtain impressive data rates, generally at the cost of power efficiency [2]. The growing demand for higher-order modulation techniques require higher SNR and linearity, thereby increasing complexity and DC power consumption.

A different approach could be to use less complex transceivers with only moderate spectral efficiencies, and instead focus on obtaining Ultra-Wideband (UWB) spectra [3]. This drive towards higher frequencies has pushed researchers to much higher carrier frequencies. In particular, wireless network development is showing a great interest towards submillimeter-wave frequencies above 100 GHz. The D-band, ranging from 110 GHz to 170 GHz, presents an abundance of unlicensed spectrum, that is attenuated by only limited atmospheric absorption [4]. The increase in bandwidth using these spectral bands can enable short-range wireless channels with large data throughput. Such high data throughputs and resolutions allow for new, as yet unimagined applications [5]. For these reasons, the D-band is targeted for the 6^{th} generation of wireless communications, known as 6G.

Because of these promising new opportunities, the D-band has been an active topic of extensive research. Recent implementations demonstrate that this frequency band is no longer science fiction, as many studies have reported data rates of over 100 Gb/s [6]. In [7], a peak data rate of 200 Gb/s was achieved, albeit at a short 15 cm range. For radar, UWB radar operating between 126–182 GHz is shown to achieve 2.7 mm range resolution [8]. Such technologies could potentially even be combined into an Integrated Sensing And Communicating (ISAC) wireless system [9], thereby further enabling applications that are science fiction to us now.

While these studies demonstrate the potential for D-band wireless systems, unlocking the full potential of the sub-THz band with $>$ 1000 Gb/s transfer speeds over distances $>$ 500 m has not yet been fulfilled [6]. As will be demonstrated in the next section, there are still many challenges to address in order to achieve full technological scalability and economic success for sub-THz wireless systems.

1.2.1. Challenges for D-band Antenna System Design

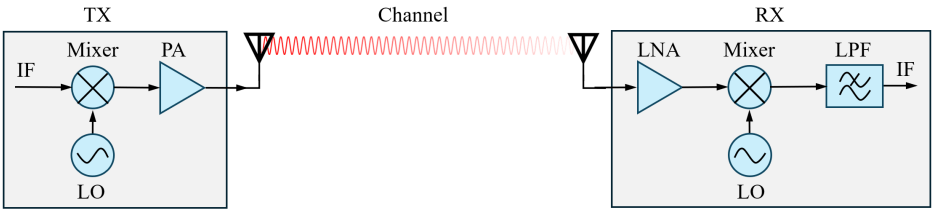

Figure 1.1: Typical RF system block diagram for TX (left) and RX (right).

Unfortunately, these high carrier frequencies also provide a large set of challenges for antenna systems. These challenges come in the form of physical, technological, and economic boundaries, all linked to the increasingly shorter wavelengths at sub-THz spectra. As we will see, the implementation of these technologies over UWB frequency ranges remains difficult, as high performances must be attained throughout the RF system [2]. This section will briefly outline several of these challenges, by providing a birds-eye-view of the isolated wireless system components.

Fig. 1.1 shows an overview of a typical TX-RX front-end architecture, adapted from [10]. On the left side, there is the TX that mixes the Intermediate Frequency (IF) signal with the Local Oscillator (LO), to generate the upconverted RF signal. The RF signal is then amplified by the Power Amplifier (PA), and is sent to the antenna for transmission over the wireless channel in which the electromagnetic fields must propagate. On the right, there is a generalized RX topology that receives the RF signals from the antenna. These signals are passed through a

Low-Noise-Amplifier (LNA), and is then downconverted to IF by mixing with the LO.

As an overview, we will go through the most common challenges found in each of these building blocks separately. Note, however, that while low-frequency RF systems could practically consider the components inside TX and RX as existing in isolation, $>$ 100 GHz wireless systems enforce co-design between the different components. Problems such as excessive thermal build-up or mutual coupling will not only affect the discussed component, but all other components inside the integrated antenna system. This makes the field truly challenging, as the antenna designer is forced into the role of complete system designer. A final set of challenges is found in the high-frequency characterization of all these antennas, RFICs, interconnects, and materials in general. This topic will be touched upon in the final subsection.

D-band Integrated Circuit

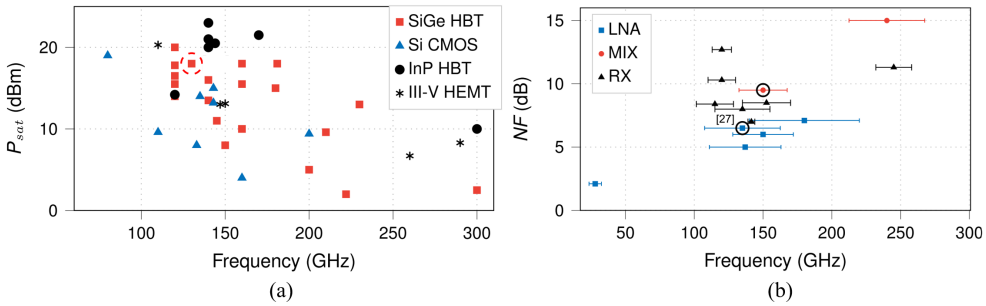

Figure 1.2: (a) Literature overview of the saturated output power of a power amplifier for TX, studied for various IC technologies. Taken from [11]. (b) Similar study but now for the receiver noise factor for RX. Also from [11].

One of the current main limiting factors for D-band wireless systems are the available Integrated Circuit (IC) technologies. In particular, the technology-dependent transistor switching speed presents a key bottleneck towards high-frequency system performance. As the carrier frequencies approach the commonly used $f_T/f_{\max}$ metric, a decrease in Power-Added Efficiency (PAE) is obtained [2]. Such decrease in efficiency results in thermal issues in the ICs, and a reduction in the already power-limited high-frequency devices.

On the TX side, this is particularly problematic for the PA, the component that is commonly associated to the largest DC power consumption in a transceiver chain [12]. Fig. 1.2a shows an overview of the PA saturated output power P_{sat} for D-band frequencies across different IC technologies. While P_{sat} can be increased by

integrating for example Indium Phosphide (InP) Heterojunction Bipolar Transistors (HBTs), such IC technology does not integrate well with digital IC techniques, and presents difficult economic scaling. Therefore, silicon-based technologies are preferred for their integration capability with high volume and relatively low costs [13]. Unfortunately, their P_{sat} is limited to only 18dBm, with a PAE of only 12% [11]. To achieve higher P_{sat}, more amplification stages are required, in turn occupying more IC area and consuming more DC power [2]. These problems worsen with more complex modulation techniques, requiring larger linearity, and therefore, increased IC device power 'back-off' with lower PAE [10].

On the receiver side, similar performance degradation due to higher switching frequencies is observed. This is visualized in Fig. 1.2b, where D-band RX Noise Figures (NFs) for the LNA, mixers and receivers are visualized. As shown, the high-frequency NF is more than 3 dB higher compared to their $<$ 30 GHz counterparts [11]. Lowest NF values are reportedly achieved for narrowband systems, where further optimization can be applied [14].

In addition, the higher carrier frequencies also affect numerous other active and passive components. Negative degradation includes higher In-phase Quadrature-phase (IQ) imbalances, LO phase noise, and baseband IF energy efficiency. In [11], the conclusion was drawn that while above-mentioned effects are not fundamentally limited, the total system power efficiency (and therefore related thermal problems), are current technological constraints limiting current developments. Collectively, these factors contribute to a reduction in the overall system link budget.

D-Band Antennas

Due to these performance limitations in current IC technology, alternatives are required to meet system power budgets. The antenna could play a crucial role in providing the sufficient wideband gain required for the wireless link. The channel shown in Fig. 1.1 is where most of the radiated power ends up lost in the atmosphere for non-directive antennas. Instead, by focusing the radiated energy into a narrow beam, more efficient wireless links can be achieved that can potentially fulfill the D-band link requirements. Such a link budget can be mathematically described by the famous Friis' equation for transmission:

$$\frac{P_{\mathrm{RX}}}{P_{\mathrm{TX}}} = G_t G_r \left(\frac{\lambda}{4\pi R}\right)^2 \tag{1.1}$$

where G_{r} and G_{t} are the receiver and transmitter antenna gains, respectively, λ is the free-space wavelength, and R is the propagation distance [15]. The factor $L = (\lambda/4\pi R)^2$ represents the free-space path loss, which can be compensated for by increasingly large G_{t} and/or G_{r}. In [16] the feasibility of also long-range D-band

wireless links was emulated over a distance of up to 2.3 km. Such link could only practically be achieved using 40 dBi gain TX and RX antennas.

Naturally, the question arises how to cover large angular areas using increasingly narrow beams. Here, the highly directive antennas face problems obtaining full hemispherical coverage required for many applications. This problem, known as antenna pattern reconfigurability, is identified as one of the key problems facing future high-gain antenna systems [6]. Particularly challenging applications require (near) omnidirectional coverage, a topic that will be one of the focus points of this doctoral work.

To understand why this is problematic, we have to distinguish between the different types of antenna architectures. These architectures need to be either scalable enough to fit in a multi-beam array, or have (mechanically or electrically) adaptive beam patterns. Although mechanical steering can achieve full omnidirectional coverage, it comes with a number of disadvantages, such as reliability issues, lack of compactness, and slow speed of scanning [6]. In this thesis work, only highly integrated antennas using low-cost materials will be considered. The classes of antennas meeting these requirements in sub-THz domain are broadly defined as lens antennas, phased arrays, reflect arrays, transmit arrays and leaky-wave antennas [6].

Transmit arrays offer simpler electronic front-ends, as the feeding antenna is separated from the array [6]. Low cost, Printed Circuit Board (PCB)-based transmit arrays were presented in [17] and [18] with high gain. However, such arrays suffer from low aperture efficiency, and have limited gain-bandwidth product. Next, a 24×16 slot-array fed by gap-waveguide technology was presented in [19]. Although excellent aperture efficiency is achieved, the gap waveguides have limited bandwidth, making them unsuitable for wideband applications. Lens antennas use their electronically large volumes in order to generate high antenna gains, although this generally comes at the cost of narrow beam steering range [6]. Previous works ([20, 21]) have incorporated feeds with tilted beams to improve their scanning capabilities. Integrated lens antennas based on leaky-wave feeds were presented in [22, 23], and have shown very large operational bandwidth. Still, in literature, the large majority of integrated lens designs are based on waveguide feeds, [22–26], which make the front-end integration more difficult and costly at high frequencies. Finally, in [27], a complete integrated antenna solution with an on-package feed was presented. It achieves a high feed directivity using a 2×2 patch array, at the cost of high feeding network losses. Also, the lens material has high losses, limiting the scalability of the lens to reach >30dBi gains.

Phased-array architectures are commonly envisioned to solve the antenna pattern reconfigurability problem, where electronically scanned beams enable rapid angular switching of the radiation patterns. Their adoption into the > 100 GHz spectrum is slowly becoming more commonplace, with examples including [28]. Furthermore,

such architectures present a solution to the shortcomings in P_{sat}, as they enable superposition of the radiation patterns of many combined elements.

Unfortunately, their scaling to higher frequencies is not without challenges. Traditional phased-arrays require $\lambda/2$ spacing to avoid grating lobes in the far-field radiation patterns. This means that in order to achieve the high antenna gains, many antenna elements are required to create any significant antenna aperture. The element density in turn causes thermal problems that, if left unaddressed, cause components such as the PAs to suffer from reduced performance [2]. This makes scaling towards larger arrays challenging. Furthermore, sub-THz phased-arrays generally suffer from beam-squinting effect, where the main beam pointing angle changes as a function of frequency. Due to this narrowband limitation, only few systems have demonstrated active phased-array beam steering with data rates beyond 10 Gb/s [11]. While True Time Delay (TTD) could one day enable wideband phased-array operation, current implementations suffer from low phase resolution, high insertion loss, and large IC area occupation [11, 14]. Numerous other challenges, such as the losses in feeding networks and digital processing consumption, further complicate (economical) implementation of phased-arrays.

D-Band Integration Technologies

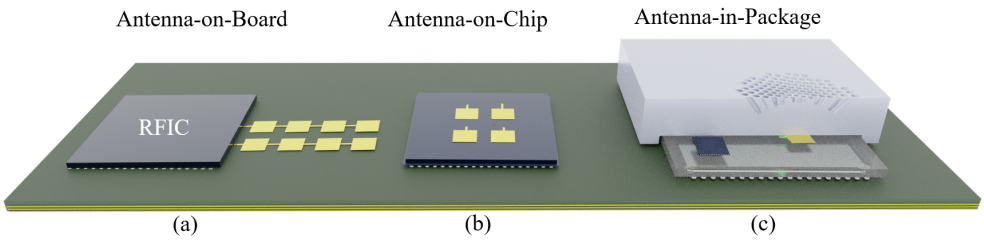

Figure 1.3: Different integration topologies. (a) Antenna-on-board, (b) Antenna-on-Chip, (c) Antenna-in-Package

Next, we briefly discuss another important aspect of the wireless system design. Namely, how to integrate the high-frequency antennas and aforementioned RFIC front-ends together. This is what will be referred to as the RFIC integration technology. In literature, three main classes of techniques are defined, shown in Fig. 1.3. The first, Antenna-on-Board (AoB), is where the antenna is located on a Printed Circuit Board (PCB) technology. This is a fabrication technique known for its low costs, high production scalability, and fast time-to-market [2, 11]. However,

at higher frequencies (such as D-band), significant substrate losses occur due to surface roughness and dielectric loss in board material [13].

The family of technologies that is commonly used is Antenna-on-Chip (AoC), shown in Fig. 1.3b. This architecture relies on high-volume IC fabrication processes with high precision. The advancements of IC miniaturization fit well with the shrinking wavelengths found beyond 100 GHz, as the on-chip antennas fit directly onto the IC itself.

However, AoCs are shown to generally have less gain, typically below 1 dBi [11], due to the usage of more expensive IC area [29]. AoCs can also excite surface waves that negatively impact radiation efficiency [11]. For these reasons, such AoCs are usually combined with high permittivity lenses [11]. However, the high permittivity and substrate height of the ICs present a limiting factor to the radiation efficiency and bandwidth of AoC antennas [2].

As a middle-ground technique, Antenna-in-Package (AiP), shown in Fig. 1.3c, integrates the antenna on a low-loss interposer. By going off-chip, the antenna designer is left with a lot of flexibility in material selection, antenna design and interconnect topology [11]. At D-band frequencies, AiP appears to be the most common solution towards antenna integration [29]. Whilst increasing complexity to assemble the antenna system, AiP enables heterogeneous integration [2, 11], that, as we have seen in Fig. 1.2, might be critical to enable the usage of more powerful and sensitive transceivers, whilst retaining the advanced digital processing capabilities of current silicon-based technologies. However, such switching of IC technologies is only reasonably possible with wideband and efficient interfaces.

One such commonly used interconnect technique is the deployment of gold bond wires, also known as 'wire bonding'. However, such wires become electrically long at D-band frequencies, necessitating the use of compensation structures [11]. A better performing interconnect is the so-called flip-chip interconnect, where the RFIC is connected upside-down (flipped) to the antenna via an intermediary interposer. This technique enables small connection length, resulting in reduced loss, lower parasitics, and therefore, higher bandwidth [2, 11]. Combined with low-loss interposers, such as glass [30], enables wideband and power-efficient integration of multiple MMICs. For these reasons, this architecture will be pursued for the remainder of this thesis.

D-Band Material & Antenna Characterization

Our knowledge on all abovementioned technologies and architectures would not exist without the ability to accurately measure their characteristics. Furthermore, the wireless systems are made up of many different materials, each requiring careful characterization as their performances rely heavily on the properties of the involved materials.

Unfortunately, Device-Under-Test (DUT) characterization is particularly challenging at D-band frequencies, where dynamic range is limited due to a myriad of effects such as cable and interface loss, reduced output power levels [11]. The large bandwidth requires specialized equipment or measurement strategies to obtain sufficient SNR given the high noise floor. Furthermore, due to the short wavelengths involved, measurement and calibration standards are sensitive to fabrication or operational errors. Understanding of all non-idealities of measurement setup and instruments becomes critical to distinguish between errors in measurement and DUT design or fabrication.

For antennas, measurements involve the probing of near- or far-field electromagnetic fields to characterize the radiation patterns. The interface between the D-band antenna and instrument is, in many cases, no longer a cable, but rather an RF landing probe, requiring specialized calibration structures and operator skill for repetitively accurate measurements. In addition, the characterization complexity of these antennas increases drastically when integrated in-package or IC technology, as described in the previous section. Often in such cases, the Antenna Under Test (AUT) is a breakout of the final (fully integrated) system and could be probe-fed to minimize the design of extra interfaces. Furthermore, given the high permittivity of the substrate materials used at these frequencies (i.e., silicon and III-V compounds) the radiation is in most cases realized through the substrate/package, resulting in feeding and the radiating to be opposite one another, resulting in feeding and radiation being opposite to one another as in [31–33].

In [34], various mm-wave probe-fed, backside-radiating, antenna characterization systems are reviewed, with several employing custom suspended probing environment and the use of complex multi-axis robotic arms to perform far-field measurements of the AUT. When high-gain lens antennas are considered, as in this case, these approaches become impractical given the large volume of the setups for reaching the far-field distance. In [31], the mechanical restrictions lead to a phase-less spherical measurement system, which required multiple scans and iterative solver processes, contributing to a lower accuracy of the reconstructed phase. In [33], QO approaches have been employed for backside radiating antennas. Nevertheless, this far-field approach was hampered by strong vibrational coupling between the motorized stage and the RF landing probe. In short, sub-THz measurements are facing challenges in measurement setup and accuracy, and there is not yet a clearly defined road path for such high-frequency antenna measurements.

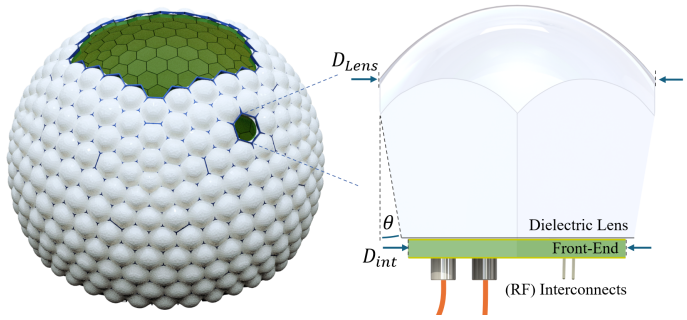

Figure 1.4: Artist impression of the proposed spherically conformal Fly-Eye Array made of high-gain lens antennas. A cross-sectional conceptual view of a single element is shown on the right, visualizing the antenna front-end with its dielectric lens.

1.3. Towards Fly's-Eye Antenna Architectures

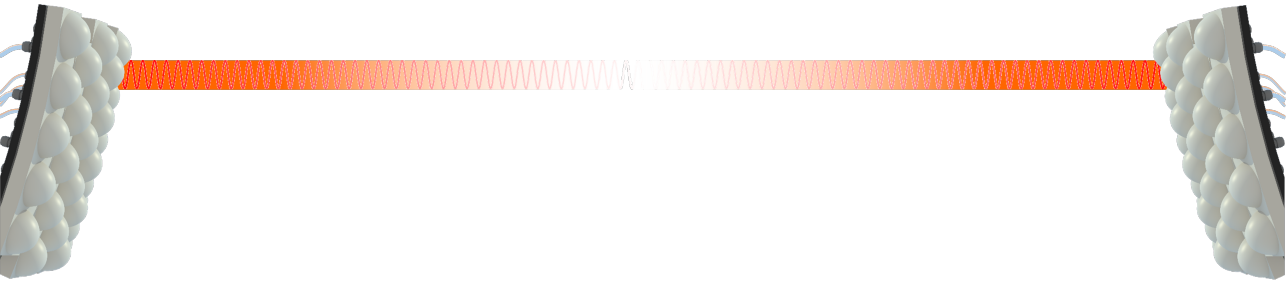

The aforementioned challenges in IC technologies, antennas, integration and characterization will need to be addressed to successfully deploy D-band antenna systems. A Fly's-Eye high-frequency communication system based on lens arrays that generate multiple simultaneous beams was proposed [35]. Fig. 1.4 shows a conceptual view of the Fly's-Eye concept. Contrary to active electronic steering, the Fly's-Eye system relies on passive multibeam combining, where each beam is oriented towards a different part of the field-of-view. This way, potentially full omnidirectional coverage is obtained without the need for complex active beam scanning elements. Furthermore, a low-order modulation scheme is targeted that presents less stringent linearity requirements on the RFIC front-end, enabling higher power efficiency. Combined with a large bandwidth (>20GHz), such Fly's-Eye system could still offer high data throughput.

For such a Fly's-Eye system to work, high-gain antennas (> 30dB) with large bandwidth (> 20 %) are required [22]. Lens antennas have been shown to be a good

candidate for such a system, as they allow for wideband operation (> 20 %), with high radiation efficiencies (> 80 %). Moreover, they enable scalability towards large lens arrays since the electronic front-end could potentially be integrated within the lens footprint, as shown in Fig. 1.4. This latter aspect is very important as it allows modularization of the antenna elements.

We can demonstrate that for any fixed number of antenna elements, the Fly's-Eye and phased-array systems obtain identical SNR performance for each cell when averaged over time. This SNR, demonstrated in Appendix A, results in an expression valid for both the Fly's-Eye and a phased-array systems:

$$\mathrm{SNR}_{\text{Fly-Eye}} = \frac{4\pi N P_e D_r \left(\frac{\lambda}{4\pi R}\right)^2}{\Omega_s k_B T \mathrm{BW}}. \tag{1.2}$$

Fig. 1.5 shows a communication scenario with the above SNR versus distance for various numbers of antenna elements. Depending on the application's required maximum distance, more elements can be added to the Fly's-Eye array, resulting in higher antenna gains. Since the front-ends need to fit below the lens footprint (see Fig. 1.4), the minimum number of elements is dictated by the compactness of the RF electronics.

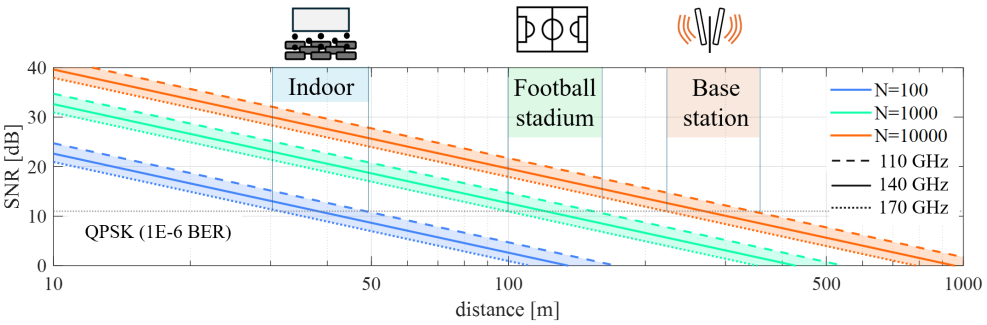

Figure 1.5: Signal-to-noise-ratio versus distance R (in log scale), for various element numbers N. The D-band bandwidth from 110 to 170 GHz is indicated. A minimum SNR for QPSK modulated signals is indicated at 11 dB. The following parameters were used: Bandwidth of 5 GHz, Temperature of 290 K, Rx noise figure 8 dB, G_r 13 dBi and Pt 16dBm.

The scope of this thesis is to continue the developments in sub-THz antennas, specifically at D-band (110 to 170 GHz) and parts of G-band (140-170 GHz), meeting the requirements of Beyond 5G and 6G communication scenarios. This dissertation concentrates particularly on the design of wideband, efficient integrated lenses, that can be fully integrated with RF front-ends. The latter will be targeted in a system demonstration at D-band. Furthermore, the thesis will try to develop new

methodologies and antenna systems for the characterization of sub-THz antennas and materials.

1.4. Scientific Contributions in this Thesis

This doctoral work has made a variety of novel contributions to the scientific communities in the field of antennas and RF characterization. The contributions in design, theory and measurements found in this dissertation are listed below. The referenced publication labels refer to the index in the 'List of Publications' on page 179.

1.4.1. Antenna Technology contributions

- A contribution was made of an integrated core-shell lens antenna. The design incorporated an electrically small core lens composed of dense thermoplastic material, surrounded by a larger shell lens made of low-permittivity material. The shell lens enhanced the antenna gain whilst maintaining low dielectric losses, whereas the compact core lens improves the front-to-back ratio and preserves the spherical wavefront shape. Furthermore, the dual-lens architecture unlocks additional degrees-of-freedom for further lens antenna optimization. This contribution is related to publications J.3, C.3, C.6, C.8 and C.9.

- In order to achieve simpler front-end integration, another contribution focused on adapting the previous lens architecture, by introducing a novel flat-lens design for integrated core-shell lens architectures. The flat lens presents a physically flat interface, that is electrically spherical. This way, the interface between the core and shell lens is planar, allowing for easier lens integration and potential mechanical scanning. This contribution is related to publications C.13 and J.4.

1.4.2. Quasi-Optical Measurement contributions

- A contribution to the Quasi-Optical characterization of probe-fed backside radiating antennas using a near-field planar scanning setup. Calibration and modelling techniques allow for an accurate measurement of antenna reflection-coefficient, directivity and gain. Experimental data of was presented, validating

the proposed approach and characterization bench. This contribution is related to publications C.12 and C.10.

- Further advancements in the field of sub-THz material characterization were made. A waveguide-based, lens antenna architecture was proposed that achieves high-efficiency near-field coupling, and allows for quasi-optical Thru-Reflect-Line calibration. Wideband performance could be obtained, generating inhomogeneous plane-waves with high Gaussicity and low field spreading effects due to the high-density dielectric lens materials. This contribution is related to publication J.5.

1.4.3. System Integration contributions

- A contribution to antenna systems for spherically conformal antenna architecture based on Goldberg polyhedra was made. Such array geometry uses higher-order symmetries to significantly reduce the number of unique antenna elements. An optimization technique was formalized, based on the analytically derived antenna far-field characteristics. The method combines antenna directivity, beam crossover and interference in a computationally efficient way, that enables scaling towards potentially thousands of antenna elements. This contribution is related to publication J.6.

- A two-tier TRL calibration procedure was proposed for characterization of flip-chip interconnection performance was made in another contribution. Complex 2-port S-parameters of the isolated flip-chip interconnects can be extracted and compared with high fidelity with a full-wave simulation. Furthermore, the method allows the calibration reference planes to be further away from the flip-chip transition itself, thereby minimizing potential impact of mutual coupling from the probe landing to the interconnect itself. This contribution is related to publication C.11.

- Design and fabrication efforts in the development of an electronic front-end were made. The front-end combined the fused-silica interposer technology, combined with antenna-in-package techniques for integration with RFICs. The resulting system was then positioned on standard PCB technologies for connectivity with external inputs and outputs.

1.5. Outline of this Thesis

This thesis is structured into three distinct parts. In Part I, two chapters are dedicated to a D-band integrated lens antenna design that can be compactly integrated with RFIC front-end. Chapter 2 presents the design of an integrated core-shell lens design is described using both theory and simulations, leading to working antenna prototypes. Chapter 3 is a continuation of this lens architecture, by introducing a novel core-shell architecture with a flat interface.

Then, to contribute to the challenging high-frequency measurements, Part II introduces novel QO techniques to characterize both antennas and materials in a near-field setup, consisting of two chapters. Chapter 4 presents a QO measurement technique for the measurement and calibration of high-gain probe-fed antennas in a planar near-field setup. This is followed by Chapter 5, where a set of near-field coupled lenses are theorized and designed for use in high-accuracy material characterization.

Finally, Part III aims to integrate the antenna of Part I into a spherically conformal D-band antenna system. To do this, first the proposed front-end architecture is briefly described. Then, a novel antenna array architecture with a rigorous antenna optimization method are presented in Chapter 6. Chapter 7 then provides a high-accuracy methodology for the characterization of flip-chip interconnects, required for the integration of the electronic front-end into the antenna system of previous chapters. Finally, Chapter 8 provides information on the work-in-progress towards an integrated antenna front-end.

I

D-Band Integrated Lens Antenna Design

Chapter 2

Core-Shell Lens for Antenna On-Package Integration at D-Band

This chapter presents a novel dual-lens architecture using an electrically-small, non-diffractive core lens made of dense thermoplastics, and a large shell lens. The electrically-small core lens is fed efficiently by a leaky-wave feed that radiates a spherical wave in the near field. The leaky-wave feed is realized on a glass substrate that can be used as low-loss interposer for on-package antenna integration at D-band frequencies. A prototype using low-cost and mass-production plastic materials with one or two metal layers on a glass substrate has been developed and characterized. The measured prototype shows a directivity of more than 32 dBi and a measured total loss of less than 2 dB over a bandwidth of 30 % and can be used as the array element for future communications systems based on Fly's-Eye antenna architectures.

2.1. Introduction

ENABLING broadband operation and seamless integration between sub-THz antennas and RFIC front-ends is challenging. Conventionally, high permittivity lenses (e.g. silicon) are preferred due to their increased front-to-back ratio (f/b). Moreover, they have low dielectric loss and high scanning capabilities [22, 36]. However, lenses made of silicon together with the possible implementation of anti-reflective layers is quite costly. Other lens materials with high permittivity such as thermoplastics or ceramics are typically lossy [37], or require expensive milling techniques [38]. On the other hand, low-cost plastic lenses with low loss, such as HDPE or Topas, have also been used [22, 23]. Lenses made of those materials suffer from poor integration and scanning capabilities because of their lower critical angle

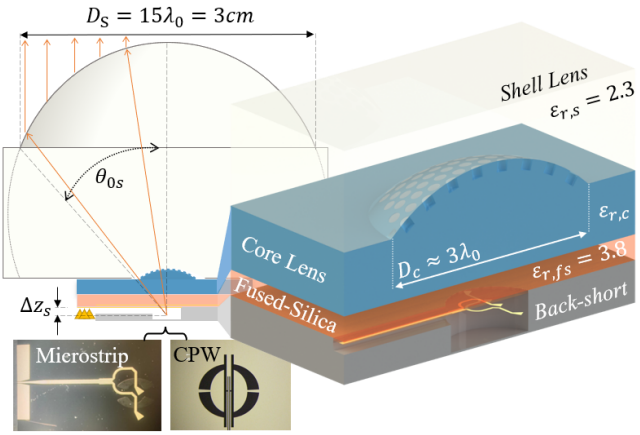

Figure 2.1: Core-shell lens antenna geometry based on an in-packaged leaky-wave feed. The core lens is made of a PREPERM dense material with a sub-wavelength matching-layer. The shell lens is a standard elliptical lens made of HDPE plastic ($\varepsilon_{r,s}$=2.3). The inset shows two in-packaged leaky-wave feed designs, composed of double slots printed on fused-silica wafers ($\varepsilon_{r,fs}$=3.8).

[22]. Lens architectures using novel materials are therefore needed to solve the lens integration problems that are present today.

The objective of this chapter is to develop an integrated dual-lens antenna at D-band that can be used as a low-cost and low-loss array element for Fly's-Eye communication systems [35]. We propose the use of artificially-loaded thermoplastics combined with HDPE to develop a novel core-shell lens antenna architecture. The elliptical shell lens is made of low-permittivity, low-loss and low-cost plastic material (HDPE, $\varepsilon_{r,s} = 2.3$, $\tan\delta = 3.3\text{e-}4$) with a diameter of $D_s = 15\lambda_0$ (3cm) to fulfill the requirements derived in [35]. The elliptical lens has a large eccentricity and therefore suffers from critical angle reflections and poor scanning properties. Therefore, a high-directivity core-lens feed for this lens is used, made of high-permittivity material that has only minimal radiation beyond the shell lens critical angle. Contrary to earlier proposed dual-lens designs, such as [24], the proposed core lens, made of a dense material, is electrically small ($D_c \approx 2-3\lambda_0$) to enable the use of low-cost machinable thermoplastics (PREPERM [39]) with low-loss. This material has different values of permittivity that can be used for the antenna optimization, both as homogeneous lens or GRIN-like design [40].

The core-lens feed is developed using a planar on-package antenna solution. The feeding antenna is based on a leaky-wave stratification realized using a half-wavelength fused-silica ($\varepsilon_{r,fs} = 3.8$, $\tan\delta = 6{\cdot}10^{-4}$) based thin-film technology. Leaky-wave feeds have a well-characterized near-field [41], enabling good illumination of the electrically small core-lens. Furthermore, the fused-silica substrate acts as

a low-loss interposer between the lens antenna and a potential MMIC, as in [30]. The core-lens results in a low-loss and directive feed, transitioning between the PREPERM and HDPE, whilst enhancing the antenna (f/b) and also potentially increasing the degrees of freedom for scanning optimization.

Preliminary simulations of this architecture were presented at earlier conferences in [42, 43]. In this work, we also include the first technological demonstration of a dual-lens integrated antenna at D-band with low-loss performance, and provide an in-depth overview of the design choices with a physical insight on how the core-shell lens works.

Throughout this work, the radiation pattern naming convention is based on the Ludwig-3 definition [44]. The D-plane is the 45° plane, in between the E-plane and the H-plane, whereas the D-plane CX is the cross-polarized component, normalized to the broadside co-polarized component.

This chapter is structured as follows; Section 2.2 provides a detailed design overview of the core-lens. Section 2.3 describes the thin-film on-package antenna design including the feeding network. A fabricated prototype is described in Section 2.4, followed by a brief discussion in Section 2.5.

2.2. Core Lens Design

The core lens design aims at generating a Gaussian-like pattern in the HDPE material to reduce the impact of the critical angle in the shell lens, while facilitating the integration of an in-package planar feed. In this section we describe its architecture and simulated performances.

To feed this core-lens, we introduce a $\lambda_{fs}/2$ fused-silica wafer to act as a resonant Fabry–Pérot/leaky-wave cavity [45, 46], being λ_{fs} the wavelength in the fused-silica medium. The material contrast between the core lens and the fused-silica cavity enables the propagation of a couple of degenerate leaky-wave modes that radiate a Gaussian-like field in the near field with a clean spherical phase front [41]. Since the diameter of the core lens is limited to a few wavelengths, it can be illuminated efficiently by this spherical near field [41]. The core lens can then be shaped following this phase front. To reduce core-shell lens interface reflections, an artificial anti-reflective coating layer is synthesized in the core-lens materials using a new honeycomb-like geometry. In the coming subsections we describe the design in detail, including simulation methodology and the main trade-offs involved.

2.2.1. Leaky-Wave Modes

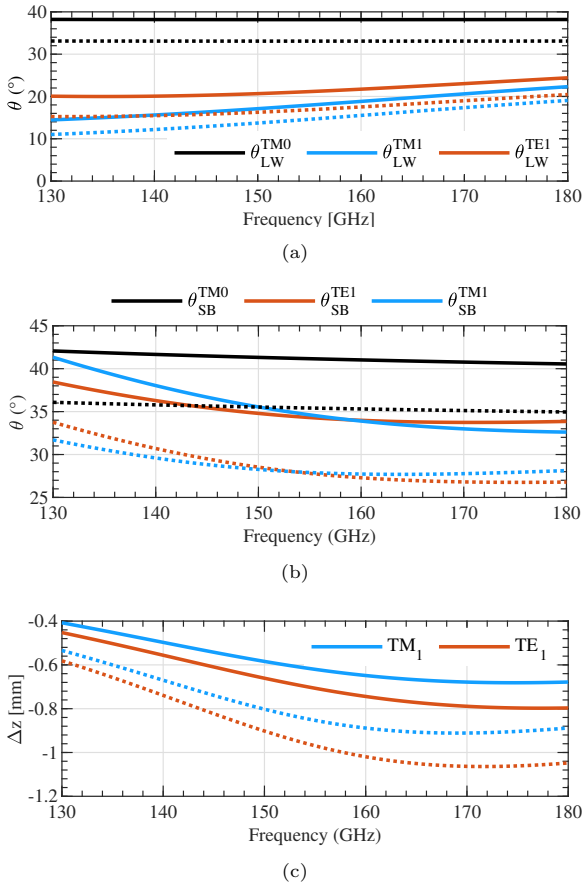

Figure 2.2: Leaky-wave TM_0, TM_1 and TE_1 angle of radiation (a), shadow boundary angle (b), and phase center (c) as a function of frequency. Solid lines indicate $\varepsilon_{r,c} = 9.3$, dotted lines $\varepsilon_{r,c} = 12$.

A resonant cavity made of fused-silica between a ground plane and an infinite dense material is compatible with three leaky-wave modes; TM_0, TM_1 and TE_1 [47] with propagation constants $k_{LW}^{TE/TM} = \beta_{LW}^{TE/TM} - j\alpha_{LW}^{TE/TM}$. Fig. 2.2a shows the angle of radiation for these modes,

Table 2.1

Material Properties Characterized in the 140-200 GHz Frequency Band

Material	Permittivity	Loss tangent	Conductivity (S/m)
Fused-Silica	3.8	6e-4	
Gold			4.1e7
Aluminum			3.53e7
HDPE	2.3	3.3e-4	
PPE400	3.8±0.1	4e-3	
PPE950	9.2±0.15	5e-3±2e-3	
PPE1200	14±0.4	6e-3±2e-3	

$$\theta_{LW}^{TE/TM} = \arcsin\left(\frac{\beta_{LW}^{TE/TM}}{k_0\sqrt{\varepsilon_{r,c}}}\right), \tag{2.1}$$

in case of two dense materials, $\varepsilon_{r,c} = 9.3$ and $\varepsilon_{r,c} = 12$. Around resonance, the TM_1 and TE_1 modes generate a nearly-Gaussian pattern in the infinite medium. A double-slot situated in the ground plane can be optimized for suppressing the TM_0 leaky-wave mode to achieve rotationally-symmetric patterns [47]. The simulated patterns of such double-slot antenna (dimensions given in Fig. 2.3), radiating in infinite dense medium, are shown in Fig. 2.4 for $\varepsilon_{r,c} = 9.3$ and 12. The patterns present good symmetry and low cross-polarization over the 140-170 GHz band. A larger $\varepsilon_{r,c}$ increases the pattern directivity at the cost of antenna bandwidth [22]. The leaky-wave feed achieves a directivity of 14.42 dBi and 15.13 dBi for $\varepsilon_{r,c} = 9.3$ and 12, respectively. As such, the trade-off in $\varepsilon_{r,c}$ is between bandwidth, f/b, and feed directivity. For the considered bandwidth of 30% this corresponds to a ratio $\varepsilon_{r,c}/\varepsilon_{r,fs} \approx 4.5$ leading to $\varepsilon_{r,c} \leq 15$.

This generated Gaussian-like beam will couple well to an integrated lens made of this dense medium as demonstrated in [36] for silicon. However, silicon is expensive for large volumes and the use of a large PREPERM lens will lead to very high loss. Therefore, we introduce an electrically small core lens in the next section. The core lens material choice of $\varepsilon_{r,c} = 9.3$ is based on the PREPERM characterization of Appendix B, as summarized in Table 2.1. The PPE950 material was more constant over a number of measurements taken at different sample locations than the PPE1200 material.

2.2.2. Spherical Core Lens

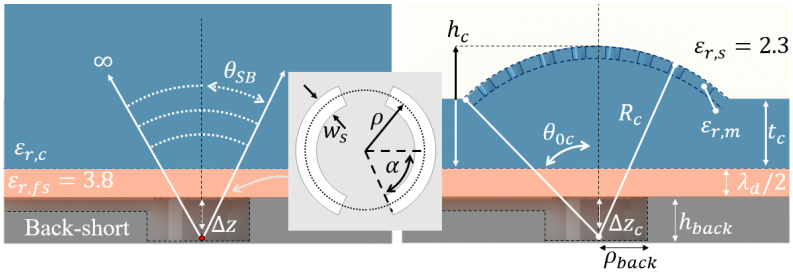

Figure 2.3: Left stratification shows the infinite dense medium with a spherical wave emanating from the phase center at -Δz. Right figure shows the final core lens made of PPE950 with radius R_c of 3.2mm. The core lens is truncated with angle θ_c of 44° and has Δz of -0.7mm. Finally, the inset shows the double slot geometry with the parameters w_s=60 µm, ρ=300 µm and α=67° for the width, radius and slot angle, respectively. The slots are excited by a discrete edge port in the center of each the slot. The back-reflector has parameters h_{back}=800 µm and ρ_{back}=950 µm95.

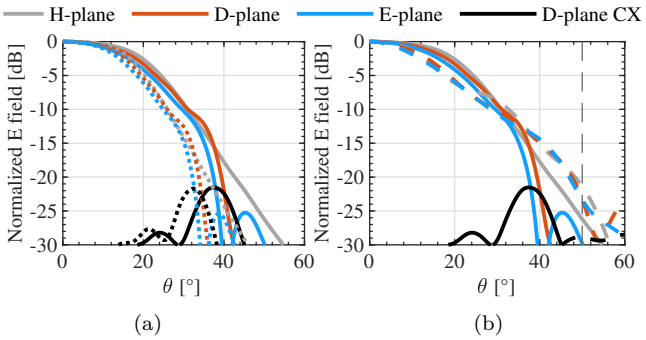

Figure 2.4: (a) Primary pattern comparison at 155 GHz between the $\varepsilon_{r,c}$=9.3 medium (solid) and the $\varepsilon_{r,c}$=12 (dotted), using a standard double-slot feeding antenna shown in Fig. 2.3. (b) Comparison between the patterns in infinite dense medium ($\varepsilon_{r,c}$=9.3) (solid) and those including the core lens (infinite. $\varepsilon_{r,c}$=2.3) in dashed. The vertical dashed line is the shell lens critical angle.

The scope of the core-lens is to radiate a similar Gaussian-like beam generated by the leaky-wave feed to the HDPE plastic medium of the shell lens. The wave emanating from the phase center at Δz_c, can be assumed to be spherical up to a certain angle θ_{SB} [41], known as the shadow boundary angle (see Fig. 2.3 left). The shadow boundary angle is shown in Fig. 2.2b for the corresponding stratifications, and was evaluated using the following equation:

$$\theta_{SB}^{TM/TE} = \Re\{\beta_{LW}^{TE/TM}\} + \arccos(\operatorname{sech}(\Im\{\beta_{LW}^{TE/TM}\})). \tag{2.2}$$

As expected, denser mediums lead to a smaller shadow boundary angle. Because of the spherical nature of the fields, we can make the core-lens spherical with its center at Δz_c until this shadow boundary angle. Then, the incident phase-front will be conformal to the lens surface, thereby conserving relative pattern shape as the field propagates through the core-lens surface. This implies that the shape of the Gaussian-like pattern after the core lens into the HDPE medium resembles that from the infinite $\varepsilon_{r,c}$ medium, as shown in Fig. 2.4b. The frequency variation of the TE_1 and TM_1 phase center for the considered stratification is shown in Fig 2.2c. It was evaluated using the equation proposed in [41] as follows:

$$\frac{\Delta z^{TM/TE}}{\lambda_0} = -\frac{\arctan\left(\sin^2\theta_{SB}^{TM/TE}\right)}{2\pi\sqrt{\varepsilon_{r,c}}\left(1-\cos\theta_{SB}^{TM/TE}\right)} \tag{2.3}$$

We can now describe the core lens geometry using Δz_c, $\theta_{SB}^{TM/TE}$, as well as its cross-sectional radius R_c, spanning from the phase center to the upper surface, as shown in Fig. 2.3. On top of the core lens, we will use a matching layer to reduce possible reflections. As an example geometry, consider the average TE/TM Δz_c of -0.7mm and shadow boundary angle of 36° at the central frequency for $\varepsilon_{r,c} = 9.3$. Fig. 2.4b compares the fields radiated by this core lens into infinite HDPE (solid) to the ones of $\varepsilon_{r,c} = 9.3$ (dashed) medium. The two fields show good agreement, confirming the validity of the spherical geometry choice. Fig. 2.5a visualizes the E-field propagation through the core lens, indicating that the radiation solid angle is roughly maintained through the core lens, whereas the propagation speed increases when entering the less dense medium. The directivity of this core-lens feed is 14.6dBi, thereby preserving the value obtained in the infinite medium of Section 2.2.1. Due to this high directivity of the core lens feed, the majority of power falls within the lens critical angle (indicated in dashed vertical lines in Fig. 2.4b). Without the core lens, the directivity would be only 8dBi.

2.2.3. Core-Shell Design Trade-Offs

The designed leaky-wave feed in combination with the high-dielectric core lens radiates a Gaussian-like pattern into the HDPE dielectric which enables a high-aperture efficiency illumination of the shell lens. Moreover, compared to the architectures in [22, 23], the directivity of this feed is further enhanced and thus, the impact of the critical angle on a low-dielectric plastic lens is reduced.

In the previous section θ_{SB} and Δz_s have been defined. Now, the core-lens diameter D_c and subtended angle θ_{0c} will be co-designed with the shell lens. The shell lens is an elliptical lens with a diameter D_s, subtended angle θ_{0s} and phase

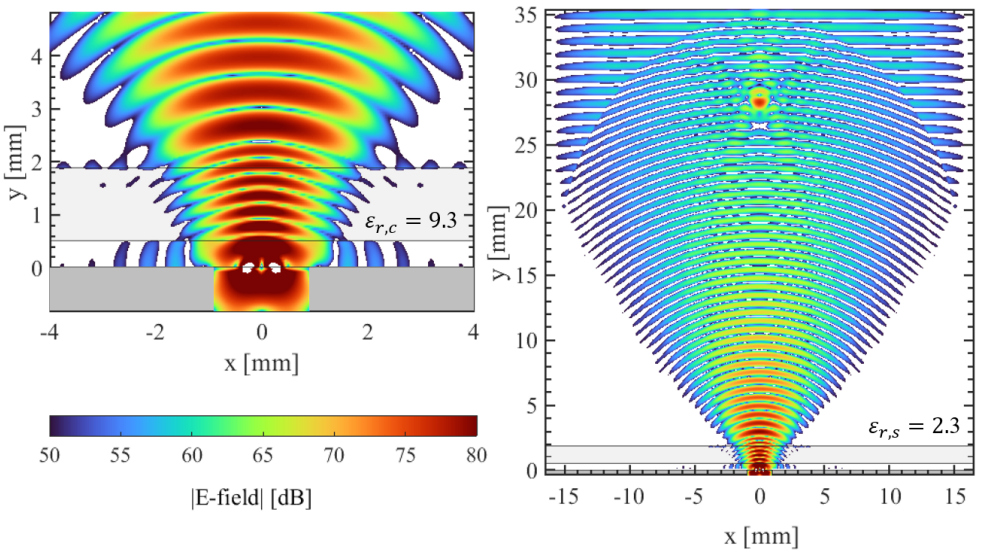

(a) (b)

Figure 2.5: (a) Full-wave simulation of the E-field propagating at 155 GHz through the core lens, matching layer, and infinite plastic medium. Core lens volume is shown in light gray. (b) The same 155 GHz E-field now propagating through the ellipsoidal HDPE lens surface and into the free space medium.

center Δz_s (different from the core lens), as shown in Fig. 2.1. For a lens diameter of $D_s = 15\lambda_0$, corresponding to a directivity of around 32dBi, the shell-lens and core-lens parameters have been optimized to maximize the overall aperture efficiency, η_{ap}, over the bandwidth of 140-170 GHz. The aperture efficiency has been calculated from the combination of full-wave simulations of the core-lens in combination with Fourier optics tool as in [48].

First, θ_{0c} is optimized in terms of η_{ap}, whilst simultaneously also optimizing shell-lens parameters θ_{0s} and Δz_s. Fig. 2.6 shows the η_{ap} optimized for three values of θ_{0c}, when $\theta_{0c} = \theta_{SB}$ and two cases where $\theta_{0c} > \theta_{SB}$. As shown in the figure, θ_{0c} needs to be larger than θ_{SB} to increase the aperture efficiency in the lower part of the frequency band, where θ_{SB} is larger (Fig. 2.2b). However, further increasing the θ_{0c} does not achieve a higher aperture efficiency. Moreover, it also becomes more challenging to fabricate, since the core-lens thickness t_c (Fig. 2.3) decreases with increasing θ_{0c}. Therefore, $\theta_{0c} = 44°$ provides the optimum trade-off and will be used for the next optimization.

Secondly, the diameter of the core-lens D_c should be minimized to reduce the dielectric loss in the PREPERM material. However, larger diameters are easier

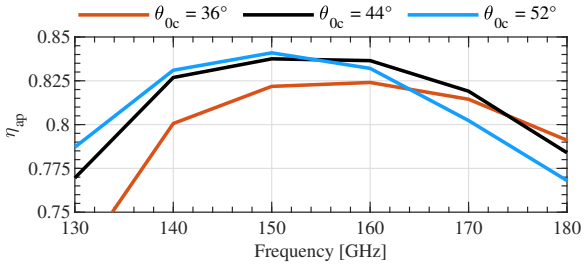

Figure 2.6: Aperture efficiency comparison between the different core lens subtended angles θ_{0c}.

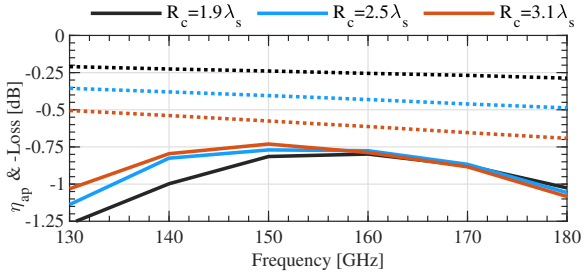

Figure 2.7: Aperture efficiency (solid) and loss (dotted) in dB for different core lens radii.

to fabricate, and reduce the impact of misalignment tolerances. The diameter of the core-lens is defined as $D_c = 2R_c \sin\theta_c$, where R_c is the radius of the core-lens originating from the phase-center as shown in Fig. 2.3. The trade-off between losses and aperture efficiency is presented in Fig. 2.7 for three values of R_c, corresponding to $1.9\lambda_s$, $2.5\lambda_s$ and $3.1\lambda_s$, where λ_s is the wavelength in the HDPE material. As previously, the parameters of the shell-lens θ_{0s} and Δz_s are optimized for each value of R_c. As shown in the figure, low values of R_c indeed lead to lower dielectric loss but also degrade the quality of the patterns at low frequencies. The shrinking thickness $t_c < 1$mm also makes fabrication more difficult. As a trade-off, the core lens was set to a radius of $2.5\lambda_s$ (3.2mm) leading to a t_c =1.26mm and D_c =4.75mm. This core lens is still feasible for fabrication, with acceptable dielectric loss (0.4dB) and high aperture efficiency across the band ($\eta_{ap} > 80\%$).

The fields radiated into the HDPE medium using these optimized dimensions of the core lens are shown in Fig. 2.9 for the low, center, and upper limit of the frequency band. The fields are rotationally symmetric with low cross-polarization levels. The fields are also compared to those radiated into an infinite medium with $\varepsilon_{r,c} = 9.3$. The fields match very well until roughly the shadow boundary angle. The fields radiated by the complete core-shell lens are shown in Fig. 2.9.

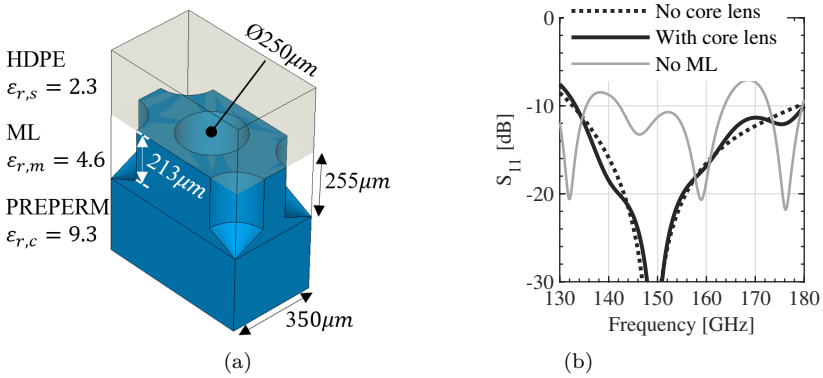

(a) (b)

Figure 2.8: (a) Synthesized matching layer unit cell used for simulations. A conical drill-tip has been included with dimensions defined in the figure. (b) Simulated S_{11} reflection parameter using $Z_0 = 300\ \Omega$ with (solid) and without (dotted) the core lens. The case with core lens excluding a matching layer is shown in solid gray.

2.2.4. Core-Shell Matching Layer

To avoid multiple reflections and their potential impact on the input reflection coefficient, a quarter-wavelength matching layer with permittivity $\varepsilon_{r,m} = \sqrt{\varepsilon_{r,c}\varepsilon_{r,s}}$ is located at the interface between the core and shell lens. Given the core-lens permittivity of $\varepsilon_{r,c} = 9.3$, an artificial permittivity of $\varepsilon_{r,m} = 4.6$ is synthesized by drilling cylindrical holes conformally in the core lens surface, see Fig. 2.1. Compared with a linear grove topology, as in [49], the cylindrical holes support dual-polarization. Moreover, its fabrication is faster, as the holes are drilled instead of milled.

A standard drill bit of diameter 250 µm, corresponding to $\approx 0.4\lambda_c$, defines the diameter of the hole. A short cone is added to the bottom of the cylinder to emulate the drill-bit tip. Because the holes are conformal to the spherical surfaces, the matching layer periodicity was optimized using Floquet mode analysis at broadside incidence, its unit cell shown in Fig. 2.8. Less than −20dB reflection coefficient was obtained using this approach. The reflection coefficient of the spherical core-lens antenna with the anti-reflection layer whilst propagating into the infinite HDPE medium (see Fig. 2.1) is shown in Fig 2.8b. The reflection coefficient follows the same behavior of the double-slot and leaky-wave radiating on the infinite $\varepsilon_{r,c} = 9.3$ medium (also displayed in Fig. 2.8b), showing only minor ripples. The

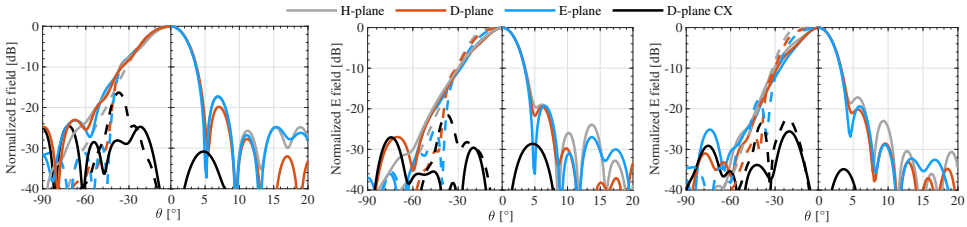

(a) (b) (c)

Figure 2.9: Antenna patterns at 140 GHz (a), 155 GHz (b), and 170 GHz (c). On the negative θ axis, the primary patterns in infinite $\varepsilon_{r,c} = 9.3$ medium are shown in dashed lines, whereas the solid lines show the patterns in infinite plastic medium (with the core lens included). The positive θ axis shows the simulated secondary patterns (in free-space) of the standard double-slot of (Fig. 2.1).

reflection coefficient is below -10dB across the 130-180 GHz band, covering a relative bandwidth of 32%. Also shown in Fig. 2.8b is the S_{11} without a matching layer, significantly affected by the reflections at the core-shell lens interface. Because of the small reflections coming from the core-lens, we can design the on-package planar feed using the simulations with the infinite $\varepsilon_{r,c} = 9.3$ medium, which reduces significantly the computation time.

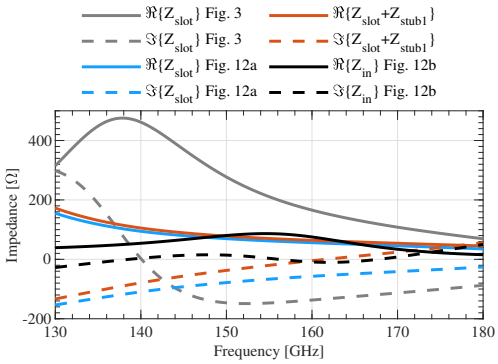

Figure 2.10: Double-slot active impedances. In gray, the standard double-slot with α=67° of Fig. 2.3. In blue, the double-slot with increased α=87° and $w_2 = 2w_1$ tapering of Fig. 2.13a. In red, the same double slot of Fig. 2.13a, but now with stub 1 added. Finally, in black is the input impedance seen at the central port in Fig. 2.13b.

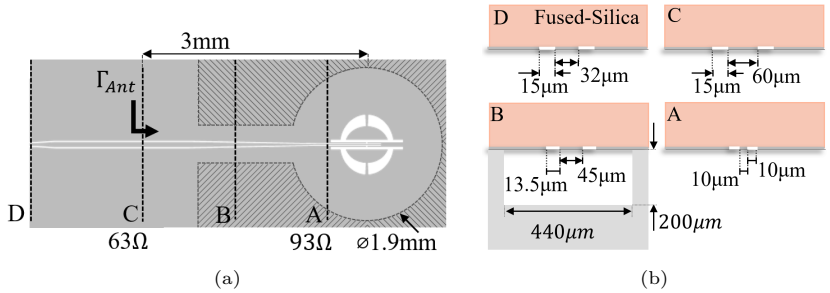

Figure 2.11: (a) Top-view of the CPW-fed double-slot geometry. The back-reflector is indicated by the gray shaded region. Several reference planes are indicated by numbers A-D. (b) Cross-sectional view at the reference planes of (a), including the CPW and back-reflector dimensions.

2.3. On-Package Double-Slot Feed Design

The double-slot feeding architecture plays an important role in the integrated antenna front-end, since it affects performance and interconnection to the MMICs. In this contribution, two options were considered: a single metal layer solution that can be fabricated with lithographic techniques using 10 µm line resolution; and a two metal layer solution which can be fabricated with a thin-film commercial process or a high-quality PCB-like process featuring 45 µm line resolution and 50 µm layer thicknesses. The one-layer high-resolution lithographic process will be realized in-house with an aluminum layer, whereas the thin-film commercial technology will use gold metallization. Because surface roughness, metal thickness and losses of these technologies are not known at these frequencies, dedicated calibration kits were developed and measured using the technique explained later in Chapter 4. It was found that the losses matched well with the simulations done with a classical surface conductivity model, as the one used in [50], with the material properties summarized in Table 2.1. These values will be used as an input to the on-package planar antenna design in this section.

The double slot shown in Fig. 2.3 is defined with α, ρ and width w_s. Below the double slot, there is a cylindrical back-reflector air-cavity defined by h_{back} and ρ_{back}, also shown in Fig. 2.3. Due to the high f/b produced by the high-dielectric core lens, its impact on the antenna impedance is small. Fig. 2.10 shows the input impedance Z_{slot} of this double-slot, indicating that it operates near the first resonance with high $\Re\{Z_{slot}\}$. Its reflection coefficient is shown in Fig. 2.8b for a reference impedance of 300Ω. However, taking into account the thin-film technology limitations, the achievable characteristic impedance Z_0 of a CPW or MS ranges from ≈50-100Ω. Therefore, the double slot has to be optimized according to the limitations of the thin-film technology.

2.3.1. Double-Slot Feed on Single Metal Layer Package

In this section, we describe the design of a double-slot antenna using a thin-film fused-silica technology with a single metal layer done via high-resolution lithography (i.e. 10 µm minimum trace and gap width). Because of the high resolution, the feeding of the double-slot can be made via a CPW transmission line on the same metal layer as in [51], which extended a classic double-slot bolometer silicon design [52] to a distributed central feeding CPW line. The proposed CPW-fed double-slot is shown in Fig. 2.11a, with its equivalent circuit approximate representation in Fig. 2.12. The central feeding line, see Fig. 2.11b cross-section A, is limited by the minimum trace width that reaches a maximum characteristic impedance of $Z_{0A} = 93\Omega$. To reach good impedance matching with a much lower reference impedance than in Fig. 2.8b, the operation of the double-slot has been shifted to the second resonance, where the real part of the impedance is lower. To this end, the double-slot has been lengthened by increasing the α to 87°. The low frequency matching is further improved by tapering the slots with $w_2 = 2w_1$ (Fig. 2.13a). The effect of these double-slot modifications on the pattern quality was found to be negligible.

The associated double-slot input impedance, shown in Fig 2.10, presents now a real part in the order of 80Ω. The remaining imaginary part is matched by adding a short-circuited stub in series with Z_{slot}, denoted by '1' in Fig. 2.13c and '$Z_{stub,1}$' in Fig. 2.12. Its effect, shown in Fig. 2.10 (red), is an increased imaginary part with a zero-crossing at the central frequency.

Then, two CPW distribution lines are introduced with $Z_0 = 80\Omega$ to transfer the impedance to the central line with minimum reflections. A second short-circuited stub in series ('2' in Fig. 2.13c, '$Z_{stub,2}$' in Fig. 2.12), is used to reach better matching to the 90Ω central CPW line. The simulated antenna input impedance Z_{in} is shown in Fig. 2.10. The geometrical parameters of the proposed design are given in Fig. 2.13. The achieved aperture efficiency of the core-shell lens coupled to this optimized double-slot with a CPW feeding is compared in Fig. 2.14 to that of the initial double-slot of Fig. 2.3. The resulting aperture efficiency drops significantly, as the central CPW-fed line increases the cross-polarization. Furthermore, the central cut of the double-slot limits the TM_0 mode suppression. For this reason, it was necessary to minimize the width of the 93Ω CPW line to 10 µm gap width and 10 µm trace width.

The double slot shown in Fig. 2.13a is connected to the central $Z_{0A} = 93\Omega$ line with 10 µm gap as indicated in Fig 2.11 (plane A). This CPW transmission line is tapered towards 63 Ω (plane B) and extends outside the back-reflector cavity (plane C). The CPW transition through this cavity was designed for minimum impact in the antenna performance. The integration of a potential MMIC could be done in the region between planes C-B via flip-chip technology. Finally, the CPW transmission

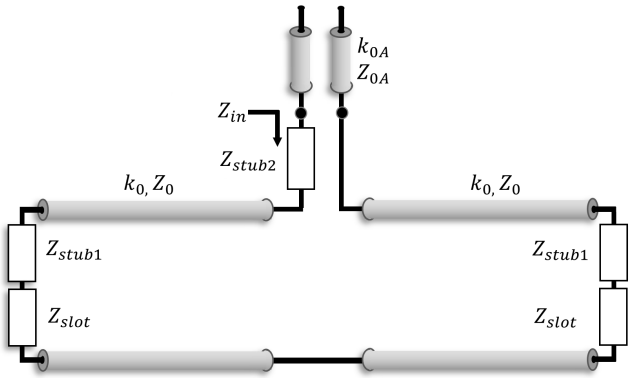

Figure 2.12: Approximate circuit model for the double slot connected by a CPW distribution line, characterized by k_0, Z_0. The two stubs 1 and 2 of Fig. 2.13 are added in series with the slot impedance and the input impedance, respectively. The final antenna input impedance Z_{in} is to be matched to the central CPW line with parameters k_{0A}, Z_{0A}.

line terminates with a transition region for probe-landing measurements at plane D. After some optimization, the final double-slot dimensions are shown in Fig. 2.13.

The resulting reflection coefficient associated to the reference plane C is shown in Fig 2.15. This feeding can achieve a matching below -10dB across 130-180 GHz band. The aperture efficiency associated to the complete design (Fig. 2.11) is shown in Fig. 2.14. There is an additional small decrease in the efficiency since the central $Z_0 = 93\Omega$ feeding line introduces some asymmetry between the two slots due to coupling with the $Z_0 = 80\Omega$ line. The ohmic and dielectric losses, given in Table 2.2, are around 1.75dB across the 140-170 GHz band. The major contributors are the ohmic losses corresponding to the CPW feeding, which are around 1.2dB, and the 0.5dB of dielectric losses of the core-lens made of PREPERM. The CPW losses are referenced to the measuring plane C indicated in Fig. 2.11a and can be reduced when integrating the MMIC.

2.3.2. Double-Slot Feed on Two Metal-Layers Package

This section describes the design steps to integrate an MS feeding network, as shown in Fig. 2.16c for the proposed double-slot feed. A second metal layer is used, separated by a 50 µm thin fused-silica substrate (see Fig. 2.17a).

Due to the fused-silica substrate below the double-slot ground-plane, the effective wavelength in the slots becomes shorter. Therefore, the double-slot of Fig. 2.3 with $\alpha = 67^o$ and the fused-silica substrate underneath is already in second-resonance

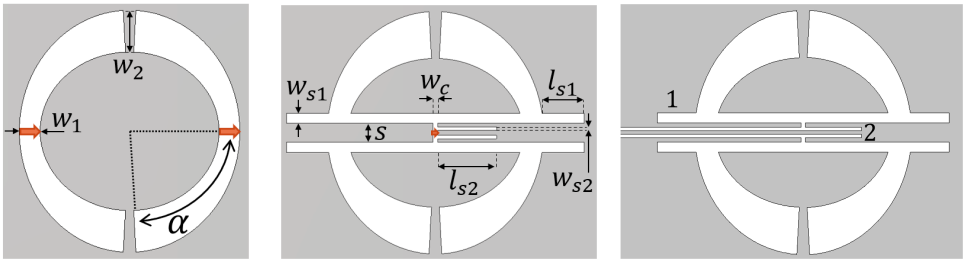

(a) (b) (c)

Figure 2.13: (a) The double slot that has been tapered with parameters $w_2 = 2w_1$ and $\alpha = 87°$. (b) The elliptical double slot with a central feeding point, incorporating a CPW line and two matching stubs (c) The same double-slot as in (b), but now being fed by a central CPW line. The final design has dimensions (in µm) w_1=60, w_2=120, w_{s1}=30, l_{s1}=115, w_{s2}=10, l_{s2}=163, s=55, w_c=14, α=87°.

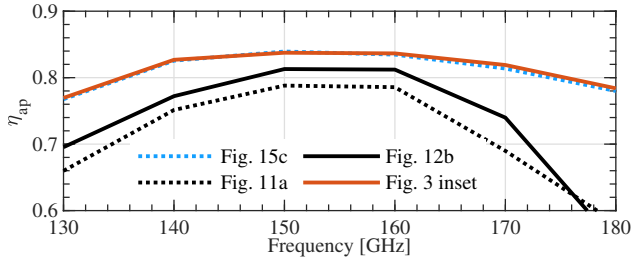

Figure 2.14: Aperture efficiencies of the shell lens, comparing the cases with (dotted) and without (solid) feeding networks for both MS and CPW lines.

condition with low $\Re\{Z_{slot}\}$, as shown in Fig. 2.18. To match this impedance, a microstrip of Z_0=74Ω and an inductive stub in the order of 70Ω is required. An MS feeding network, shown in Fig. 2.16c is designed to feed the double slot. From a 50Ω transmission line, a power combiner is used to couple to both slots terminated with the stub. Fig. 2.17 summarizes the dimensions, impedances and approximate equivalent circuit of the MS-fed feeding network.

Since vias were unavailable in the considered technology, an open-ended series stub of ≈1.1 mm will then be needed, which does not fit between the slots separated by 0.6mm. The stubs, power combiner and slots should have enough clearance to avoid coupling between the three. Therefore, the double-slot has been redesigned with a limited angle α=63°, thereby allocating enough space for both the transmission lines and stubs. Then, to reduce the inductance requirement, the double-slot is reshaped by the parameters ρ_1 and ρ_2, with $\rho_2 > \rho_1$, thereby forming an elliptical slot topology enabling more space for the power combiner, as shown

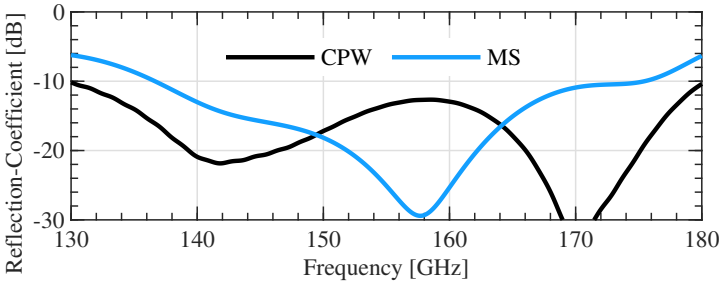

Figure 2.15: The full-wave simulated S_{11} matching of the CPW antenna (Fig. 2.11a) and the MS antenna (Fig. 2.16c) at reference plane C with $Z_0 = 63\Omega$ and $Z_0 = 50\Omega$, respectively.

Table 2.2

Simulated Ohmic and Dielectric Losses at 155 GHz

Material	CPW Loss (dB)	MS Loss (dB)
Aluminum	1.22	
Gold		0.43
Fused-Silica	0.05	0.04
PPE950	0.33	0.41
HDPE	0.13	0.16
Total	1.73	1.03

in Fig. 2.16. The resulting impedance is given in Fig. 2.18. This additional degree of freedom has negligible effects on $\Re\{Z_{slot}\}$ but reduces $\Im\{Z_{slot}\}$, thereby enabling impedance matching with a shorter open-ended stub. Finally, an inductive open-stub has been designed using a tilted and tapered radial stub as shown in Fig. 2.16b. The final stub design has radius of 200 µm and tapering angle of 15°.

Unlike the CPW feeding lines, this feeding topology can be fabricated with lines wider than 45 µm, showing its potential for other packaging technologies. Using the 50 µm fused silica technology in combination with gold, a 50Ω transmission line achieves a loss of <0.15dB/mm. The reflection coefficient of this MS feeding network, including the double slot is shown in Fig. 2.15. The S_{11} is below -10dB for a $Z_0 = 50\Omega$ over the 135-170 GHz frequency band. This reflection coefficient is reported up to the measurement plane C shown in Fig. 2.16c. This transition was designed with minimal impact on the reflection coefficient and radiation properties of this antenna.

The full-wave simulated losses of the MS-fed core-shell lens antenna are shown in Table 2.2. Total losses amount to around 1dB including dielectric and ohmic loss up

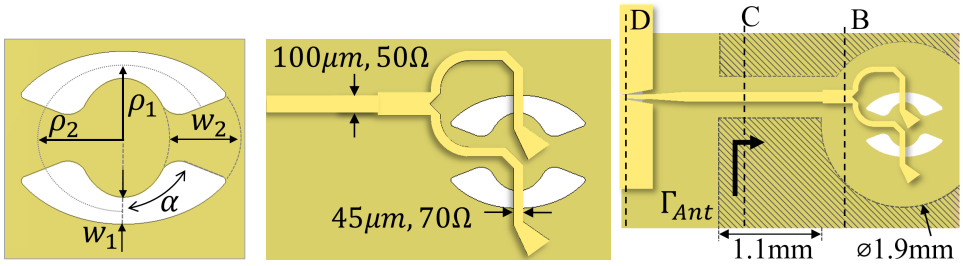

(a) (b) (c)

Figure 2.16: a) Geometry of the elliptical double-slot used for matching to a microstrip network. Final parameter values (in mm): ρ_1=0.279, ρ_2=0.34, w_1=0.1, w_2=0.3, α= 67.3°. (b) The same double-slot with the microstrip feeding network integrated in the second metal layer. (c) The full layout including the back-reflector in the shaded region, and the probe landing transition. The measurement reference plane is indicated by C.

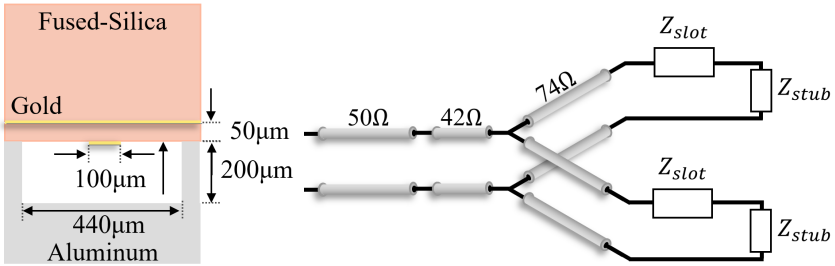

(a) (b)

Figure 2.17: (a) Cross-sectional view of the MS antenna at plane C of Fig. 2.16c. (b) The microstrip equivalent circuit model with the 3dB power divider, slot and stub impedances.

to the reference plane C, which is closer than in the CPW case. Fig. 2.14 shows the aperture efficiency of the core lens antenna with (solid) and without (dashed) the MS feeding network. The feeding network has only limited impact on the patterns due to low radiation loss of the transmission line, achieving an aperture efficiency above 80% across the 135-170 GHz band. Fig. 2.19 compares simulated far-field PO directivity and gain of the MS- and CPW-fed antennas. The PO directivity is evaluated using only the PO shell currents, whereas the gain was derived using the loss in Table 2.2, and also includes spillover and f/b loss. As shown, both antennas achieve similar directivity, but the MS-fed architecture achieves higher gain due to its lower ohmic loss.

The MS has a minimum feature size that is larger than the CPW (45 µm lines vs. 10 µm+10 µm+10 µm slot-line-slot), but the additional electrically-thin substrate

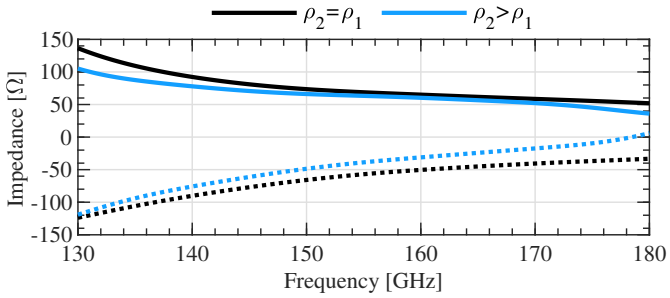

Figure 2.18: Antenna impedances for a circular double slot (black) with ρ_2=0.279mm and an elliptical one with ρ_2=0.34mm (blue).

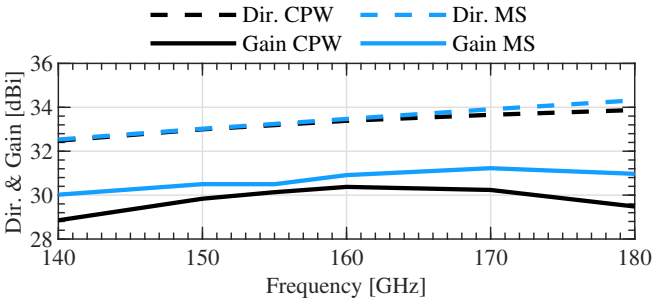

Figure 2.19: Simulated directivity (dashed) and gain (solid) for the CPW and microstrip-fed antennas.

might add considerable complexity in the overall fabrication and assembly at high frequencies. Both feeding architectures were developed and used for an antenna prototype, described in the next section.

2.4. Antenna Prototype at D-band

A prototype was developed to validate the core-shell lens antenna architecture. For this, the CPW and MS feeds, described in section 2.3, were fabricated as shown in the inset of Fig. 2.1. Each one has a long feeding line to enable measurements with RF landing probes in the 140-200 GHz range as described in the previous section.

As shown in Fig. 2.20c, the antenna prototype is composed of five main parts: the core lens, shell lens, the fused-silica wafer with the antenna feed, the back-reflector metal feature, and a metal fixture that holds the structure together.

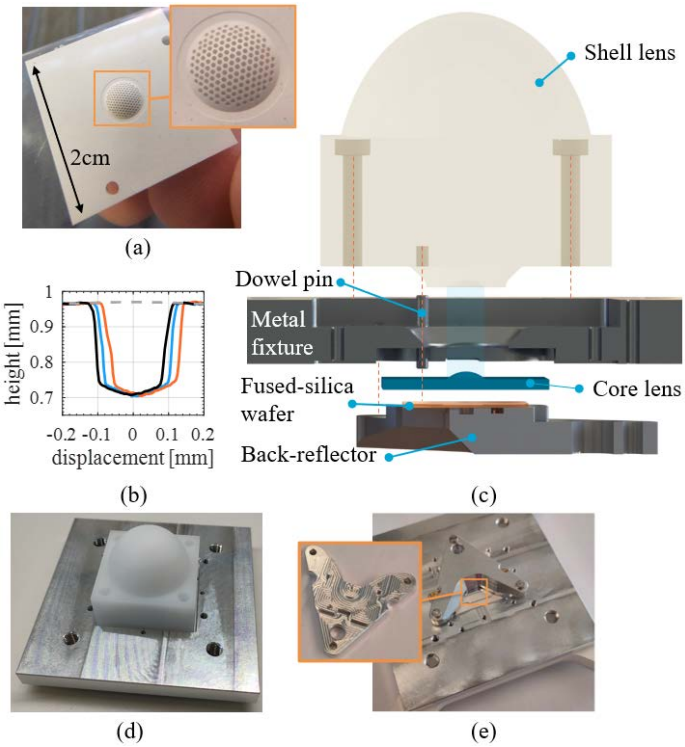

Figure 2.20: (a) Core lens prototype fabricated in PPE950 thermoplastic material. (b) Measured dimensions of the central hole along the 0° (blue), 60° (red) and 120° (black) axis. (c) Cross-sectional, exploded view of the antenna prototype assembly. Threads/dowel pin axes have been indicated in orange. (d) and (e) are photographs of the assembled core-shell lens prototype with a top and bottom view, respectively. The inset of (e) shows the upside-down view of the back-reflector.

The plastic core- and shell-lenses as well as the two metal fixtures have been fabricated using an in-house 5-axis CNC milling machine. The fabrication of the core-lens with its anti-reflection layer in PREPERM PPE950 material was realized in two steps. First, the spherical surface of the core-lens was shaped by the CNC milling machine. Next, the holes of the anti-reflection layer were drilled conformally over the spherical surface using a standard drill bit of 250 µm diameter (Fig. 2.20a). Its physical dimensions were measured using a confocal microscope, giving a diameter and depth of the holes within 20 µm from their nominal dimensions (see Fig. 2.20b).

The double-slot fed by a CPW transmission line was fabricated using photo-lithographic techniques on a fused-silica wafer of 500 µm thickness with a 1 µm

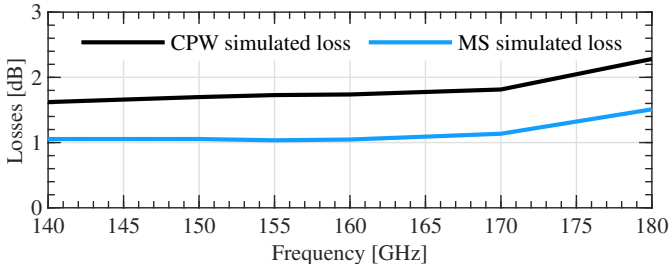

Figure 2.21: Full-wave simulated total loss in the core-shell lens antennas of the MS-fed (blue) and CPW-fed (black) architectures. The simulated losses are reported up to the reference plane C shown in Fig. 2.16c and Fig. 2.11a for MS and CPW-fed antennas, respectively.

thick aluminum metallization. The double-slot fed by the MS was realized on two wafers. The first wafer was a 50 µm on fused silica with double-side 1 µm thick gold metallization. One side containing the double-slot, the other side the MS transmission line. After, that, this wafer was bonded to a 500 µm fused silica carrier.

The assembly of all the parts was designed to reach an alignment within 100 µm. The aluminum frame that holds the different components in place is shown in Fig. 2.20d and e. This structure has a set of press-fitted dowel pins that protrude from two sides, thereby aligning simultaneously the core-lens, shell-lens and the back-reflector, as shown in cross-sectional view in Fig. 2.20c. Connecting all components to a single set of dowel pins prevents the accumulation of tolerances across different parts. As shown in Fig. 2.20, the fused-silica wafer containing the antenna was optically aligned and glued to the metal back-reflector using a similar method as in [53]. An alignment of 5 µm was achieved between the wafer and the back-reflector.

2.5. Discussion

The proposed core-shell lens antenna is summarized in the last two rows of Table 9.1 for a comparison of with the state-of-the-art. Good bandwidth and gain have been obtained, when compared to the other works. Contrary to [27], the outer lens can be scaled up to reach even higher antenna gains ($>$ 40 dB) due to the low-loss lens material. Furthermore, the proposed core-shell lens design can be extended to other increasingly popular packaging technologies. For instance, low-loss glass-ceramic interposers that can be fabricated in large volumes [30, 54]. The design can potentially also be scaled to work in even higher frequency bands, as both lithography and CNC milling technologies can be pushed further to allow for smaller

designs. Finally, the additional degrees of freedom in lens shaping can be further investigated to optimize shell lens illumination. For instance, a beam tilt could be generated by displacing laterally the feeding antenna and shaping the lens surface as in [55], instead of other more complex architectures such as [20, 21].

2.6. Conclusion

This work presented the development of a core-shell lens antenna architecture suitable for on-package integration at D-band frequencies. The key elements in the proposed architecture have been the introduction of an electrically-small core lens made with thermoplastics and an on-package antenna feed with low loss. Significant part of the work was dedicated to the validation of the proposed lens architecture in the 140-170 GHz bandwidth.

In upcoming chapters, this lens architecture will be used as a key element in Fly's-Eye antenna systems aiming at different applications in communication and sensing. From one side, the degrees of freedom introduced by the core-lens can be used to give the means to independently control the scanning performances, the side-lobe level, etc., from the directivity control given by shell lens. On the other side, the developed on-package antenna topology can be integrated with MMICs via flip chip to enable the generation of multiple spatial beams via a Fly's-Eye integrated and scalable architecture.

Chapter 3

Flat Lens Concept Using Multi-Axis Machining for D-band Core-Shell Lens-In-Package Integration

This chapter presents an electrically-small core lens that has been redesigned towards a flat interface. The core lens is physically flat, but electrically spherical. This way, the lens is easier to integrate, compared to an earlier introduced spherical core-shell lens concept. The lens is created from a single dielectric host material by conformally machining holes into the material. In this process, two artificial dielectric layers are created; The first layer is used for anti-reflection purposes, whereas the second is used to convert the spherical interface to a flat interface. The two layers enable the use of holes with lower aspect ratio drilling, compared to classical gradient-index lenses. The lens is designed to operate in the 140-170 GHz bandwidth, and a prototype with height of only 2.2 mm and diameter of 6.6 mm was fabricated and characterize. The prototype is small enough to fit in many integrated circuit packages. The flat lens was compared to a non-flat core lens in terms of pattern quality, return loss and dielectric loss, with only negligible performance degradation.

3.1. Introduction

THE previous chapter saw the design and development of the core-shell lenses with their spherical interface. Unfortunately, the dual-lens fabrication and assembly was a difficult process. The precise alignment required between the concave shell lens and convex core lens surfaces required tight tolerances. The potential for misalignment orientation and position is emphasized in Fig. 3.2b. These

misalignments could result in an additional air gap between the two lenses, leading to pattern degradation and/or increased S_{11}. These effects add to the already intricate tolerating requirements of the assembly, leading to high-cost machining. For these reasons, a design of a flat core lens would be highly beneficial. A flat lens architecture furthermore permits the lateral movement of such lens underneath a shell lens, thereby enabling lens scanning, as in [56].

A common design for flat lenses is the use of Gradient Index (GRIN) refractive index lenses. A popular technique to fabricate flat lenses is by GRIN lenses is the use of additive manufacturing [57, 58]. Recent works have demonstrated 3D printed GRIN lenses even up to sub-THz domain [59–61]. However, the choice of materials for additive manufacturing is often limited, as the materials need to be both suitable for printing and the RF application. By contrast, CNC machining offers great flexibility in the material choice. In this technique, air cavities are CNC milled inside a host material, thereby creating a GRIN structure [62]. However, drilling unit cells for beyond 100GHz is challenging, due to the high aspect ratio drilling and the large number of holes (>1000) required. Finally, in [63], a technique involving a stratification of stacked PCBs was used to shape GRIN lenses. Unfortunately, at D-band frequencies, the unit cells become too small for the PCB tolerances to be a reliable solution. Also, a large number of stacked PCBs is required to create electrically large lenses. For a detailed discussion on related antenna designs, please refer to [64]. It is due to these challenges that a novel architecture for flat lenses is required that addresses current shortcomings.

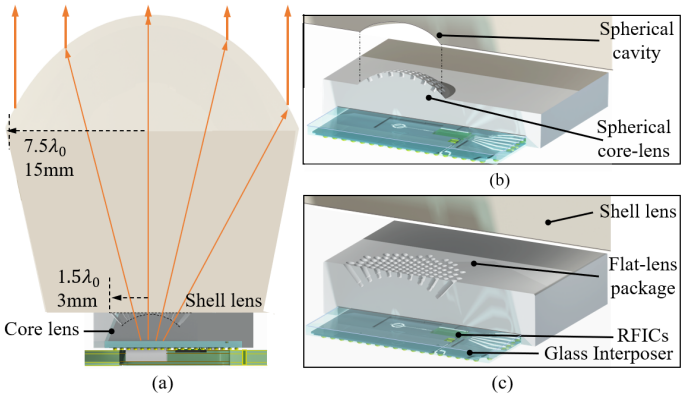

Figure 3.1: (a) Conceptual integrated core-shell lens antenna cross-sectional view. (b) Zoomed-in view of the spherical core lens interface with the spherical shell lens cavity. (c) proposed flat core lens for easier integration with the shell lens.

In this chapter, we propose a compact flat lens made of dense thermoplastics using a novel design concept. The proposed spherically conformal design is illustrated

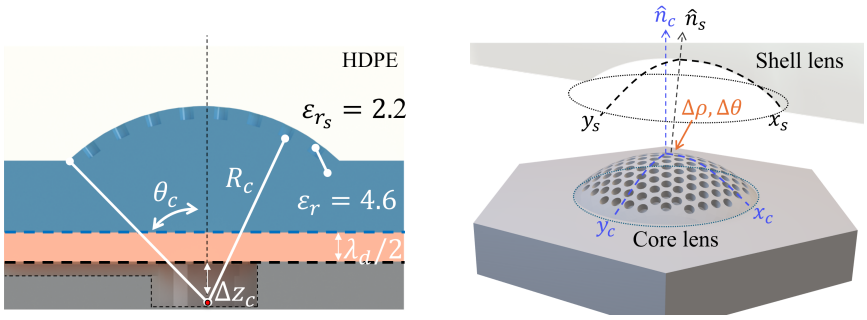

Figure 3.2: Cross-sectional view of (a) the spherical core lens, taken from [64], and (b) a 3D view of the same spherical lens. (b) furthermore indicates the potential for misalignment in orientation between the two lens interfaces. For orientation, there is the misalignment in lens normals $\hat{n}$, written as $\Delta\theta$, and in position between x, y center coordinates of the two lenses, written as $\Delta\rho$.

schematically in Fig. 3.4a. Such design conserves the spherical wavefront (i.e. not enhancing the directivity). The host dielectric material is modified via conformal machining of holes (Fig. 3.4b), resulting in two artificial dielectric layers within the compact lens structure. This topology enables a compact design that minimizes dielectric losses. The resulting flat core lens has a thickness of only 2.2 mm (1.13 λ_0, where λ_0 is the wavelength in free-space).

In parallel, a variation for the spherical design is proposed, by introducing a vertical extension of the lens feed with respect to its phase center. This extension enables an increase in the primary pattern directivity, and thereby unlocks low sidelobe level (SLL) performance.

This work addresses the design, optimization, fabrication, and characterization of this novel flat lens topology. The simulation methodology used to create and refine the lens design is detailed, followed by the fabrication process using multi-axis machining. Finally, the performance of the fabricated antenna prototype is validated through a set of antenna measurements.

3.2. Flat Lens Design

Commonly, GRIN lenses are used to create a flat lens interface using well-known theoretical frameworks [66]. In [65], a GRIN lens was designed to synthesize the core lens of [64], which was implemented on a PCB stack-up with thickness T. For such a design, the maximum required permittivity, which is proportional to a factor $1/T$, was $\varepsilon_{r,max} = 25$, as shown in Fig. 3.3a. Increasing T of the GRIN would lower

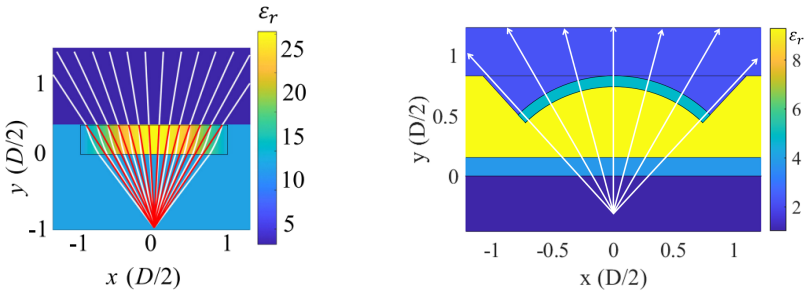

Figure 3.3: Comparison of the material effective permittivity distribution between (a) the GRIN lens of [65] and (b) the proposed flat core-shell lens.

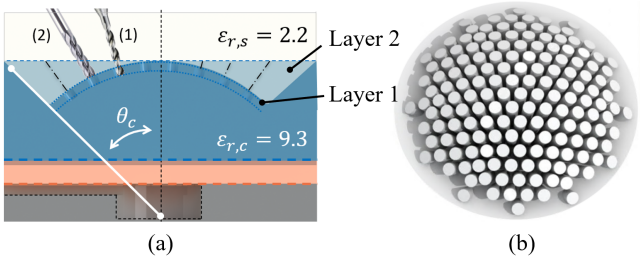

Figure 3.4: (a) The same core lens as in [64], but now adapted to a flat interface using an effective $\varepsilon_{r,s}$ permittivity. The two artificial dielectric layers are indicated. The two machining steps have been indicated. (b) Indication of the conformal drills required to shape the internally conformal flat lens.

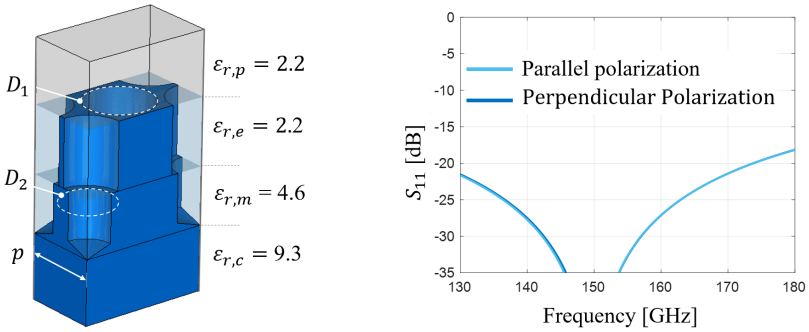

(a) (b)

Figure 3.5: (a) Unit-cell of the matching layer. The optimized geometry has a matching layer diameter D_2 of 250 µm, effective permittivity layer diameter D_1 of 320 µm, and periodicity p of 360 µm ($\approx \lambda_d/4$). (b) The resulting S_{11} performance of the optimized unit cell.

this maximum permittivity, but also implies higher aspect ratio drilling and/or more PCB layers. Such type of GRIN lens implemented in dense thermoplastics with the same dimensions as [64], would need a permittivity of around 18, which increases not only the ohmic loss but also the fabrication challenges due to the reduction in the unit cell sizes.

In this work, 5-axis conformal machining is used to enable a flat core lens with a thickness of only 2.2 mm (1.13 λ_0) using a lower permittivity $\varepsilon_{r,c} = 9.3$ dielectric material. The main scope of the spherical core lens of [64] was to conserve the spherical wavefront that transitions between the core and shell lenses. The design is shown in Fig. 3.3b, and uses only three permittivity values: A host material with $\varepsilon_{r,c} = 9.3$ for the spherical core lens, $\varepsilon_{r,m} = 4.6$ for the matching layer and $\varepsilon_{r,e} = 2.2$ for the effective permittivity of the shell lens. Both $\varepsilon_{r,m}$ and $\varepsilon_{r,e}$ are obtained by removing part of the host dielectric material via the conformal holes. The detailed lens topology will be explained in the next sections.

3.2.1. Flat Lens Topology

The proposed novel flat lens concept is shown in Fig. 3.4a. The lens is made of PREPERM ($\epsilon_{r,c}$=9.3, tanδ = 0.005), and internally has the same electrically small ($\approx 3\lambda_0$) spherical core lens including matching layer as in [64], shown in Fig. 3.2. However, a key difference is that now, instead of milling a spherical surface, the PREPERM material left with a flat interface by CNC machining an effective permittivity equal to the HDPE medium ($\epsilon_{r,s}$ = 2.2, $tan\delta$= 0.0003). This enables the core lens to have an 'electrically' spherical interface, that is physically flat. This

flat interface does not suffer from the same misalignment penalties as the spherical lens of Fig. 3.2b. A shift in position will only impact lens scanning, but has negligible impact on S_{11}. Finally, the orientation misalignment $\Delta\theta$ can be further mitigated due to the flat interfaces.

Fabrication of the artificial dielectric media is performed in a two-step approach, shown in Fig. 3.4b. First, like in [64] (Fig. 3.6a) the matching layer with effective $\epsilon_{r,m} = 4.6$ is drilled conformally with a 5-axis CNC machine, using a standard 250 µm drill bit. Next, the layer with effective $\epsilon_{r,e} = 2.2$ will be milled using the same periodicity as the previous layer, but with a slightly larger hole size. A conical taper originating from the antenna phase center was applied to the hole diameters, to keep the same volumetric fill ratio as the wave expands spherically. Although the conical hole milling provides a more constant $\epsilon_{r,eff}$, its machining is also more time-consuming than drilling of cylindrical holes. However, due to the electrically small size of the core lens, both conical and cylindrical holes could work, as the spherical spreading has only limited impact. In our proposed prototype, conically spreading holes were chosen for completeness.

With the fabrication process in mind, the next step was to derive the dimensions for the conformally drilled holes.

3.2.2. Unit-Cell Simulations

To simulate the performance of the medium with effective permittivities, a Floquet-mode unit cell was used, shown in Fig. 3.5a. First, the matching layer situated between the ϵ_r=9.3 and $\epsilon_{r,e} = 2.2$ materials was designed nearly identical to [64], with a fixed hole diameter of 250 µm, period of $\approx$ 360 µm (variable) and depth of 255 µm ($\lambda_d/4$). This produces an $\epsilon_{r,m}$ of 4.6. Then, the milled layer with aimed effective permittivity of 2.2 was added in between the HDPE and matching layer. The structure was optimized by minimizing the S_{11} when iterating over the hole diameter and periodicity. The optimized S_{11} is shown in Fig. 3.5b, presenting $<$ 20 dB reflection coefficient for both parallel and perpendicular directions. The good dual-polarized performance implies not only that circularly-polarized feeding antennas can be used, but also that during the integration of the lenses, any rotational misalignment will not degrade antenna performance. The optimized performance was obtained using the dimensions stated in the caption of Fig. 3.5.

3.2.3. Spherical Flat Lens Design

Once the unit cell was optimized, the effective permittivity layer was designed conformally to the spherical core lens surface. The subtended angle $\theta_c = 45°$ was

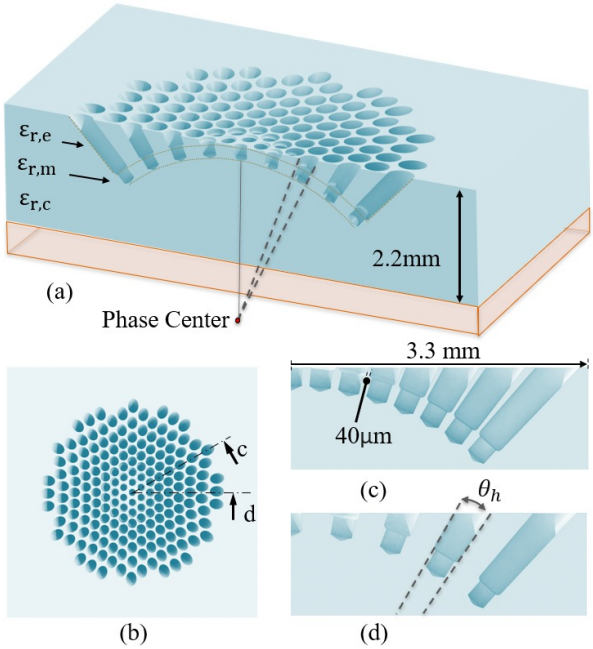

Figure 3.6: (a) Proposed flat core-lens prototype in cross-sectional view, indicating the different permittivity layers. (b) Top view of the flat core lens, with the cross-sectional views assigned in (c) and (d).

kept similar to [64]. A cross-sectional view of the designed flat core lens is shown in Fig. 3.6b. The different layers are indicated inside the 2.2 mm thick lens, and the internal spherical core is visible. A top-view is presented in Fig. 3.6b, where all holes are visible in the hexagonal layout. The presented core-shell lens solution only requires 170 holes to synthesize both the matching layer and the effective permittivity layer. This in contrast to GRIN lenses found in literature with > 1000 drills ([62]), that operate < 100 GHz. Fig. 3.6b also indicates two cross-sectional lines, shown in Fig. 3.6c and 3.6d for 30° and 0° hexagonally symmetric cutting planes, respectively. The 30° cross-section represents the worst-case scenario with a minimum wall thickness between two adjacent holes of only 40 µm. However, due to the hexagonal layout, the wall thickness gradually increases until its maximum at 0° cross-sections. Also shown in Fig. 3.6a and d is the conical tapering that is applied to the holes. This means that the hole size is spherically increasing in size, with a fixed angle θ_h, with the sphere radius coincident with the phase center. Such hole is fabricated by milling an increasingly larger hole size from the phase center,

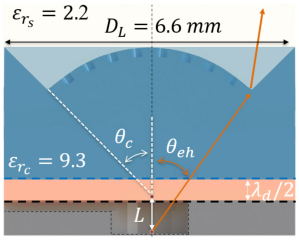

Figure 3.7: Geometry of the extended hemispherical lens. The extension is described by parameter L, as seen from the phase center. Except for this extension, the lens is identical to Fig. 3.4

thereby creating a conically-shaped hole. This method is applied to keep the same volumetric fill ratio as the wave expands spherically.

3.2.4. Extended Hemispherical Flat Lens

An additional degree-of-freedom can be introduced in the flat lens design by including a vertical extension in the flat lens profile. Such design is a popular technique to enhance lens directivity [67]. This extended hemispherical geometry is shown in Fig. 3.7, where the vertical extension is dictated by parameter L. The hemispherical part of the lens is kept the same as in the non-extended lens. By choosing different values of L, different lens focusing capabilities can be selected.

In this work, an extension of $L = 1.45$ mm ($0.75\ \lambda_0$) was chosen, as a compromise between the SLL reduction and the lens spillover. The core lens subtended angle θ_c is kept the same 44° as the spherical flat lens. Therefore, the subtended angle θ_{eh} is reduced to 31.8 °. This way, Increasing the lens extension whilst keeping the same lens geometry increases lens spillover loss. However, this effect could be decreased by increasing the lens truncation angle θ_{eh} further (See Fig. 3.7).

3.3. Simulation Results

3.3.1. Conformal Flat Lens

The design was simulated in a full-wave CST microwave studio solver. Similar to [64], the lenses were fed by a double-slot that is lithographically printed on a glass substrate, acting in turn as a leaky-wave feeding antenna.

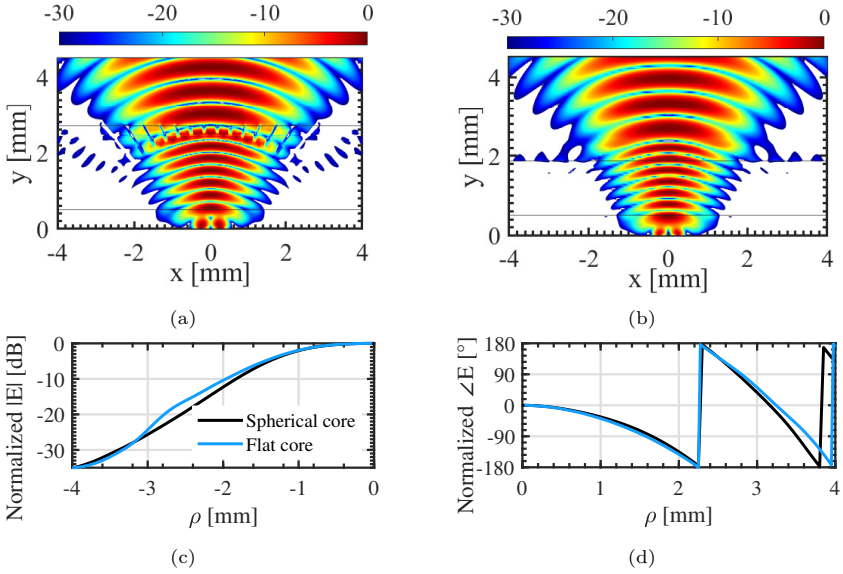

Figure 3.8: (a) Full-wave simulation of the normalized E-field (in dB) propagating at 155 GHz through the core lens. (b) The comparison to the same E-field propagating through the spherical core lens of [64]. (c) The comparison of the normalized near-field E-field amplitude at y = 3 mm between the spherical and the core lens. (d) The same comparison, but now in phase.

Fig. 3.8 compares the 155 GHz E-fields propagating through the flat core lens (a) and spherical core lens (b) interfaces. Horizontal lines have been added to indicate the core lenses. Both interfaces conserve the spherical wavefront as the material changes from dense thermoplastic to low-density HDPE. The flat lens has some stray radiation towards ± 60° angles, most likely caused by the reflections at the outer edges of the effective permittivity layer. However, its amplitude is at ≈ -30 dB w.r.t. the maximum E-field found at the center. Finally, Fig. 3.8c,d compares the amplitude and phase at the near-field at y = 3 mm. Both lenses show near-identical behavior in both metrics.

The primary patterns in infinite HDPE medium of both spherical and flat core lenses are compared in Fig. 3.9. Only limited pattern degradation occurs when switching to the new topology. As can be observed in Fig. 3.8a, at angles close to the edge of the effective permittivity layer, the performance degrades because the material no longer provides the $\varepsilon_{r,e} = 2.2$ effective medium condition. This most likely causes an increase in radiation at large angles away from bore sight (> 50°), as visible in Fig. 3.9. A larger θ_{core} could help mitigate the problem, at the cost of increased machining time. As in [64], the pattern quality is quantified in

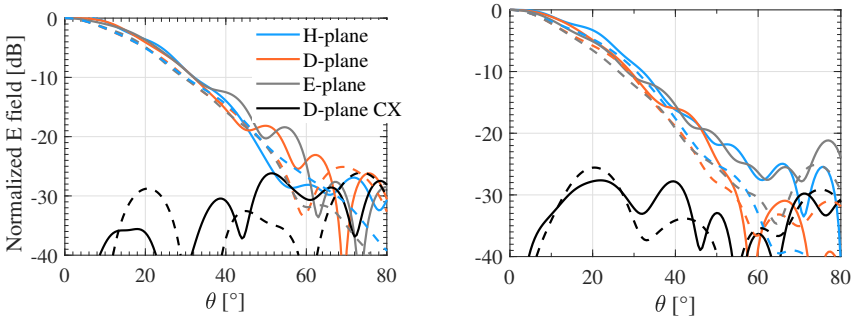

Figure 3.9: The primary patterns inside the infinite HDPE medium at 150 GHz (a) and 170 GHz (b) in solid, respectively. They are compared with the patterns of the spherical lens (in dashed). The D-plane CX represents the cross-polarization in the 45° plane, normalized to the co-polarized component at broadside. Both figures share the same y-axis.

the aperture efficiency η_{ap}, where the patterns in infinite $\varepsilon_{r,p}$ medium are analyzed using the Fourier optics tool of [48]. The resulting η_{ap}, representing the shell lens illumination efficiency, is shown in Fig. 3.10a. The shell lens subtended angle is set to 37° to optimize η_{ap}. A small difference of only 1-2 % is observed when comparing the flat and spherical core lenses.

The antenna S_{11}, shown in Fig. 3.10, has similar behavior for both lenses, indicating that the flat lens is also able to present a near-reflection-less interface to the feeding antenna. Furthermore, we note that the simulated dielectric loss increases from 0.23 dB to 0.36 dB, when switching from the spherical to the flat core lens, due to increasing the wavefront path through lossy dielectric material.

To conclude, Fig. 3.11 shows the secondary patterns in free space of the flat core and shell lenses, obtained using the GO/FO tool of [48]. The resulting patterns have good azimuthal symmetry, indicating that the flat core lens provides good rotational symmetry for the wavefronts. Furthermore, no large differences between the flat lens and spherical lens are observed.

3.3.2. Extended Hemispherical Flat Lens

Simulating the extended hemispherical lens was done in the same way as the non-extended variant, using a full-wave solver. The effect of the extension becomes apparent when analyzing the lens primary patterns (e.g. in infinite ε_r=9.3) for their directivity. This is shown in Fig. 3.12a. The extension enables an additional 3 to 4 dB of directivity. This implies that the shell lens is illuminated with a more tapered

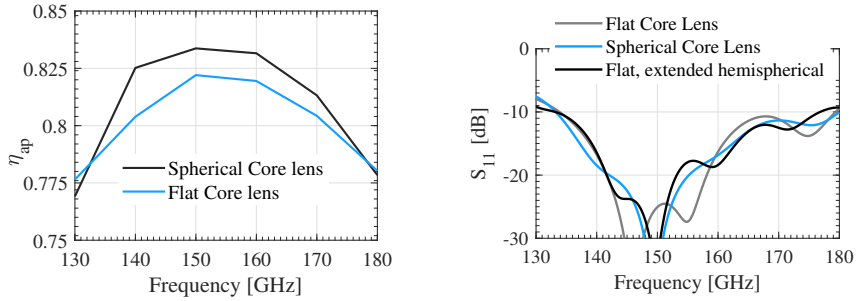

Figure 3.10: (a) The flat lens aperture efficiency compared to the spherical lens. (b) S_{11} comparison of flat and spherical core lenses.

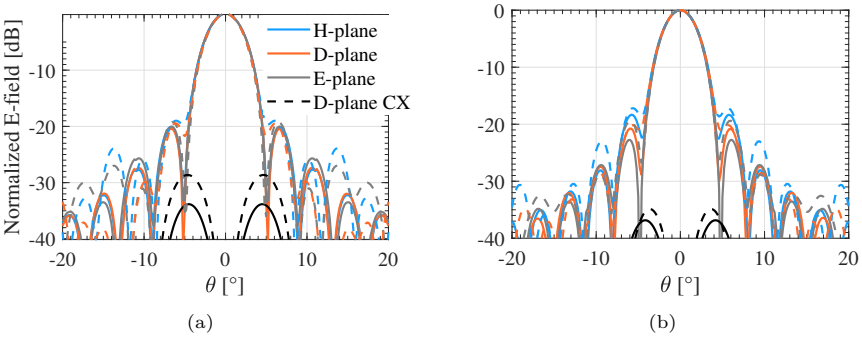

Figure 3.11: Free-space secondary patterns derived using the GO/FO tool of [48] for (a) 150 GHz and (b) 170 GHz, comparing the flat lens (solid) versus the spherical lens (dashed). Both figures share the same y-axis.

amplitude distribution, compared to the non-extended lens. The result is apparent in the far-field patterns, shown in Fig. 3.12b. The SLL is significantly decreased by >8 dB, when compared to the conformal lens patterns of Fig. 3.11. The penalty is paid in main-beam directivity, calculated using [48], and compared in Fig. 3.12c. The difference in directivity between the $L = 0$ mm and $L = 1.45$ mm antennas is 0.97 dB at the central frequency. Finally, Fig. 3.10b shows that simulated S_{11} behavior is similar for the extended hemispherical lens and the non-extended lens.

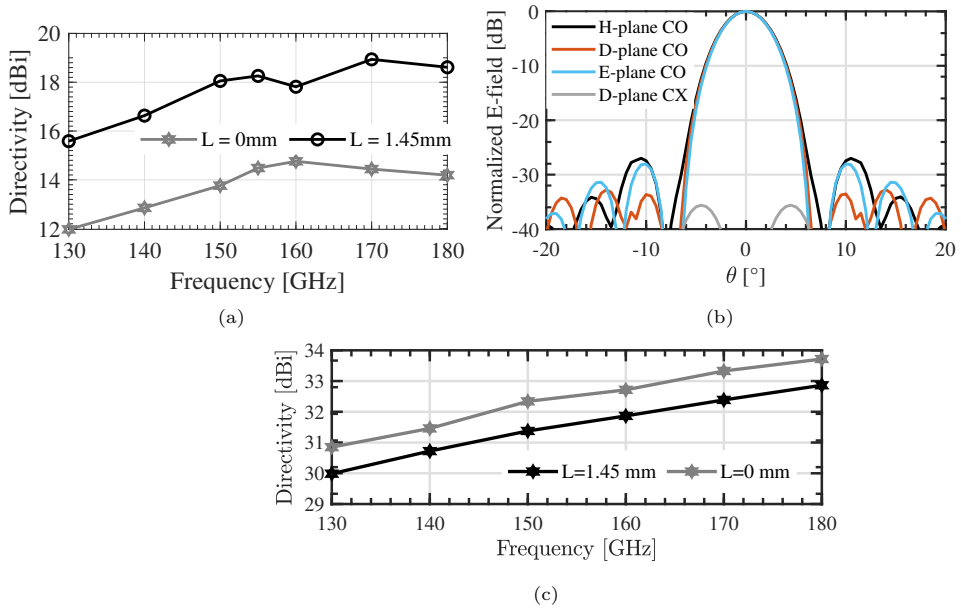

Figure 3.12: (a) Full-wave simulated primary pattern directivity of the flat lens without extension (L=0), and the flat lens with 1.45 mm extension. (b) The resulting free-space secondary pattern at 155 GHz, with the reduced SLL, compared to non-extended lens. (c) The comparison in simulated free-space far-field directivity of the two lenses.

3.4. Flat Lens Prototype at D-band

We fabricated the conformal flat lens to experimentally test the concept and design, and to make the direct comparison to the spherical lens of [64]. The conformal flat lens prototype was fabricated using aforementioned 5-axis machining techniques. The prototype is shown in Fig. 3.13. The 20 × 20 mm outline and the location of the dowel pins is exactly the same as in [64]. The prototype is added to the same dual-lens assembly of [64], as shown in Fig. 3.14. The feeding antenna, shown in the inset of Fig. 3.14, is a lithographically printed double-slot antenna with coplanar waveguide (CPW) transmission lines, as taken from [64]. A detailed view of the lens is shown in the inset. Although small deformations in periodicity and uniformity are visible at the center of the lens, the overall fabrication process is according to specifications.

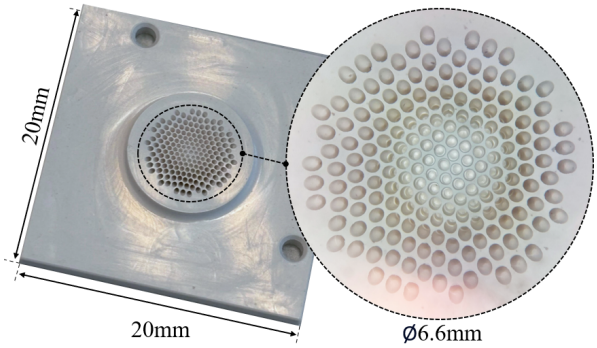

Figure 3.13: Fabricated prototype of the flat lens. The inset shows in more detail the drilled holes in the hexagonal grid layout.

3.5. Conclusion

This chapter presented a design strategy for a novel compact flat lens using conformal CNC machining. The flat lens interface can be easily integrated to form a dual-lens architecture for a Fly's-Eye communication system. Two designs were illustrated, a conformal design similar to earlier work, and an extended hemispherical design. This adjustment allows the lens to trade off the directivity with reduced sidelobe levels, a property that becomes particularly useful in later chapters on system integration.

The conformal flat lens was fabricated using 5-axis CNC machining techniques. The resulting compact flat core lens prototype has a height of only 2.2 mm (1.13 λ_0) and a diameter of 6.6 mm (3.4 λ_0). The compactness enables such lens to fit inside an RFIC encapsulation, hence providing the name lens-in-package.

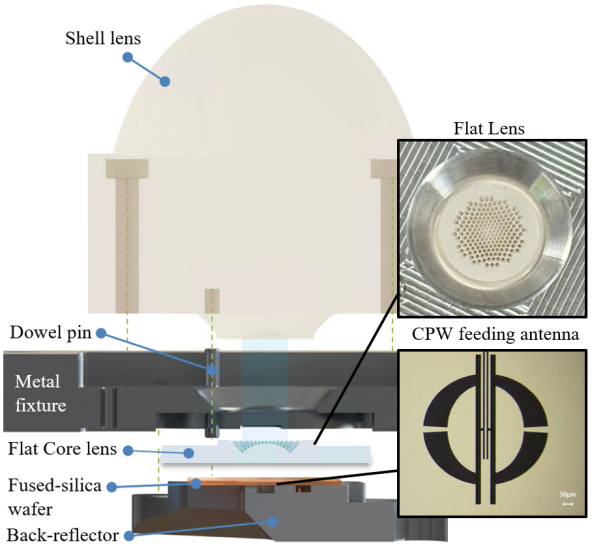

Figure 3.14: Exploded view of the prototype assembly, the same as in [64], except that its spherical core lens is now replaced by the flat lens. The insets show the photographs of the flat lens inside the assembly and the CPW feeding antenna from [64].

II

QO Measurement Techniques

Chapter 4

A Near-Field Quasi-Optical Measurement Technique for Probe-Fed High-Gain Backside-Radiating Antennas

This chapter presents the measurement strategy to accurately characterize probe-fed high-gain antennas operating in the sub-THz band. First, a near-field technique employing a quasi-optical system is introduced in Section 4.2 to enable characterization of backside radiating antennas (with respect to the landing pads). The proposed setup employs classical manipulators for probe landing (i.e., above the structure) and linear xyz CNC controlled translation stages. Then, calibration and modelling techniques were introduced to allow for an accurate input reflection-coefficient at the antenna input plane, and to provide an estimation of the antenna gain, as described in detail in Section 4.3. The experimental data of two high-gain backside-radiating lens antennas operating in D-band are presented in Sections 4.4 and 4.5 to validate the proposed approach and characterization bench.

4.1. Introduction

THE sub-THz band above 100 GHz is being targeted for the upcoming 6th generation of communication systems, partially thanks to its large available bandwidth. High-capacity line-of-sight data links are being proposed for coverage in highly dense scenarios, such as the one presented in [35] or for back-haul systems

[68]. For these scenarios, high-gain lens antennas are envisioned to realize the required transmit (Tx) and receiver (Rx) gain to establish a communication link [27].

We propose the use of planar scanning systems in combination with quasi-optical (QO) approaches to characterize probe-fed and backside radiating antennas in the near-field. To do this, a novel approach using a 45° mirror is introduced, providing a 90° rotation between the AUT radiation and the measurement plane, allowing to decouple the landing environment from the motorized one (see Fig. 4.1). The use of linearly motorized translation stages enable high precision control, even with higher mechanical loads compared to the robotic arms. As a result, accurate phase acquisition in the sub-terahertz can be achieved by employing mm-wave extender-based architectures.

Moreover, we detail the techniques to accurately characterize, in the sub-THz range, the antenna input impedance and the antenna gain in setups operating in the near field. To have an accurate reflection coefficient measurement, a calibration and modeling technique has been implemented to transfer the calibration accuracy of a two-port Thru-Reflect-Line (TRL) to a one-port Short-Open-Load (SOL), this is described in Section 4.3. A technique to estimate the antenna directly from one set of measurements and simulations of the AUT in the near field is introduced in Section 4.4. The proposed setup and the discussed techniques are validated on a probe-fed backside radiating lens antenna from chapter 2.

4.2. Near-Field Planar Antenna Measurement Setup

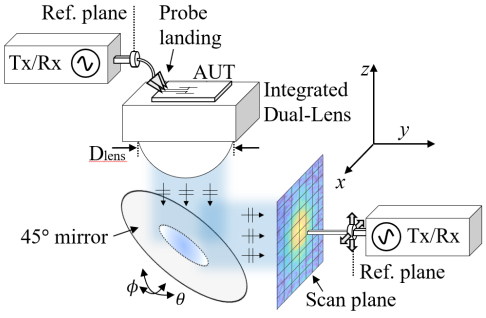

Figure 4.1: (a) Schematic of the planar near-field antenna measurement setup.

The characterization of the antenna has been realized via a custom measurement test bench shown schematically in Fig. 4.1, that combines a planar near-field scanner based on a CNC machine with a probe station. The near-field antenna measurement

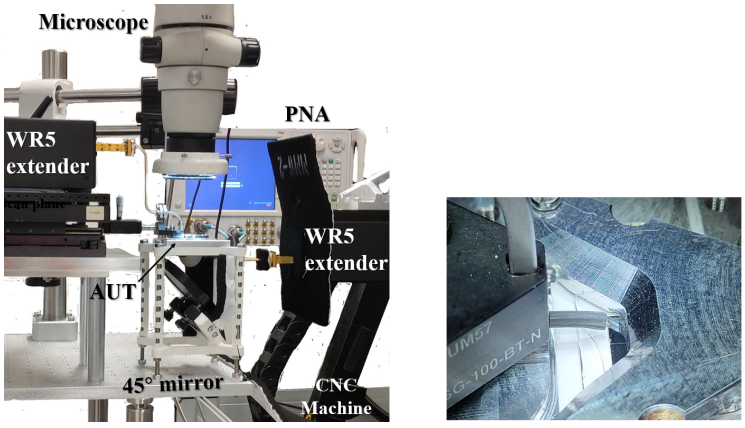

(a) (b)

Figure 4.2: (a) Photograph of the measurement setup for the core-shell lens antenna using a CNC actuated waveguide probe and extender manipulator platform for the RF probe. (b) Photograph of the RF landing probe above the CPW feeding antenna. The inset shows the CPW transmission line that connects the landing probe to the double-slot antenna below the back-reflector in the center.

setup is shown in Fig. 4.2a. It uses a CNC mechanical x-y-z scanner and a vector network analyzer (VNA) with WR 5.1 frequency extender modules to measure the antenna S-parameters. The AUT is fed by a wafer probe mounted on a commercial micro-manipulator, securely mounted on an optical table. The one-port probe station uses 100 μm pitch WR5.1 RF probes to land onto the CPW- and MS-pads with <10 μm accuracy, as shown in Fig. 4.2b. The planar near-field scanner and one-port RF probe-station were assembled in two independent tables to suppress the propagation of the vibrations traveling from the CNC machine toward the antenna RF landing probes.

To enable the quasi-optical plane translation, the AUT is fixed to a metallic fixture that positions the lens antenna facing downward. The fixture holds a 45° flat mirror used to forward the radiation towards the near-field x-z measurement plane (see Fig. 4.1). The mirror is mounted on a manual rotation stage that can adjust the tilt in θ and ϕ. These two degrees of freedom allow for the alignment of the aperture antenna with the waveguide probe. For example, with the employed lens AUT which radiates a collimated beam, the alignment is achieved by maximizing the flatness of the measured phase on the scan plane. A circular 3-inch (≈76 mm) mirror provides a projected ellipse of 76 mm × 54mm which is significantly larger than the projected circular aperture of the lens (D_l=30 mm). Since the lens antenna radiates a collimated beam, the beam will not diverge significantly in the proximity

of the lens. In this case, the distance between the lens and the mirror was 24mm, and from the mirror to the measurement plane was 64mm.

The near-field measurement plane, indicated in Fig. 4.1a, is scanned by an open-ended waveguide probe connected to the second VDI WR 5.1 frequency extender. RF absorbers were used around the waveguide area of the extender to minimize the multiple reflections in the setup. With this setup, the reflection coefficient, radiation patterns and gain were characterized and will be explained next.

4.2.1. 1-Port SOL Calibration

The input reflection coefficient of the AUT is a parameter of key importance in the characterization of the antenna. Conventionally, when an over-the-air setup is considered (i.e., port 1 connected to a wafer probe and port 2 connected to the probe antenna), a one-port calibration is carried out at port 1 and an eventual de-embedding step is employed to reach the antenna reference plane. When operating at sub-THz frequencies, the error introduced by the inaccuracies of the calibration standard definitions (both commercially available and custom designed/EM simulated) of the devices used in the calibration process, i.e., short, open, and load, makes this approach not pursuable. Calibration algorithms such as the thru-reflect-line (TRL) requiring partial knowledge of the standards' response [69] are the traditional approach to correct VNA systematic errors, and to derive fixture and interconnection responses at sub-THz [70]. Such approaches (offline TRL calibration) can be used to derive the entire input section bend with probe and antenna feed transition (i.e., S_{probe} and S_{tran} in Fig. 4.3a), by using dedicated calibration structures in a two-port probe station. Nevertheless, the connecting/reconnecting of mechanical (pre-characterized) parts in sub-THz setups, leads to poor overall accuracy, as shown in Fig. 4.8, dashed, where the resulting antenna reflection coefficient is shown. To improve the accuracy of the measured input impedance, we use transfer devices to replicate the accuracy of the TRL calibration to the one-port calibration [71].

This procedure is accomplished by first performing a probe-level TRL calibration using the device shown in Fig. 4.4a, fabricated on a fused silica substrate. After this calibration, the response of the SOL transfer standards shown in Fig. 4.5 is acquired. These transfer standards can then be employed in the setup of Fig. 4.1b to derive (without removing any connection in the setup) the de-embedding data from the waveguide calibration up to the probe tip (i.e., S_{probe} matrix). Finally, a TRL kit to extract the response of the transition from the landing pads to the antenna feed-line is measured, as a second-tier TRL (concerning the probe plane TRL), shown in Fig. 4.4b, providing the S_{tran} matrix of Fig. 4.3b.

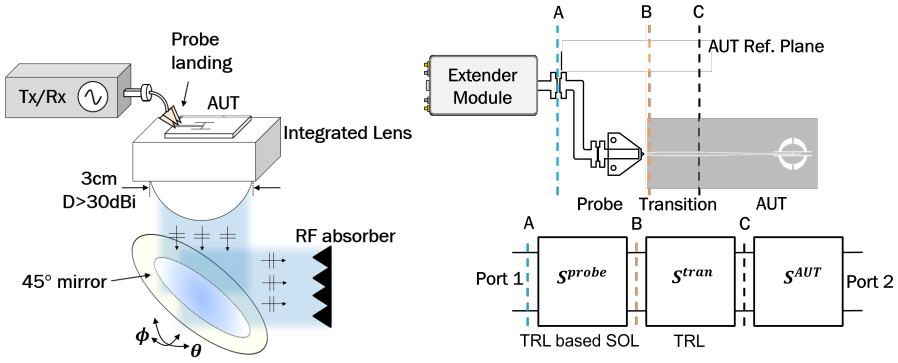

(a) (b)

Figure 4.3: (a) Schematic of the measurement setup for extracting the reflection coefficient. (b) Schematic overview of the different calibration procedures to move the measurement plane from the waveguide flange A to the antenna reference plane C.

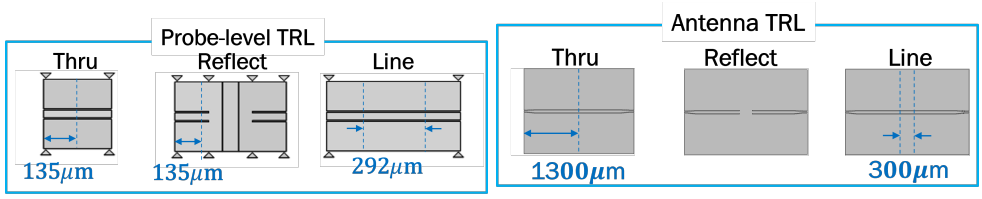

(a) (b)

Figure 4.4: (a) Probe-level TRL calibration. (b) TRL cal kit for de-embedding until antenna reference plane (blue dashed lines). Images are not to scale.

The quality of the calibration transfer standards, employed in the one port antenna setup, can be evaluated by comparing, in the two port probe station environment, the S-parameters of the line of the transition TRL kit using two methods: First, a direct TRL calibration using the custom designed calkit shown in Fig. 4.4b. This represents the reference data. Second, an indirect two-port calibration using the transfer standard S_{tran} matrix to de-embed the transition section. The results of this comparison are also shown in Fig. 4.7, validating that the calibration transfer standards will achieve the same calibration quality as the one they have been derived from. The two-port probe-level calibration then allows us to measure the 1-port SOL calibration responses. This way, when changing to the 1-port antenna measurement setup, the calibration can be retrieved using the now-known SOL calibration standard.

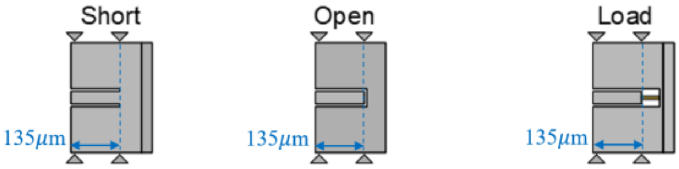

Figure 4.5: 1-port SOL calibration kit.

(a)

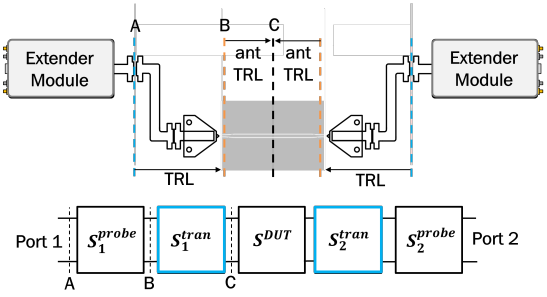

(b)

Figure 4.6: (a) Two-port probe station setup at WR-5. (b) Block diagram showing back-to-back the S-parameters boxes from port 1 (left) towards port 2 (right).

4.2.2. 2-Port SOL Calibration

For the two-port calibration using the two-tier SOL technique, the SOL error terms are converted to an S-parameter box by using $S_{11}^{SOL} = E_D$, $S_{22}^{SOL} = E_S$ and $S_{12}^{SOL} = S_{21}^{SOL} = \sqrt{E_R}$. The Antenna T-parameters are then provided by

$$T_{ant} = \left[T_t^{-1}\right] \left[T_{t,SOL}^{-1}\right] [T_m], \tag{4.1}$$

where $\left[T_t^{-1}\right]$ is the inverse T parameter of the transition, $\left[T_{t,SOL}^{-1}\right]$ are the T parameters extracted from the SOL calibration, and $[T_m]$ are the measured T parameters of the uncalibrated structure. Finally, a conversion from T- to S-parameters is performed, followed by a normalization to the transmission line impedance value.

4.3. Reflection Coefficient Characterization

4.3.1. 1-Port SOL Calibration

Once SOL calibration kit has been utilized to calibrate until the probe tips, the earlier obtained two-port transition $[S_t]$ parameters can be used to de-embed from the 1-port calibrated data to the desired antenna reference plane. First, the $[S_t]$ is dissected into its constituent components: S^t_{11}, S^t_{21}, S^t_{12} and S^t_{22}. The input reflection coefficient Γ_L at the desired antenna reference plane is then obtained using [72]

$$\Gamma_L = \frac{\Gamma^{SOL}_{LL} - S^t_{11}}{\Gamma^{SOL}_{LL} \cdot S^t_{22} - \Delta}, \tag{4.2}$$

where Γ^{SOL}_{LL} is the 1-port reflection parameter of the antenna, after calibration with the SOL calibration algorithm and de-embedding of the two-port transition $[S_t]$ parameter. The factor Δ is given by

$$\Delta = S^t_{11} \cdot S^t_{22} - S^t_{12} \cdot S^t_{21}. \tag{4.3}$$

The 1-port S-parameters is then normalized to the transmission line impedance value (e.g. 64 Ω for CPW-fed antenna).

Applying the proposed approach to compute the input reflection coefficient of the antenna in the OTA setup, provides a significant reduction in the trace ripples when compared to the offline de-embedding approach, see solid blue trace in Fig. 4.8a. Moreover, the figure shows good agreement with the CST full-wave simulated data, with only a shift in the main resonance peak which is attributed to small variations in the fabrication and assembly process. As shown, a reflection coefficient below -10 dB is achieved over the 140-170 GHz band, with a bandwidth of 28% and 21% for CPW- and MS-fed antennas, respectively. The oscillations in both the simulations and the measurements are associated to the reflections in the shell lens.

Similarly, we wanted to apply this TRL technique to derive the S_{11} of the microstrip-fed antenna. Unfortunately, we could not apply the same three-step calibration process for the de-embedding of the landing probes in the MS case as we did for the CPW case because of the spurious radiation coming from the RF landing pads. Instead, the MS-fed AUT S_{11} will be obtained through the use of time-gating, described in the next section.

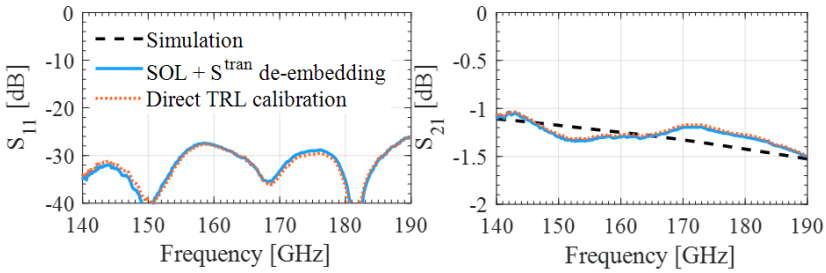

Figure 4.7: (a) S_{11}^{DUT} and (b) S_{21}^{DUT} extracted from the direct calibration and from the used two-step calibration process. Note in (a) the simulation is < -40dB.

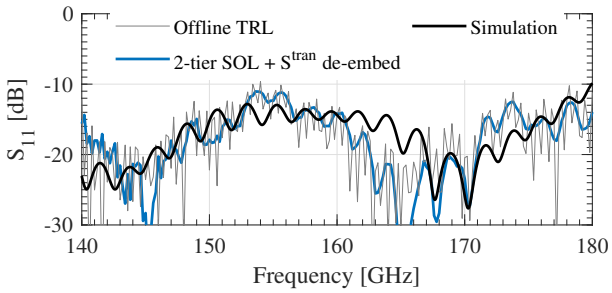

(a)

Figure 4.8: Measured reflection coefficient of the CPW-fed AUT, compared against full-wave simulations.

4.3.2. Antenna Calibration Seen from the Time-Domain

So far, calibration has been performed using frequency-domain metrics, which are applied naturally since the VNA is a frequency-domain-based measurement device. However, reconstruction of the time-domain using complex frequency-domain data can provide significant further insight in the applied calibration technique. For this reason, this section briefly analyses $S_{11}(t)$ by Inverse Fast-Fourier-Transformation (IFFT) of $S_{11}(f)$. It is important to remember that the Fourier transform assumes in time-domain an infinitely repeating periodical segment of time waveforms. This waveform length is related to the number of sample points taken and the measured bandwidth. In our case $\Delta t = 1/(190GHz - 140GHz) = 20$ ps. Therefore, with a total of 251 frequency bins, the total time span is set to 5 ns.

Fig. 4.9 shows the time-domain $S_{11}(t)$ after applying only the standard waveguide-based TRL calibration (i.e. reference plane A in Fig. 4.3b), thereby

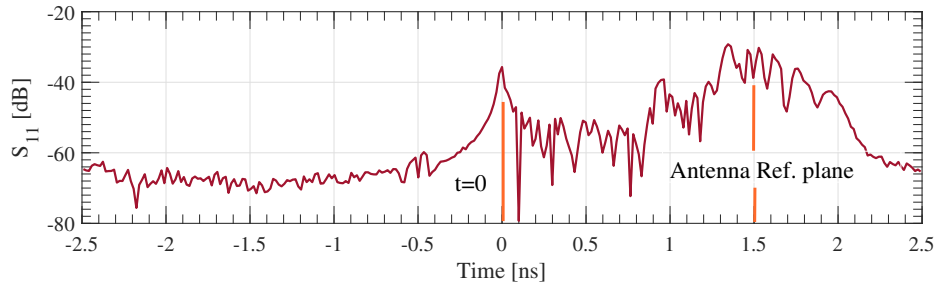

Figure 4.9: Time domain S_{11} of the CPW-fed Core-Shell lens antenna, before applying the on-wafer TRL calibration technique. Two time instances are labeled, indicating the waveguide flange and antenna reference plane propagation times.

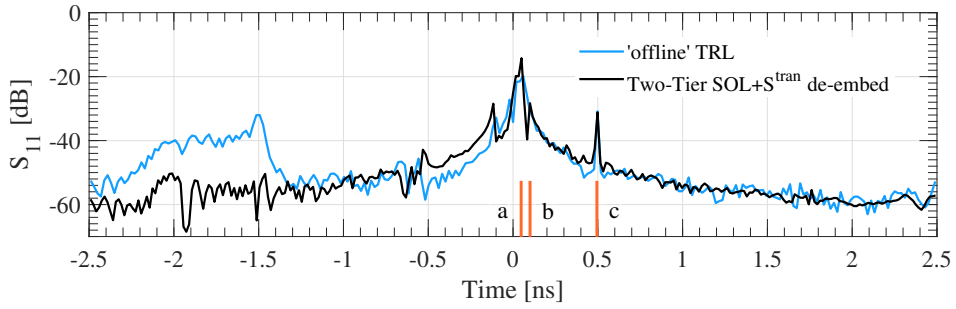

Figure 4.10: Time domain S_{11} of the CPW-fed Core-Shell lens antenna, after applying the on-wafer TRL calibration technique.

setting the time $t = 0$ at the frequency extender waveguide flange. Significant $S_{11}(t)$ spikes are visible even before reaching the antenna reference plane after about 1.5 ns (Ref. plane C in Fig. 4.3b), contributed by impedance mismatches inside and between the RF components. To make matters worse, any non-ideal frequency dispersion of the used components (such as the probes, waveguides, fused-silica transmission lines etc.), leads to group delay in the time-domain. Therefore, the AUT characterization will suffer from such unwanted effects.

To solve the problem, both the 'offline' TRL and proposed two-tier SOL with S_t de-embedding are performed, and their time-domain equivalents are presented in Fig. 4.10. As shown, The time frame $t = 0$ is successfully shifted to the antenna reference plane, and the AUT $S_{11}(t)$ has more clearly identifiable peaks due to the removal of group delay effects. Three of such peaks are marked in Fig. 4.10: a represents the reflections at the double-slot at ≈ 50 ps, b is the core lens interface at ≈ 100 ps, and finally c is the shell lens interface to free-space at ≈ 500 ps. These values are within the expected time range, given the time resolution of 20 ps and the electrical length (taking into account physical dimensions and material permittivies) of the components.

Although the 'offline' TRL and two-tier SOL calibration techniques appear similar, a large difference of more than 20 dB is observed at time intervals of -2.5 and -1.5 ns. This time interval corresponds to an improper calibration of the waveguide flange ($t = 0$ in Fig. 4.9). The reason for this is that the 'offline' calibration unjustifiably assumes that the calibration performed in another setup could be transferred to a different setup, where the components are interconnected differently by mechanical tolerances. The inaccuracy of the method then results in significant AUT measurement errors, as was shown in Fig. 4.8a.

Apart from the SOL-calibration, one other technique to is the use of time-gating, where only the time-instances related to the AUT are kept, while the rest of the time domain is negated. The results of such procedure are discussed in the next section.

4.3.3. Time-Gating technique for S_{11} Calibration

From the time-domain $S_{11}(t)$, calibrated by the 'offline TRL' of Fig. 4.10, the erroneous time samples can be set to zero, thereby removing the invalid data points caused by the faulty calibration. The time gate is set from 0 ns, the start of AUT reference plane, to 1 ns, a value well beyond the shell lens outer interface. The result of this time gating, shown in Fig. 4.11a, is compared to the SOL calibration method described earlier. As shown, the time-gating approximates well the behavior of the antenna $S_{11}(f)$, and therefore provides a good alternative to time-consuming SOL calibration.

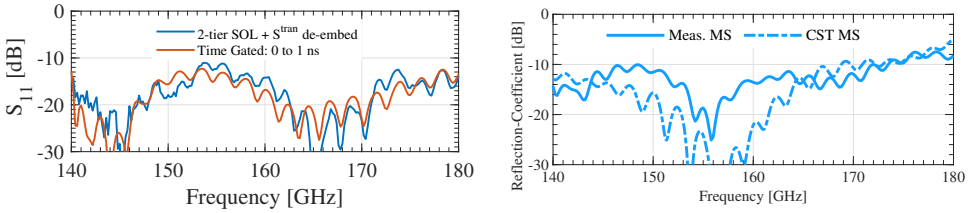

Figure 4.11: Measured reflection coefficient of the (a) CPW-fed and (b) MS-fed AUTs, compared against full-wave simulations. The measured results have been obtained using time-gating.

The resulting $S_{11}(f)$ of the MS-fed antenna, shown in Fig. 4.11b, is based on the same time-gating technique, using the 0-1 ns interval. Its $S_{11}(f)$ amplitude is several dBs higher than the full-wave simulation but shows overall similar behavior.

4.4. Gain Estimation in the Near-Field

Accurate calibration of absolute gain measurements proves to be a substantial challenge in near-field setups, particularly in the context of probe-fed antennas. First, good phase stability is imperative to enable a near- to far-field transformation [73]. Furthermore, extracting the gain of the AUT using the Friis' transmission equation is not feasible in this scenario, as the RF radiated power spreading does not follow the square of the distance.

In this contribution, instead of relating the power received by the AUT with a standard gain antenna as in [74], we propose to compare the measured power with the simulated or estimated power received by the AUT. The proposed strategy to extract the far-field gain from the measured S-parameters relies on first extracting the far-field directivity $D_{FF,meas}$ via a near-field to far-field transformation. Then, two near-field methods based on measurements only (Section 4.4.2), and semi-analytical methods (Section 4.4.3) are used to obtain a good estimation of the near-field radiated power spreading as a function of distance, and subsequent antenna loss. The gain of the AUT will then be derived from $G_{FF,meas} = D_{FF,meas} - L$, see section 4.4.4. The next section provides more detail on obtaining $D_{FF,meas}$. Finally, sections 4.4.2 and 4.4.3 describe two different methods of how this loss term L was obtained.

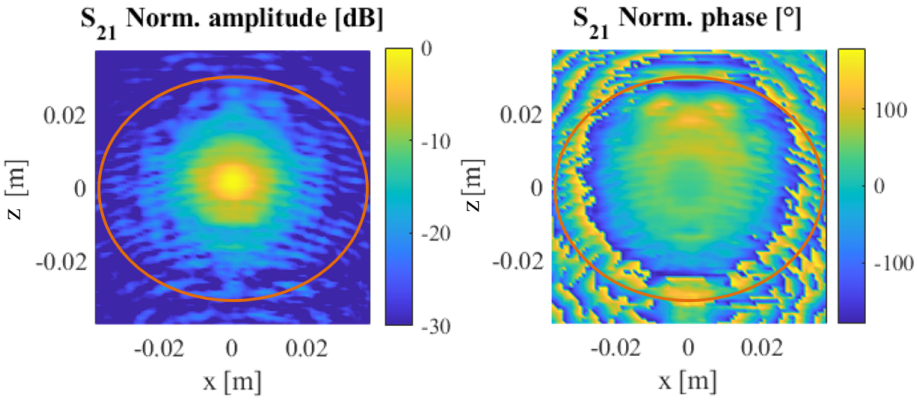

Figure 4.12: (a) Measured S_{21} (Electric field) amplitude in the scan plane with the projected mirror aperture outlined (red circle). (b) Same S_{21} but now in phase format.

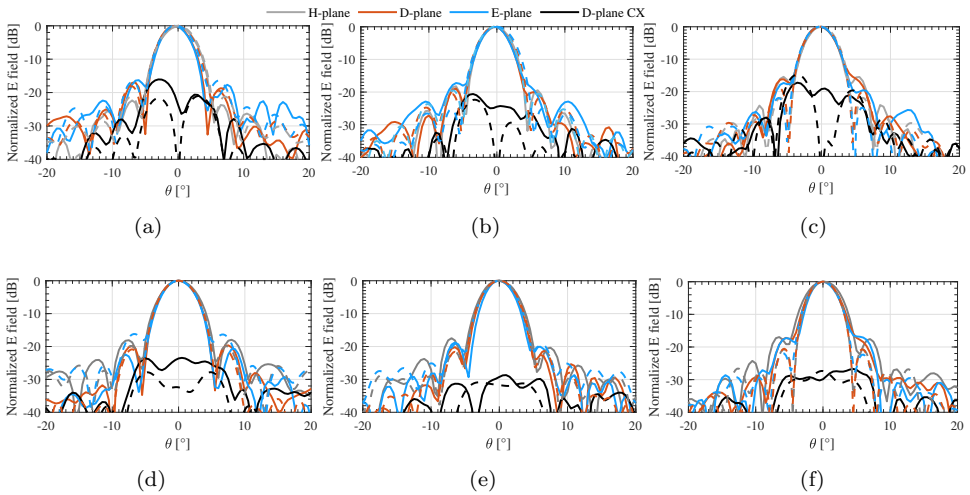

Figure 4.13: Measured (solid) vs simulated (dashed) far-field patterns for CPW-fed (a-c) and MS-fed (d-f) antennas. Three frequencies are shown: 140GHz (a, d), 155GHz (b, e), and 170GHz (c, f).

4.4.1. Measured Far-Field Radiation Patterns and Directivity

The radiation pattern of the antenna was measured in the near-field with the setup of Fig. 4.1. The near-field measurement plane, located at a distance of 8.8 cm from the tip of the lens, covered an area of 8 × 8 cm and was sampled with a step

size of 0.88mm (corresponding to $\lambda_0/2$ at the maximum measurement frequency of 170 GHz). The electric field amplitude on the measurement plane at 155 GHz is shown in Fig. 4.12. The lens aperture diameter of 3 cm contains most of the field. The area between the lens aperture and the projection of the mirror, outlined in red, shows some (minor) diffraction effects probably due to the edges of the mirror. Furthermore, the S_{21} phase, shown in 4.12b is slightly offset due to a misalignment in the mirror. This effect will be compensated for mathematically using a phase correction.

The far-field radiation patterns were obtained using a near-field to far-field transformation and Ludwig-3 definition [44], shown in Fig. 4.13. We note a good agreement with the simulations. The cross-polarized field was measured using a 90° waveguide twist and also presents an excellent agreement with the simulation (see trace D-plane CX). The far-field directivity of the extracted far-field patterns is shown in Fig. 4.17 for the CPW-fed antenna, achieving an agreement within 1dB across the 140 - 170GHz band. This variation can be attributed to the truncation effects of both the mirror and the finiteness of the near-field measurement plane.

4.4.2. Estimation of the Antenna Loss Using Only Near-Field Measured Data

This subsection derives the near-field directivity and gain solely based on measurement data, using a method derived from [74]. First, the directivity is derived from the measured S_{21} parameter by

$$D_{NF} = \frac{|S_{21}|^2}{2\eta} \frac{R^2}{P_{rad}/4\pi}, \tag{4.4}$$

where η is the impedance of free space, R is the distance from the shell antenna and the measurement plane, and P_{rad} is the power radiated in the measurement plane. The latter is calculated using

$$P_{rad} = \iint_S \frac{|S_{21}|^2}{2\eta} dxdz, \tag{4.5}$$

where dx and dz are the step sizes in the measurement plane along x and z respectively, both 0.83mm. The measured near-field gain is then expressed by

$$G_{NF} = \frac{|S_{21}|^2}{G^{pr}} \left(\frac{4\pi R}{\lambda}\right)^2, \tag{4.6}$$

where G^{pr} is the probe gain, characterized through a far-field link measurement. Fig. 4.14 shows these near-field gains and directivities for both CPW-fed (a) and MS-fed (b) antennas, and are compared to simulations, described in the next section.

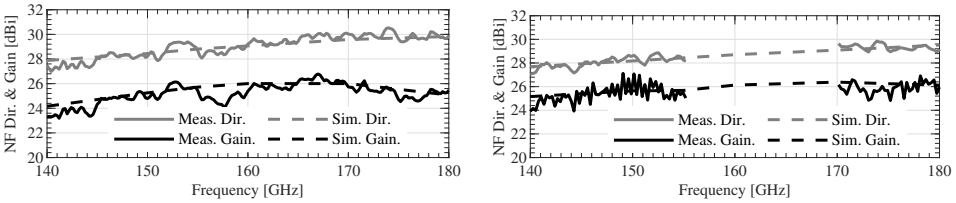

Figure 4.14: Near-field directivity (gray) and near-field gain (black) for both the CPW-fed (a) and MS-fed (b) antennas.

Due to the resonance effect in the MS-fed antenna landing pad, explained in Section 4.3, the gain could not be derived in the 155-170GHz bandwidth, as shown in Fig. 4.14b. The measured near-field gain is compared with the full-wave simulation that includes the ohmic/dielectric loss showing a good agreement within 1 dB in the 140-170GHz bandwidth. Note that the simulations do not include the effect of the multiple reflections at the lens antenna interfaces, which may be the cause of the rippling not present in the simulated directivity and the gain. Furthermore, the measured higher rippling effects observed in the gain may be attributed to the scattering effects produced by the mirror edge and the aforementioned truncation of the near-field measurement plane.

Note that the results of Fig. 4.14 represent the near-field directivity and gain. Located in the radiative near-field, they will be dependent on measurement distance. The translation to far-field gain can be made by extracting the antenna loss in the near-field, and is obtained by subtracting the measured near-field gain from the measured near-field directivity:

$$L = D_{NF} - G_{NF}, \tag{4.7}$$

which will be used in Section 4.4.4 to derive the far-field gain.

4.4.3. Estimation of the Antenna Loss Using Simulated Near-Field Power-Spreading

Contrary to the previous section, where the near-field power spreading was derived using measurements only, this section estimates the power spreading by simulating the near-field propagation from the lens to the measurement probe. When the AUT suffers from strong back-side radiation and radiation towards large angles, the estimation of the near-field power spreading through simulations allows us to

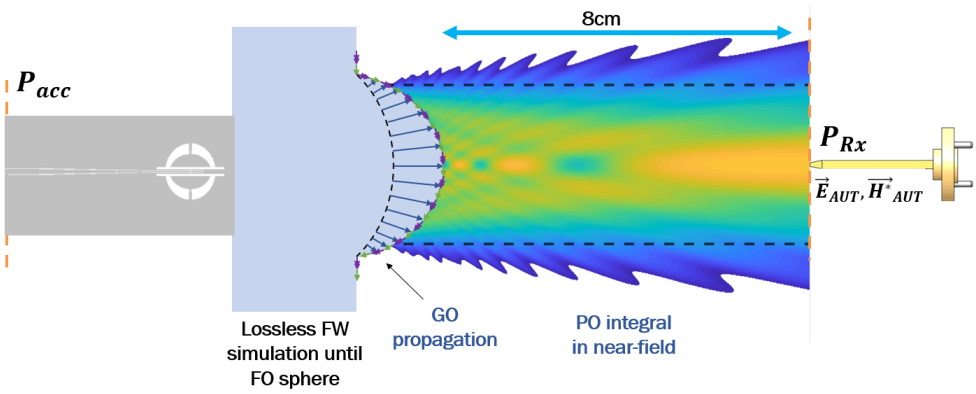

Figure 4.15: Simulated near-field propagation from the antenna reference plane (where P_{acc} is derived), to the probe tip at a distance of 8.8cm from the elliptical lens.

understand and assess better the radiation of the antenna in the measurement scan plane.

As mentioned, to extract the gain, the measured transmission coefficient will be related to a loss-less simulation of the transmission of the lens AUT on the measurement plane. The simulated S_{21}^{sim} parameter can be expressed as

$$|S_{21}^{sim}|^2 = P_{RX}/P_{acc}, \tag{4.8}$$

where P_{RX} is the power received at the waveguide probe tip and P_{acc} is the accepted power by the AUT, given by $P_{acc} = P_{TX}(1-|S_{11}^{sim}|^2)$. P_{TX} is the power transmitted in the simulation. The power received is calculated as the integration of the Poynting vector $\vec{S_y}$ over the area of interest,

$$P_{RX} = \iint \vec{S} \cdot \hat{n} dS, \tag{4.9}$$

where $\hat{n} = \hat{y}$, is the unit vector normal to the surface S. Since the lens is designed to generate a plane-wave-like field in front of the aperture, we assume that the Poynting vector only has a y component, i.e. $\vec{S}=\hat{y}S_y$. This assumption means that measurement post-processing will not include any probe compensation (the same assumption was applied in Section 4.4.2). Since the amplitude-level variation of the probe is only 0.15dB within $\pm 10°$ (at 180GHz), the validity of this approximation is good for such an electrically large lens, where the dynamic range of the measurement was >30dB (see Fig. 4.12). With this assumption, the received power is calculated as

$$P_{RX} = \Re\{S_y\} A_{eff}, \tag{4.10}$$

where S_y is the amplitude of the Poynting vector, $\vec{S_y} = 1/2\vec{E} \times \vec{H}^*$ at the measurement plane, in this case at 8.8 cm distance, and A_{eff} is the waveguide probe (broadside) effective area, given by $A_{eff} = (\lambda_0^2 G_{pr})/4\pi$. To obtain $\vec{S_y}$, first, a full-wave simulation of the antenna radiating in the lens medium is performed, without considering any ohmic or dielectric loss. After this simulation, the electric and magnetic fields on the lens surface are approximated using physical optics and are propagated to the scan plane of the same area and distance as the one measured. The overview of the simulated power spreading is shown in Fig. 4.15, indicating that negligible power spreading occurs (marked with the dotted lines), giving validity to the assumption in (4.10). This simulation method was used to obtain the simulated near-field directivity and gain, shown in Fig. 4.14.

Finally, the antenna loss L is estimated by

$$L = |S_{21}^{sim}|^2 - |S_{21}^{meas}|^2, \tag{4.11}$$

where S_{21}^{meas} is the measured transmission coefficient, and S_{21}^{sim} is the simulated ideal (i.e. no ohmic or dielectric loss) transmission of the same AUT at a fixed distance of 8.8cm, located in the radiative near-field of the AUT. The S_{21} parameters are shown in Fig. 4.16, the difference in amplitude being the antenna loss.

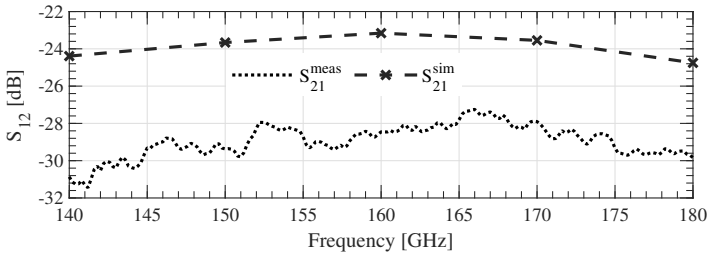

Figure 4.16: S_{21} parameters of the near-field measurement and near-field simulation, used to derive the antenna loss term L.

4.4.4. Estimation of the Far-Field Gain

For calibration of the two described methods in Sections 4.4.2 and 4.4.3, first the raw S-parameters S^{AUT} are obtained when the waveguide probe is aligned at the broadside position with the lens. Then, the S_{21}^{meas} are obtained by de-embedding the transition until the antenna plane (Fig. 4.3b). Similar to Section 4.3, SOL calibration with S_{tran} de-embedding is performed to move the reference plane from the waveguide to the AUT. The resulting S_{21}^{meas}, after removing

the reflection coefficients of the AUT and the waveguide probe, is expressed by $|S_{21}^{meas}|^2 = |S_{21}^{AUT}|^2/(1-|S_{11}^{AUT}|^2)$. The resulting losses obtained in sections 4.4.2 and 4.4.3 are subtracted from the earlier measured far-field directivity,

$$G_{FF}(dB) = D_{FF}(dB) - L(dB), \tag{4.12}$$

to arrive at the estimated far-field antenna gain shown in Fig. 4.17 for the CPW-fed antenna. Good agreement between simulated and measured far-field directivities and gain is observed. For very directive antennas with high front-to-back ratio as in this case, both near-field measurement techniques provide a good estimation of the antenna characteristics.

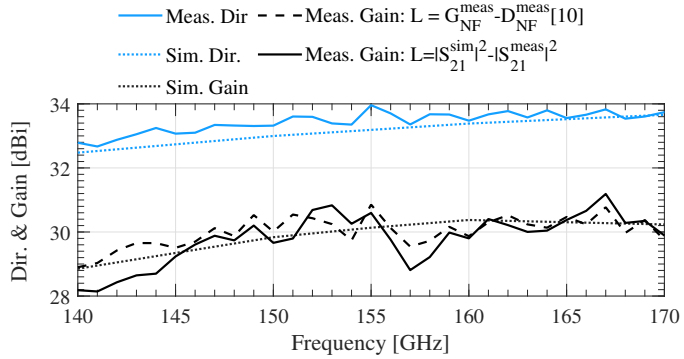

Figure 4.17: Far-field gain and directivity for the CPW-fed antenna as a function of frequency. The directivity is obtained directly through near-field to far-field conversion. The gain is compared using two methods, described in sections 4.4.2 and 4.4.3

4.5. Flat Lens Measurements

Using the same approach as above, the flat core lens of Chapter 3 is now measured for its reflection coefficient, directivity and gain. The prototype is added to the same dual-lens assembly of Chapter 2, as was shown in Fig. 3.14. Because the measurement setup and lens design are, apart from the flat interface, identical to the one presented in previous section 4.2, we can directly compare the measured results to those obtained with the spherical core lens.

Fig. 4.18 shows the measured antenna reflection coefficient of the flat lens, compared to the spherical lens. No time-gating is applied. Contrary to Fig. 3.10, the measurements include the CPW transmission lines. The two measurement

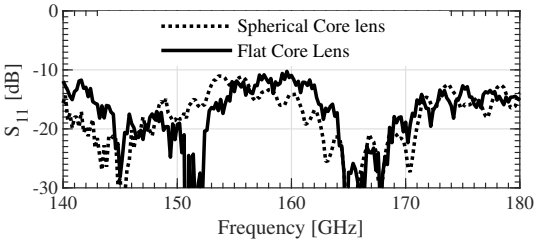

Figure 4.18: Measured S_{11} of the flat lens (solid) and the spherical lens (dashed).

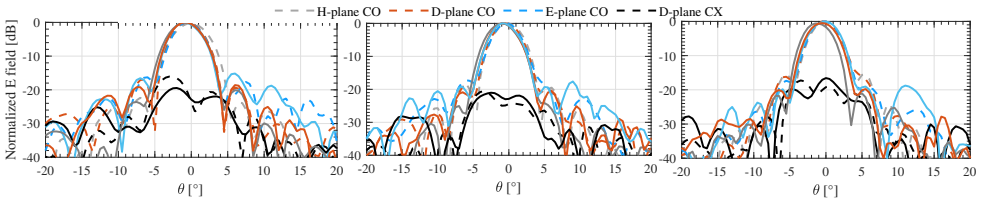

(a) (b) (c)

Figure 4.19: Measured free-space secondary patterns of the flat lens (solid) compared to the patterns of the spherical core lens (dotted). (a) 140 GHz (b) 155 GHz and (c), 170GHz comparing the flat lens (solid) versus the spherical lens (dashed).

sets indicate fair agreement, although the flat core lens introduces some additional ripples.

Next, the antenna patterns were obtained by measuring the 2D near-fields, and subsequently applying a near-field to far-field conversion. Again, the measurement setup and 2D scanning plane were kept as identical as possible to 4.2, to allow for fair comparison.

Fig. 4.19 shows the far-field patterns of the flat lens (solid), compared to the spherical lens of Chapter 2 (dashed). Three main observations can be made. First, good agreement in the main beam pattern is obtained, although a minor shifting in scanning direction has occurred for the flat lens ($\approx$ -0.5°). This is likely due to a misalignment in the measurement setup. Second, a higher sidelobe is visible in the E-plane at $\theta \approx$10°, particularly at 155GHz. This asymmetry is most likely caused by the interaction between the flat lens and the radiating CPW transmission line. This effect has not been included in the full-wave simulations of section 3.3 due to computational intensity. Finally, we note in Fig. 4.19 that the cross-polarization levels show good agreement across frequency for both lenses.

Having obtained the measured far-field patterns, the directivity and gain can be extracted. The directivity follows directly from the patterns, and is shown in Fig.

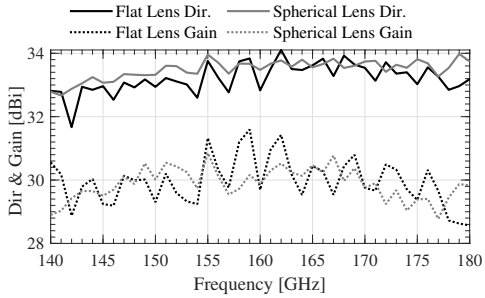

Figure 4.20: Measured far-field directivity

4.20. The flat and spherical lenses show similar directivity values across frequency, although the former has somewhat higher rippling behavior. Using the same process as in Section 4.4, the resulting far-field gain is shown in Fig. 4.20. Oscillations of up to 1dB are observed for the flat lens, with overall values close to the spherical lens. Unfortunately, the CPW feeding line (inset of Fig. 3.14) has large radiation loss, as was found in Chapter 2. This stray radiation could couple into the flat lens interface and cause unwanted radiation. An improved feeding line, such as the microstrip-based design of Chapter 2, could help resolve this issue. Despite these losses, decent radiation efficiency of around -3dB is obtained, in close agreement to the value found in Chapter 2, where a feed loss of 1.2 dB was found, lens dielectric loss of only 0.5 dB, and the rest associated to spillover and front-to-back loss. This illustrates the advantage of the dual-lens design, where the compact core lens limits dielectric loss, and permits the transition to electrically-large lenses with negligible loss.

4.6. Conclusion

This chapter presented a measurement strategy to accurately characterize probe-fed high-gain antennas operating in the sub-THz band. By using an adjustable 45° flat mirror, the radiation of the AUT is redirected to a measurement in the x-z plane, which allows separate optical tables for the mechanical scanner and the RF probe station, thereby minimizing vibrations to the AUT. Calibration and modeling techniques to transfer the calibration accuracy of a two-port TRL to a one-port SOL calibration were used. They enable an accurate input reflection coefficient measurement at the antenna input plane. The antenna gain was extracted directly from one set of measurements and one simulation.

All these techniques have been corroborated with a set of measurements compared against simulations in the 140-170GHz band. Two measured prototypes showed good agreement with simulations, with antenna directivities >32 dBi and loss <2dB in the 140-170 GHz bandwidth, validating the proposed architecture and choice of technologies.

The flat lens of Chapter 3 was compared to its spherical counterpart. Good agreement in antenna performance, such as reflection coefficient, radiation patterns, directivity and gain was obtained. The lens suffered from larger rippling effects than the spherical lens, but improved lens feeding design could help mitigate this problem.

Chapter 5

Flat Hyperboloid Lens With Leaky-Wave Feed for Material Characterization at WR-5 Frequencies

This chapter describes the design of sub-Terahertz lens antennas that are coupled in the near field. The lenses have a flat interface, making them suitable for material characterization under plane wave incidence. A waveguide-based leaky-wave antenna feed illuminates efficiently the lenses with a Gaussian pattern over a bandwidth of 140 to 220 GHz. Then, a large permittivity hyperboloid lens converts the feed pattern into a plane wave with high Gaussicity. The use of dense dielectric materials significantly reduce field spreading effects, when compared to setups with free-space propagation. Furthermore, the final lens architecture presents a flat interface, enabling direct lens-to-lens coupling for 2-port measurements with only -3 dB of coupling loss. This way, a quasi-optical Thru-Reflect-Line calibration can be performed, thereby making accurate extraction of material properties via full S-parameter matrix possible. Two materials were studied with this technique in a full-wave simulation, showcasing errors below 1 percent for permittivity and 2 percent for loss tangent, using a standard plane-wave propagation model.

5.1. Introduction

MATERIAL characterization in the sub-terahertz frequency spectrum presents promising new opportunities. Accurate, non-invasive material parameter extraction in this frequency band enables a variety of different applications, with examples including security, industrial material quality and defect detection, and air quality detection [4, 75–77]. Furthermore, accurate material characterization is key to designing and optimizing Radio Frequency (RF) systems, as their performances rely heavily on the properties of the involved materials. For these reasons, material characterization in these bands is met with growing interest, and a variety of different measurement techniques have been proposed.

At frequencies < 300 GHz, a popular approach is using a Vector Network Analyzer (VNA) for material characterization. Here, frequency-domain S-parameter matrices are compared to an analytical model for extraction of complex permittivity values [78]. Rectangular waveguides in particular offer a controlled single-mode environment, in which a highly accurate Thru-Reflect-Line (TRL) calibration can be performed [79–81]. Unfortunately, the technique is no longer non-invasive, as the Material-Under-Test (MUT) needs to be adjusted to fit in the waveguide assembly. This becomes increasingly difficult at higher frequencies, where the waveguide dimensions are smaller. Free-space material characterization techniques are therefore preferred for their flexibility [82].

Above frequencies of 300 GHz, a commonly encountered technique for free-space material characterization is terahertz Time-Domain Spectroscopy (TDS) [83–86]. It uses a wide-bandwidth system to obtain the sample permittivity, by extracting the time-domain propagation delay through the sample. However, TDS systems do not provide full S-parameter matrices, and can therefore not be used in high-accuracy calibration techniques (e.g. TRL). Therefore, many recent works have explored sub-THz (100 - 300 GHz), VNA-based free-space measurement setups [75, 82, 87–92].

However, contrary to the use of rectangular waveguides, in free-space measurement setups there is no well-defined mode with single direction of propagation. This causes a limitation in accuracy when extracting the complex permittivity using analytical models, since they rely upon the assumption of a plane-wave incidence on the dielectric sample.

Therefore, efforts have generally focused on developing Quasi-Optical (QO) measurement setups, where the fields approximate the plane-wave condition using Gaussian beam optics [75, 82, 87–92]. This well-known concept is illustrated in Fig. 5.1a. However, the plane-wave condition is met only at the Gaussian beam waist for a limited Depth-of-Focus (DoF), where the phase front resembles a plane wave. Large F-number optics, that require careful alignment in position and orientation, are required to enlarge the DoF [93]. This in turn requires the QO system to trade off its compactness for a larger DoF.

To counteract this problem, recent efforts have also attempted to adapt the analytical models to include the field spreading effects [87, 90]. Nevertheless, the

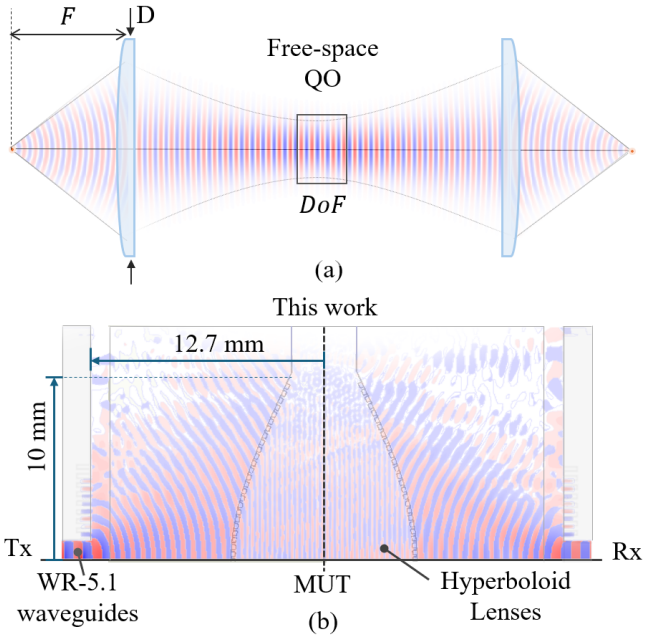

Figure 5.1: (a) Conventional free-space quasi-optical approach using focused Gaussian beams, relying on a narrow Depth-of-Focus (DoF). (b) Proposed quasi-optical material characterization system. The Material-Under-Test (MUT) is positioned in between the two waveguide-fed hyperboloid lenses.

reliance on low field spreading conditions complicates the modeling and decreases the accuracy that such systems can achieve. In addition, the use of standard horn antennas required further calibration to account for the frequency dispersion of the phase-center [87].

To face these challenges, this work proposes a compact lens design with a flat interface. The lens generates directly a high-purity plane wave in a dense dielectric medium with low amplitude spreading and low phase dispersion. Instead of field propagation through air, the dense medium helps suppress the field spreading effects. This way, accurate free-space material characterization using a VNA in the WR-5 band (44 % bandwidth) can be achieved. The lens design is shown in Fig. 5.1b, and consists of a low loss $\varepsilon_r = 2.3$ dielectric, and a high density $\varepsilon_r = 9.3$ thermoplastic. The lenses can be mounted on a WR-5 waveguide, and are calibrated using an accurate TRL approach. We demonstrate the material characterization with a standard plane-wave model, placing no emphasis on additional compensation with analytical spreading models. Furthermore, the flat interface allows the MUT to be

clamped in between the Tx and Rx antennas, thereby enabling a simple assembly and a reduction in angular misalignment.

This work is structured as follows. Section 5.2 describes provides an in-depth discussion on the used Gaussian propagation model, the design of the flat lenses. Then, Section 5.3 provides a full-wave simulation analysis of the designed lens, validating the claims made in Section 5.2. Finally, Section 5.4 describes the method to characterize materials using the established lens architecture, and two example cases are demonstrated.

5.2. Lens Antenna Design

This section describes the design and modeling process for the lens architecture. It starts by modeling the electric field propagation using Gaussian beam theory. Then, the leaky-wave feed that illuminates the lens is analyzed, followed by the actual hyperboloid lens design.

5.2.1. Gaussian beam propagation

In the first step, some a priori information on the Gaussian wave-front propagation is modeled. This helps us establish a relationship between the lens aperture dimensions and the MUT sample thickness.

As mentioned in the introduction, standard dielectric measurements rely on a transmission line model that assumes plane wave incidence. However, the generated plane wave will diverge as a function of distance, developing an increasingly large beam waist with a larger radius of phase-front curvature. MUT samples with large thickness can therefore suffer from increased electric field spreading and lower coupling.

To assess the impact of such spreading effects, we model the field propagation using a standard Gaussian model [94]. First, the Gaussian beam width can be modeled using

$$w(z) = w_0 \sqrt{1 + \left(\frac{z \lambda_d}{\pi w_0^2} \right)^2}, \tag{5.1}$$

where λ_d is the wavelength in the dielectric medium, z is the propagation distance, and w_0 is the beam waist at $z = 0$. An example w_0 of 5 mm is used, corresponding to 3 λ_0 at 180 GHz. Similarly, the radius of curvature is calculated using [94]

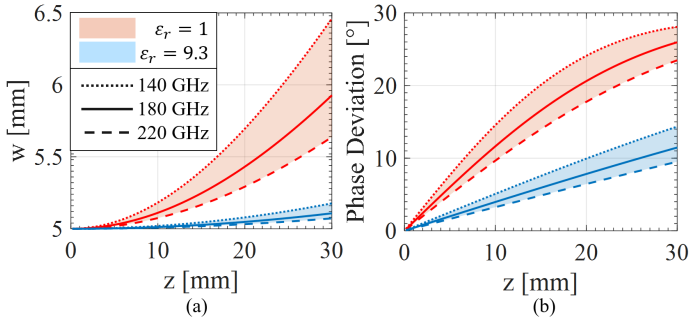

Figure 5.2: (a) Gaussian beam width w as a function of distance z. Two values for permittivity are indicated, plotted against the WR-5 frequency band. (b) The angular deviation from a plane wave, based on the radius of curvature.

$$R(z) = z + \frac{1}{z}\left(\frac{\pi w_0^2}{\lambda_d}\right)^2. \tag{5.2}$$

From the radius of curvature then follows the phase deviation from an ideal plane wave, defined by [95]

$$\Delta\Phi(x, y, z) = \frac{k_d \rho^2}{2R(z)}, \tag{5.3}$$

where k_d is the wave number in the dielectric medium and ρ defined as $\rho = \sqrt{x^2 + y^2}$.

Fig. 5.2a shows as an example the propagation of the Gaussian beam as a function of distance z, whereas Fig. 5.2b shows the phase deviation at $\rho = w_0 = 5$ mm. A frequency bandwidth of 140 GHz to 220 GHz is indicated. As expected, diffraction effects cause the initial plane-wave fronts to diverge, creating a widening of the beam width (Fig. 5.2a). The divergence also causes the wave-fronts to curve away from the central axis, causing increasing phase deviation to occur (Fig. 5.2b).

When comparing the spreading in vacuum ($\varepsilon_r = 1$) to that in our proposed ($\varepsilon_r = 9.3$) medium, the former presents a significantly larger spread over distance due to the factor $\sqrt{9.3}$ smaller electrical size of w_0. This is especially true for the lower frequency bound of the bandwidth (dashed line), where the beam width is electrically smaller.

Based on this modeled behavior, it is apparent that by confining the Gaussian beam within a medium of high ε_r, a significant decrease in spreading over distance can be achieved. The distance z can be connected to the maximum MUT thickness, by estimation of the number of multiple reflection required to reach convergence conditions. For example, $\varepsilon_r = 1$ samples with a thickness of 3 mm can be analyzed with 26° phase deviation on the 5^{th} back-and-forth reflection (total 30 mm). By

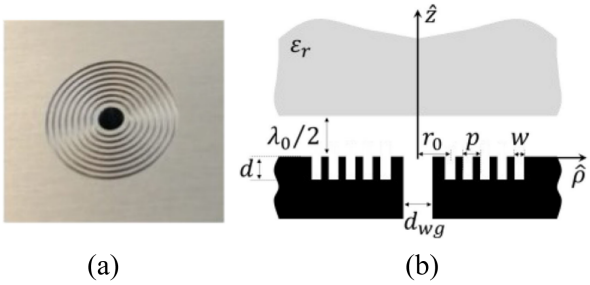

Figure 5.3: Elliptical lens antenna with leaky-wave feed, including a corrugated annular ring ground plane, taken from [23].

comparison, the denser $\varepsilon_r = 9.3$ reaches an 11° phase deviation over the same distance. The phase deviation can be further reduced by enlarging the lens D_L, thereby enlarging the Gaussian beam waist.

5.2.2. Leaky-Wave Feeding Antenna

The lens feed is of critical importance to the generation of the high-purity plane waves. Illumination of the two lenses requires a high degree of rotational symmetry and low cross-polarization levels (CX). The primary patterns should introduce an amplitude taper to avoid significant diffraction effects at the lens edges. In addition, for the generation of plane waves over a wide bandwidth, a near-constant phase center location is required. These already challenging properties must persist over a wide bandwidth, from 140 GHz to 220 GHz. Therefore, a specially designed feeding antenna is required that meets these criteria.

Fortunately, such feeding antenna was developed in earlier work in [23], shown in Fig. 5.3. In that contribution, an elliptical ε_r=2.3 High-Density Polyethylene (HDPE) dielectric lens is positioned above an open-ended circular WR-5 waveguide. The two are separated by a $\lambda_0/2$ cavity. This structural combination enables the propagation of nearly-degenerate TM_1 and TE_1 leaky-wave modes. The non-dispersive TM_0, that is associated to high CX levels, was attenuated by the addition of circular corrugations around the waveguide. The result was an antenna feed that enables highly aperture efficient lens illumination, operating over the full WR-5 bandwidth (140 GHz to 220 GHz).

The feeding antenna was analyzed whilst radiating in infinite HDPE medium, to obtain the feed performance. Fig. 5.4a shows the normalized amplitude patterns of such feeding antenna. Indicated are the central frequency, and the lower- and upper-bounds of the WR-5 bandwidth. Its normalized E-fields are amplitude

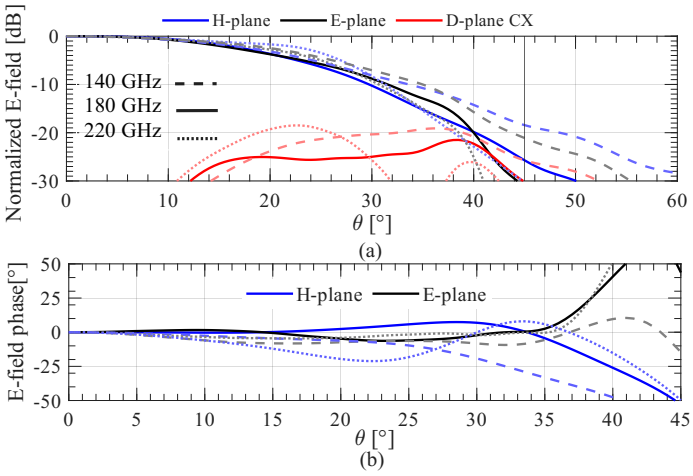

Figure 5.4: Simulated primary patterns of the corrugated circular waveguide with leaky-wave feed of [23]. (a) The normalized far-field amplitude distribution for the E- and H-planes, including the D-plane cross polarization. Three frequencies are included representing the WR-5 bandwidth. (b) The phase distribution using the same nomenclature of (a).

tapered towards a level of around -20 dB at 40°. Similarly, Fig. 5.4b shows the phase stability of the feeding antenna as a function of observation angle θ. Up to $\theta = 30°$, the phase ϕ remains constant between $-25° < \phi < 15°$. Beyond $\theta = 30°$, the amplitude tapering of Fig. 5.4a avoids large impact of phase deviations on lens performance. Finally, the feeding antenna features low S_{11} reflection parameter over bandwidth. The result is shown in Fig. 5.5. The low S_{11} is key to reducing multiple reflection in the lens setup.

5.2.3. Hyperboloid Flat Lens Design

Based on the knowledge of the feeding antennas and the Gaussian beam model, a lens architecture with a flat interface could now be designed. Given the $\varepsilon_r = 2.3$ of the leaky-wave feed, the second material made of $\varepsilon_r = 9.3$ PREPERM PPE950 thermoplastic was chosen for two reasons. First, the material was well characterized at high frequencies in Appendix B, with a loss tangent $\tan\delta = 0.005$ at the WR-5 frequency band. Second, the material offers a good contrast from the HPDE, which is needed to refract the RF wavefronts whilst limiting the lens curvature. Limiting this curvature helps in implementing a matching layer later on.

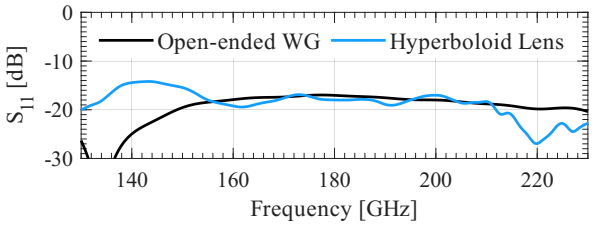

Figure 5.5: Simulated S_{11} of the open-ended corrugated waveguide of [23], compared to the proposed hyperboloid lens. Both S_{11} curves are normalized to the waveguide characteristic impedance ($Z_c = 456\Omega$).

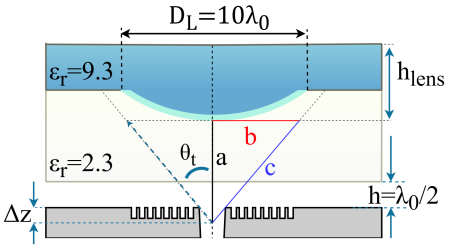

Figure 5.6: Geometry of the lens with flat interface. In blue, the convex hyperboloid lens made of dense thermoplastics. Below, the HDPE concave lens that supports the leaky-wave propagations in its air-filled cavity. The matching layer is located in between, indicated in cyan.

Once the material selection was made, the lens topology was based on the available feed pattern and the flat interface requirement. Because the wavefronts travel from an $\varepsilon_r = 2.3$ to a more dense $\varepsilon_r = 9.3$ material, a transition towards a convex lens was required. Canonical hyperboloid lenses are a well-known type of lens to convert an incoming Gaussian radiation profile to parallel rays, e.g. a plane wave. The proposed lens architecture is shown in Fig. 5.6. The convex hyperboloid $\varepsilon_r = 9.3$ lens is positioned inside a concave cavity of the $\varepsilon_r = 2.3$ HDPE lens.

To suppress multiple reflections within the lens design, a Matching Layer (ML) is introduced in between the interfaces of the two lenses. The same $\varepsilon_r = 4.6$ synthesized material will be used as in Chapter 2. In this work, we assume the ML is made of a homogeneous material with a thickness of $\lambda_m/4$, where λ_m is the wavelength in the matching layer.

The hyperboloid lens topology can be modeled using standard hyperbola equations. The degree of lens curvature is determined by the material eccentricity $e_c = \sqrt{e_{r2}/e_{r1}}$, which is a function of the ratio of permittivities between the two mediums. The lens focal length is given by

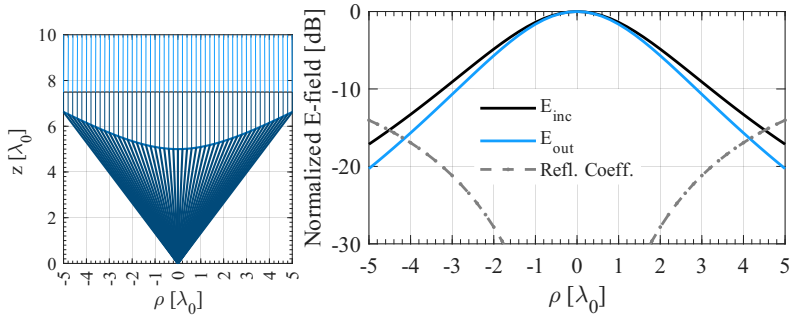

(a) (b)

Figure 5.7: (a) Ray tracing for the hyperboloid lens. The rays emanate from the phase center at $z = 0$. (b) Incident E-field amplitudes at the hyperboloid surface E_{inc} and at the flat lens-air interface E_{out}. The reflection coefficient is indicated in dashed lines.

$$F = \frac{D_{\text{L}}}{2\tan(\theta_t)}, \tag{5.4}$$

where θ_t is the lens truncation angle and D_L is the lens diameter. From here, the semi-major axis a is calculated using

$$a = \frac{F}{1 + e_c}. \tag{5.5}$$

Multiplying the semi-major axis with the lens eccentricity, the linear eccentricity c is obtained using $c = a \cdot e_c$. Both terms can then be combined to form the lens semi-minor axis $b = \sqrt{c^2 - a^2}$. Finally, these parameters enable the mathematical definition of the lens surface vertical coordinate z using

$$z = a\sqrt{1 + \frac{\rho^2}{b^2}} + c. \tag{5.6}$$

Based on this lens parameterization, a lens truncation angle $\theta_t = 45°$ was chosen to capture the feed primary patterns with sufficient spillover efficiency, whilst including a large amplitude taper to diminish diffraction effects at the lens edges (Fig. 5.4). Then, a lens diameter $D_L = 10\lambda_0$ was chosen to have the same 10 mm waist as was analyzed before, and to provide a good trade-off between lens thickness and aperture size. For structural strength, a sufficiently large h_{lens}= 4.16 mm ($2.5\lambda_0$) was needed, as the PPE950 material can flex under mechanical stress.

After the lenses satisfy the above mathematical conditions using the stated geometrical parameters, a ray tracing approach can be implemented to confirm that the feeding rays refract to parallel outgoing rays. Fig. 5.7a shows the ray tracing

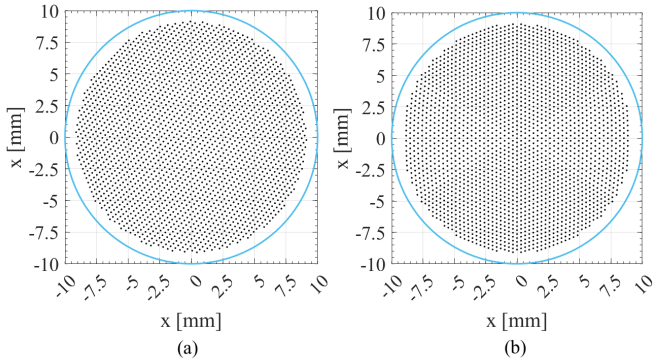

Figure 5.8: Sampling of the hyperboloid matching layers using (a) a Fibonacci distribution and (b) a regularly subdivided icosahedron distribution. The blue outline is the perimeter of the hyperboloid lens.

simulation, where the rays emanate from the hyperboloid lens phase center at $z = 0$. A collimated beam is the result. Using the same technique, the phase errors across the $\varepsilon_r = 4.6$ matching layer were analyzed. The layer has uniform thickness, and therefore does not provide the same $\lambda_m/4$ condition for all angles θ. Such errors were found to be limited to 6.1° and 9.6° at θ =30° for 140 GHz and 220 GHz, respectively.

Fig. 5.7b shows the E-field amplitudes at the lens aperture. For simplicity, the feed patterns are fitted using a simple $E_{inc}(\theta) = cos^{6.5}(\theta)$ power distribution to match the tapering of the leaky-wave feed at the specified truncation angle θ_t, see Fig. 5.4.

5.2.4. Matching Layer Design

Of key importance towards the functioning of the lens design is the mitigation of field reflections in between the high-contrast convex $\varepsilon_r = 2.3$ and concave $\varepsilon_r = 9.3$ lens interfaces. A perforated matching layer technique is chosen, as was implemented in Chapter 2. In that work, the matching layer was only 5 mm in diameter, and consisted of only 170 holes. However, when considering the much larger $D_L = 10\lambda_0 \approx 20$ mm hyperboloid lens, the sampling strategy of the lens becomes critical to prevent distortions from causing diminished matching layer performance.

To solve this problem, two distributions for the matching layer holes were considered to obtain uniformity over the hyperboloid lens surface. Both methods start by sampling an x, y, z point cloud over a sphere, after which the sphere is

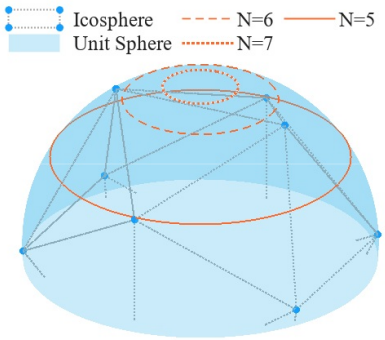

Figure 5.9: Diagram indicating the unit sphere with the underlying icosphere construction. In orange, the different icosahedron-based sampled matching layers are added.

rescaled to fit the hyperboloid surface. This rescaling is achieved by inserting the spherical x, y point coordinates into (5.6). Then, by changing the number of points in the point cloud, different periodicities can be obtained, associated to the nearest neighbor distances between the points.

The first technique samples the hyperboloid surface using a Fibonacci sampling technique with 2250 points. Its point distribution is shown in Fig. 5.8a, where the blue circle indicates the outline of the hyperboloid lens. Note that the distribution has a pole oriented towards zenith. The location of the pole was optimized for improved sampling uniformity by rotating the Fibonacci sequence by 90°.

The second technique performed the matching layer sampling using an icosahedron with N number of regular subdivisions. The same 2250 points are chosen for the distribution. As a general property, the icosahedron is constructed using 20 pentagons. Points close to these pentagons add to the distortions in the uniform sampling, and should be avoided. Therefore, the factor N needs to be sufficiently high to avoid these pentagons in the matching layer structure. This idea is visualized in Fig. 5.9, where the subset of the different sphere sizes for three values of N are shown. $N = 5$ contains the pentagons and should therefore be avoided.

Then, using a 6-nearest neighbor algorithm, the 3D Euclidean distances d between the points were calculated using the point coordinates $[x_n, y_n, z_n]$ and

$$d = \sqrt{(x_2 - x_1)^2 + (y_2 - y_1)^2 + (z_2 - z_1)^2}. \tag{5.7}$$

Some post-processing is then required. The nearest neighbor distances at the edges were removed. Furthermore, a factor $\sqrt{3}/2$ was included to compensate for the differences in 0° and 60° hexagonal grid orientations.

The resulting inter-point distances are shown in a probability histogram in Fig. 5.11, for both the Fibonacci (red) and the icosahedron (blue) distributions.

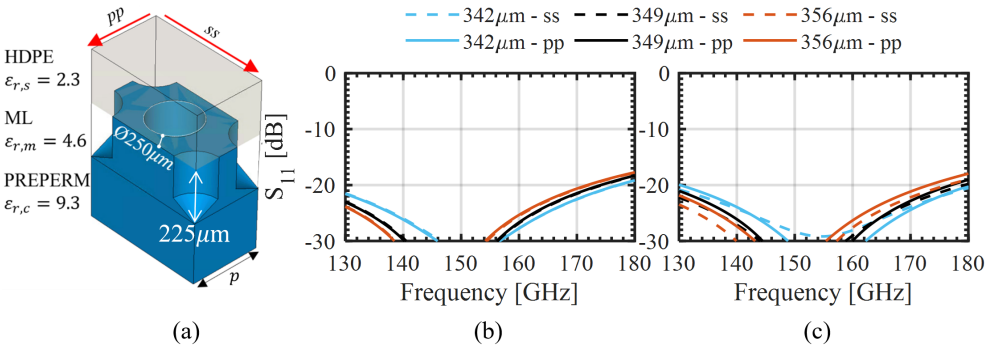

Figure 5.10: (a) Hexagon-based unit cell as used in Chapter 2. (b) Simulated S_{11} of the matching layer unit cell. The two polarizations are included with dashed and solid lines. The different colors indicate the standard deviation tolerances obtained. (c) Same simulation, but now under 30° incidence.

5

Both distribution were normalized to have the same mean periodicity of 349 µm. The standard deviation $\sigma_{\text{Fibonacci}}$ had a relatively large value of 11 µm. For the icosahedron, it was found that $N = 6$ provided the lowest standard deviation of $\sigma_{\text{ico}} = 7.2\,\mu\text{m}$. Furthermore, its point cloud distribution was also more uniformly spread over the histogram, when compared to Fibonacci distribution, as shown in Fig. 5.11. Therefore, the icosahedron-based subdivision with $N = 6$ was used.

The effect of the σ_{ico} tolerances on periodicity were studied in a unit-cell simulation. Similar to the one in [64], the unit cell shown in Fig. 5.10a uses Floquet-mode analysis to derive the S_{11} performance under plane-wave illumination. The corresponding variation in S_{11} is shown in Fig. 5.10b, indicating only minor effect on performance over frequency. Fig. 5.10c shows the same simulation setup, but now under 30° plane-wave incidence. Similar performance is obtained, as was expected from the modeling shown in Fig. 5.7, with only a slight loss in polarization symmetry. If required, the unit cells could be made more wideband by changing the geometry towards pyramidal frusta, as in [96].

5.3. Full-wave Simulations

So far, theoretical models were used to shape the lens design. However, such models do not, for instance, take into account the multiple reflections that occur inside the lens antennas. Such reflections might no longer satisfy the plane-wave based analytical models, and therefore require time-gating to improve the accuracy of the lens setup.

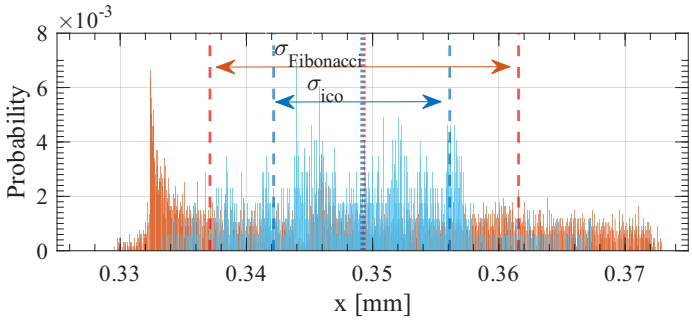

Figure 5.11: Probability histogram for the nearest-neighbor distances between the different points for the Fibonacci (red) and regular icosahedron (blue) sphere distributions. Mean and standard deviations from mean have been indicated in dotted and dashed lines, respectively.

Therefore, for a complete picture, full-wave simulations were performed by exporting the lens geometry to CST Microwave Studio. For the simulation, a homogeneous matching layer with $\varepsilon_r = 4.6$ is considered. All simulations include dielectric and ohmic losses. For aluminum, a conductivity of $\sigma = 4 \times 10^7$ Sv/m was used. The HDPE has a loss tangent of 3.3×10^{-4}, and finally the PREPERM is given a loss tangent of 5×10^{-3}.

5.3.1. Standalone Lens

First, we simulate the lens as a standalone element, radiating inside a semi-infinite $\varepsilon_r = 9.3$ medium. Open-boundary conditions were established at the outer edges to avoid reflections in the simulation box.

Fig. 5.5 includes the full-wave simulated S_{11} of the lens under the above-mentioned conditions. Because the matching layer provides a good anti-reflection layer, a similar S_{11} behavior is obtained when compared to the feeding antenna of [23]. At 140 GHz, the reflection coefficient is increased to -15 dB. Most likely this is where the $\lambda_m/4$ condition is not sufficiently met. A broader band unit-cell design of the matching layer [96] could help resolve the issue.

The normalized E-field at 180 GHz is shown in dB in Fig. 5.12. The top half represents the H-plane, whereas the bottom half is the E-plane propagation (symmetry planes were used). The planar wavefronts are clearly visible. The E-plane has slightly higher spillover loss, caused by the asymmetry in primary pattern (Fig. 5.4).

To quantify the E-field quality on the lens interface at z = 12.5 mm of Fig. 5.12, the amplitude and phase distribution is shown in Fig. 5.13. The E-field amplitude

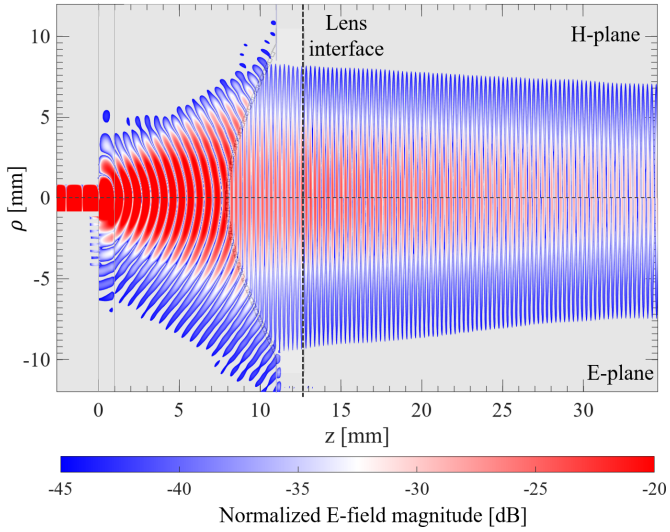

Figure 5.12: Simulated $\Re|E|$ propagating in the H-plane (top half) and E-plane (bottom half) at 180 GHz.

matches well to that of the modeled E_{out} of Fig. 5.7b, with amplitude asymmetries expected from the feed pattern. The phase remains stable within 40° from broadside within the beam waist. Such phase distortions arise from both the feed pattern and length differences over angle θ in the uniform matching layer.

As in [92], the beam quality can be evaluated over distance z using the Gaussicity $\eta_G(z)$. This metric is defined as the overlap integral between the actual E-field and an ideal fitted Gaussian beam,

$$\eta_G(z) = \frac{\left|\int E_{\text{co}}(x,y,z)\, E^*_{\text{Gauss}}(x,y,z)\, dx\, dy\right|^2}{\int |E(x,y,z)|^2\, dx\, dy \cdot \int |E_{\text{Gauss}}(x,y,z)|^2\, dx\, dy}, \tag{5.8}$$

where $E_{co}(x,y,z)$ is the co-polarized E-field under test, $E(x,y,z)$ is the total E-field (including cross-polarization) and E_{Gauss} is the fitted ideal Gaussian E-field, defined using

$$E_{\text{Gauss}}(x,y,z) = A \cdot \exp\left(-\frac{\rho^2}{w_0(z)^2}\right). \tag{5.9}$$

The fitting is obtained by minimizing the error function, defined as the amplitude difference $|E_{\text{co}}|$ and $|E_{\text{Gauss}}|$. Amplitude A is a normalization constant at $\rho = 0$. The beam waist $w_0(z)$ is fitted per distance z.

Fig. 5.14a shows the evaluated $\eta_G(z)$ as a function of distance, sampled uniformly over the WR-5 bandwidth. As expected, the outer edges of the bandwidth have

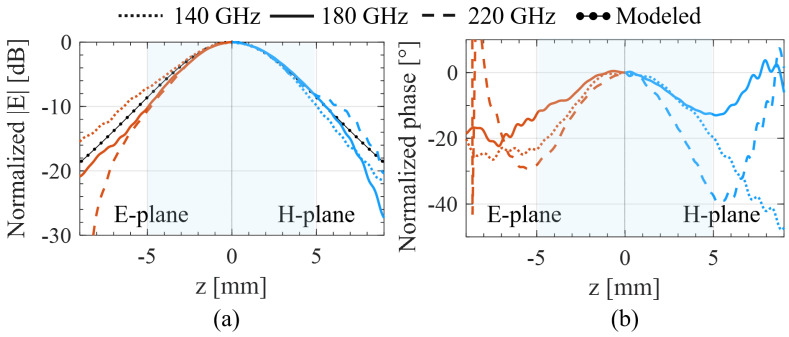

Figure 5.13: Simulated normalized E-field (a) amplitude and (b) phase distributions across the lens aperture at z = 12.5 mm of Fig. 5.12. The E-planes (left halves) and H-planes (right halves) of both figures are compared over the frequency bandwidth. In (a), the modeled amplitude distribution of Fig. 5.7b is included for comparison. The shaded blue region represents the beam-waist at 180 GHz.

worst η_G, as the phase errors from the feed and matching layer are largest at these frequencies. The frequency band from 160 to 215 GHz show $\eta_G(z) > 95\%$, with a peak value of 97.7 % at 200 GHz. As was expected from the Gaussian beam modeling of Section 5.25.2.1, the Gaussicity does not decay very rapidly over distance, implying that the use of thick MUT samples is justified without large loss of accuracy. Fig. 5.14b shows the fitted Gaussian beam waist, indicating that the field does not significantly spread over distance, in accordance to Fig. 5.2.

5.3.2. TRL Calibration Set

The final full-wave simulations are a set of Thru-Reflect-Line instances, shown in Fig. 5.15. These were simulated to extract the 2-port S-parameter boxes. For the Reflect, a Perfect Electric Conductor (PEC) plate was inserted between the Tx and Rx antennas. The Line has an added $\varepsilon_r = 9.3$, $\tan\delta = 5 \times 10^{-3}$, 90° phase shift transmission line, compared to the direct connection of the Thru.

We first look at the simulated (self) coupling of the three components, shown in Fig. 5.15b. A roughly -3 dB coupling is achieved for both Thru and Line component. Dielectric losses in the PPE950 are a significant part of this, with a total dielectric loss of 2.2 dB (1.1 dB per lens). A different material for the convex hyperboloid lenses, such as alumina, could create even higher lens-to-lens coupling. The E-field propagation through the lenses was also visualized in Fig. 5.1b.

The simulated reflection coefficients of the Thru and Line components are shown in Fig. 5.15a. Both calibration standards maintain a $<$ 10 dB S_{11}, even when

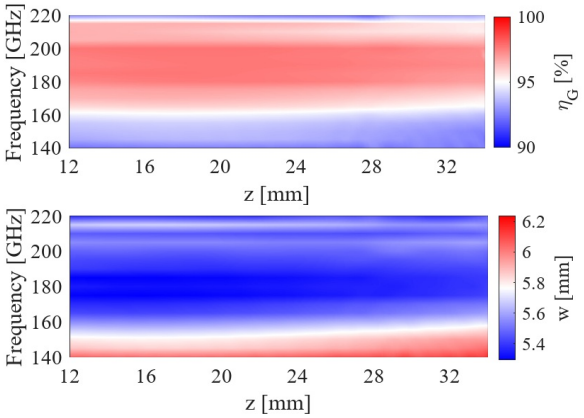

Figure 5.14: (a) Simulated Gaussian efficiency in % of the E-field propagating along the z direction, evaluated across the WR-5 band. (b) The Gaussian beam waist w, fitted to the E-field data, as a function of propagation distance z for various frequencies.

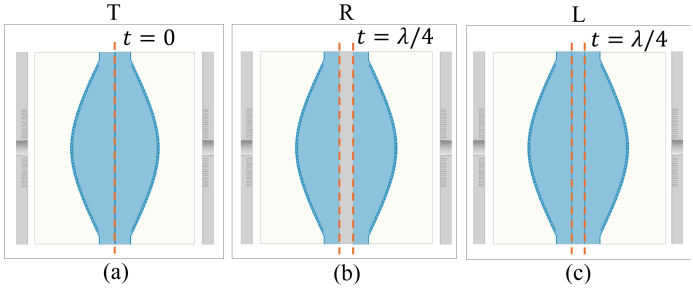

Figure 5.15: T (a) -R (b) -L (c) calibration procedure for the lens-to-lens coupled antennas. In (b), a metal plate has been added in between the reference planes, separated by distance t.

coupled directly in the near field. Compared to Fig. 5.5, some higher-order ripples can be observed. However, due to the wideband lens design, these can be filtered out using time gating techniques. This topic will be further addressed in Section 5.4.

5.4. Material Characterization Using the Lens Setup

The simulations of Section 5.35.3.2 provided a set of three 2-port S-parameters; S^{T}, S^{R}, S^{L}, for the Thru, Line, and Reflect, respectively, shown in Fig. 5.16. With these S-parameters, we can now de-embed the lens setup from an MUT, positioned

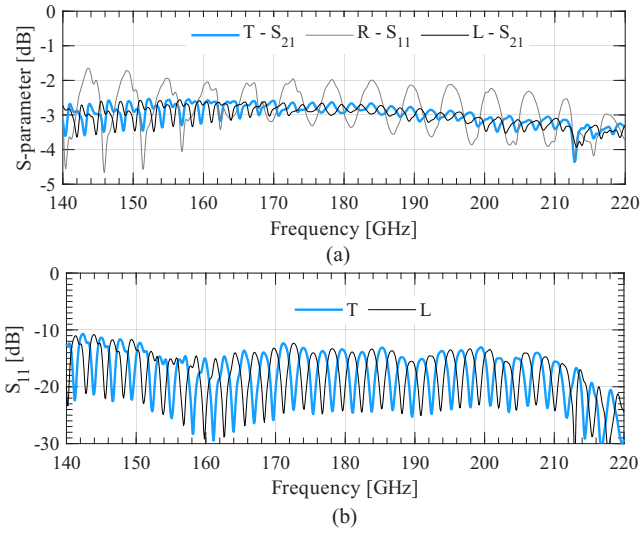

Figure 5.16: Full-wave simulated S-parameters for the TRL simulations. Losses have been included. In (a) the (self) coupling between the different TRL components. In (b), the S_{11} parameters for the Thru and Line components.

between the reference planes shown in Fig. 5.15. This de-embedding is done using the TRL algorithm explained in [97, 98]. Once de-embedded, the material characteristics can be extracted.

In this work, the relative permeability (μ_r) of all materials is assumed to be 1 (i.e. non-magnetic). We electromagnetically characterize the MUTs by their complex relative permittivity $\varepsilon_r = \varepsilon_r' - j\varepsilon_r''$, where ε_r' is the real component of the permittivity and ε_r'' is associated to the dielectric loss. Both terms allow for the calculation of the dielectric loss tangent, obtained using $\tan\delta = \varepsilon_r''/\varepsilon_r'$. We first describe the analytical model used to fit the measured S-parameters to, and then show two example cases.

5.4.1. Extraction Model for Complex Permittivity

Complex permittivity extraction is achieved by fitting the measured scattering parameters $S_{11}^{\text{meas}}, S_{21}^{\text{meas}}$ to the theoretical model of wave propagation through a dielectric slab. However, contrary to other works that involve a free-space measurement setup, the MUT is embedded in a dielectric background of relative permittivity $\varepsilon_{\text{ref}} = 9.3$. Therefore, the measured S-parameters are normalized to $Z_c = 377/\sqrt{9.3}$.

The transmission line model, similar to [82, 87], is adapted to include this dielectric background. To model $S_{11}^{\text{model}}, S_{21}^{\text{model}}$, we start by defining the reflection parameter Γ as

$$\Gamma = \frac{\sqrt{\varepsilon_r} - \sqrt{\varepsilon_{\text{ref}}}}{\sqrt{\varepsilon_r} + \sqrt{\varepsilon_{\text{ref}}}}. \tag{5.10}$$

From here, the modeled scattering parameters are a function of independent complex variable ε_r using

$$S_{11}^{\text{model}} = \frac{\Gamma(1 - e^{-2\gamma d})}{1 - \Gamma^2 e^{-2\gamma d}}, \tag{5.11}$$

where $\gamma = jk_0\sqrt{\varepsilon_{\text{ref}}}$ is the complex propagation constant in the sample material, k_0 is the wave number in free space, and d is the thickness of the MUT. Similarly, the S_{21} transmission parameter can be fit using

$$S_{21}^{\text{model}} = \frac{(1 - \Gamma^2)e^{-\gamma d}}{1 - \Gamma^2 e^{-2\gamma d}}. \tag{5.12}$$

5

Next, the fitting of measurements and model is performed on phase and amplitude separately, of both the S_{11} and S_{21}. To avoid large phase errors when the amplitude of either of the two are small, weighting factors w_Γ and w_T are included for the S_{11} and S_{21}, respectively. Given the measured S-parameters $S_{11}^{\text{meas}}(f)$, $S_{21}^{\text{meas}}(f)$, the complex permittivity ε_r is obtained by minimizing the objective function

$$\min_{\varepsilon_r} \begin{bmatrix} w_\Gamma(\varepsilon_r)^2 \left(\angle S_{11}^{\text{model}}(\varepsilon_r) - \angle S_{11}^{\text{meas}}\right) \\ w_\Gamma(\varepsilon_r)^2 \left(\left|S_{11}^{\text{model}}(\varepsilon_r)\right| - |S_{11}^{\text{meas}}|\right) \\ w_T(\varepsilon_r)^2 \left(\angle S_{21}^{\text{model}}(\varepsilon_r) - \angle S_{21}^{\text{meas}}\right) \\ w_T(\varepsilon_r)^2 \left(\left|S_{21}^{\text{model}}(\varepsilon_r)\right| - |S_{21}^{\text{meas}}|\right) \end{bmatrix}, \tag{5.13}$$

where the weights are defined by $w_\Gamma = |S_{11}^{\text{model}}| \cdot |S_{11}^{\text{meas}}|$ and $w_T = |S_{21}^{\text{model}}| \cdot |S_{21}^{\text{meas}}|$. The function is minimized for each frequency point, using an iterative least-squares technique.

5.4.2. Case I: Vacuum

The first case investigates material characterization where the MUT is a 2.7 mm thick slab of vacuum. The TRL of section 5.35.3.2 is applied to the simulated S-parameters, resulting in S^{sim}. By doing so, the reference planes are shifted to the MUT boundaries.

Fig. 5.17a shows the resulting S_{11}^{sim} and S_{21}^{sim} parameters in time-domain. Beyond 0.3 ns, multiple reflections with an amplitude of at most -29 dB are visible. However, due to the large frequency bandwidth (80 GHz) of the antenna, such reflections can

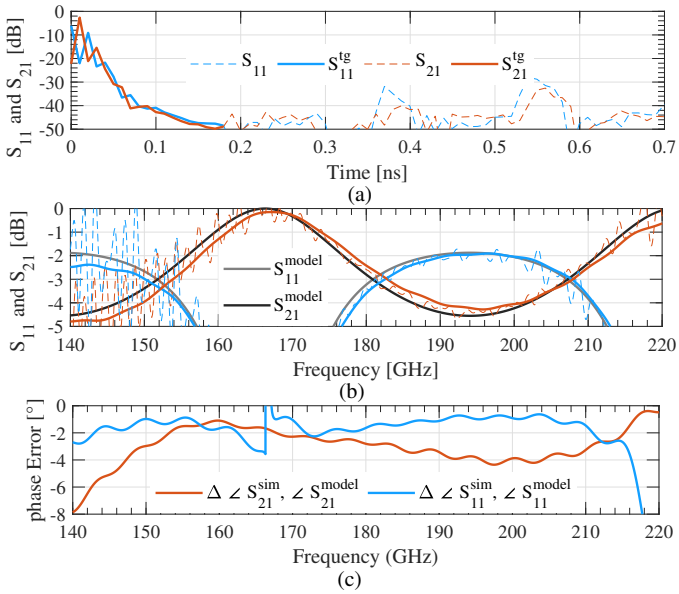

Figure 5.17: Simulated S-parameters of the case with vacuum in between the reference planes. (a) The time-response of S_{11} and S_{21}. The time-gated values are extracted from 0 ns to 0.18 ns. (b) The resulting time-gated frequency domain S-parameters, compared to the transmission-line model. (c) resulting phase errors between the model and the simulated S-parameters.

be time-gated out, as indicated in Fig. 5.17a. The time gate is applied from 0 ns to 0.18 ns. This time-gating affects the frequency-domain S-parameters, shown in Fig. 5.17b, by eliminating the ripples caused by the multiple reflections. The resulting $S_{11}^{\text{sim,tg}}$ and $S_{21}^{\text{sim,tg}}$ can then be compared to the S_{11}^{model} and S_{21}^{model} of (5.11) and (5.12), respectively.

As presented in (5.13), this comparison for the objective function is performed in both amplitude and phase, and therefore, Fig. 5.17c shows the simulated phase differences between $S^{\text{sim,tg}}$ and S^{model}. As shown, the phase errors are limited to around $-4°$ within the 150 to 210 GHz band. Outside this band the error is larger, possibly caused by the decay in Gaussicity (Fig. 5.14), the increased S_{11}, or the ringing effects of the time-gating at the edges of the frequency bandwidth. Finally, as visible in Fig. 5.17c, the phase of the $S_{11}^{\text{sim,tg}}$ shows erratic behavior when $|S_{11}^{\text{sim,tg}}|$ is going to zero at $\lambda_0/4$ multiples of material thickness. For this reason, the weight factor has been introduced in (5.13) to suppress erroneous fitting.

The post-processed $S^{\text{sim,tg}}$ can then be used to extract the material parameters. Fig. 5.18a,c shows the resulting permittivity (top) and loss tangent (bottom) for the analyzed vacuum material. For the permittivity, a roughly 1% error is made.

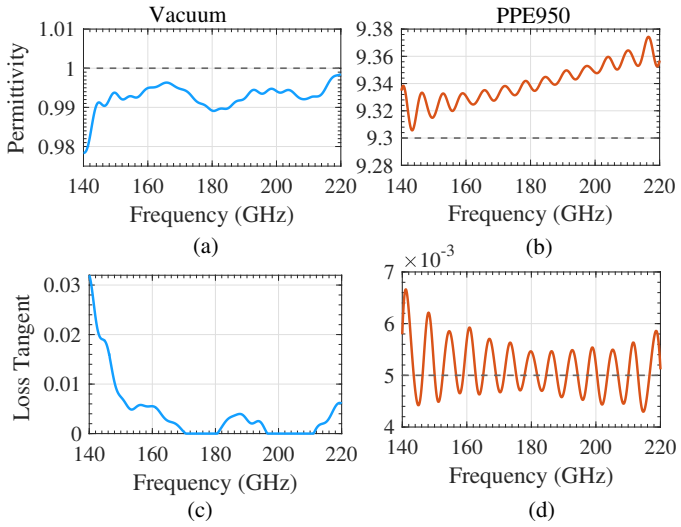

Figure 5.18: Simulated extracted material characteristics in terms of permittivity (a, b) and loss tangent (c, d). Two MUTs were characterized: vacuum (a, c) and PPE950 (b, d). Dashed horizontal lines indicate the true simulated values.

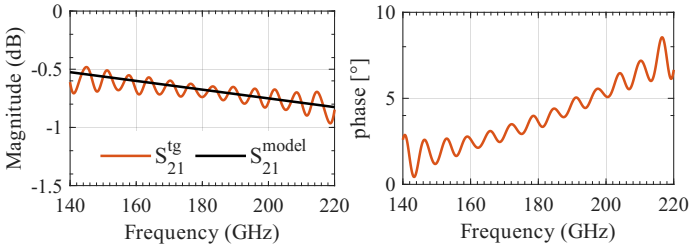

Figure 5.19: Simulated S-parameters of the slab of PPE950 material, calibrated and time-gated until its reference planes. (a) The time-gated frequency domain S-parameters, compared to the transmission-line model. (b) resulting phase errors between the model and the simulated S-parameters.

The loss tangent is more difficult for low loss and electrically thin materials, and therefore suffers from larger errors.

5.4.3. Case II: Reflectionless Slab

The second case involves the characterization of a layer of 2.7 mm thick PPE950, with true permittivity of 9.3 and loss tangent of 5×10^{-3}. The exact same TRL and post-processing (including time-gating) procedure as in Section 5.45.4.2 is performed. The calibrated S_{21} is shown in Fig. 5.19a, and compared to the model, showing good agreement, apart from some remaining oscillations. Fig. 5.19b shows the phase deviation, indicating a drifting phase error of up to 10°. The calibrated S_{11} is below -50 dB due to the reflection-less interface. This verifies that the TRL has worked well, since the S_{11} from the antenna setup has been succesfully de-embedded. For this reason, the transmission line model relies purely on the S_{21} for characterizing the material, since the weight w_Γ will be approximately zero.

Fig. 5.18b and d show the extracted material parameters. The permittivity is retrieved within a 0.8% error, and is slowly drifting due to the drifting phase error. . The loss tangent oscillates around 5.1×10^{-3} with a standard deviation of 1.4×10^{-3} (2% mean error).

5.5. Conclusion

This work proposed a new lens architecture for high-frequency material characterization purposes, using the direct generation of high-purity plane waves. The plane wave propagates in a dense dielectric material, thereby significantly suppressing the field spreading effects, when compared to standard free-space setups. The lens structure offers a flat interface, that offers great benefits when considering material measurements, as samples can be clamped between the lens interfaces.

Using a full-wave simulation approach, direct plane-wave generation was found to have a Gaussicity of $>$ 94 % was achieved from 160 GHz to 215 GHz. A high port-to-port coupling of up to -3 dB was achieved. The wideband antenna properties allow the usage of time-gating techniques to mitigate the impact of multiple reflections.

Using a TRL calibration technique, the reference planes can be shifted to the interfaces of the material under test. From there, the material complex permittivity can be extracted using a transmission line technique. This was exemplified in two case studies, where the resulting errors were limited to 2% in permittivity and 2% in mean loss tangent.

The lens design could also enable applications in other fields, such as near-field telecommunications. The promising design and numerical validation of the proposed concepts opens the path for prototyping of this idea and performing experimental measurement of different samples.

Future improvements include increasing further the Gaussicity by improving the lens design to better fit the feeding antenna phase distribution.

III

Spherical Fly-Eye System Design, Optimization & Integration

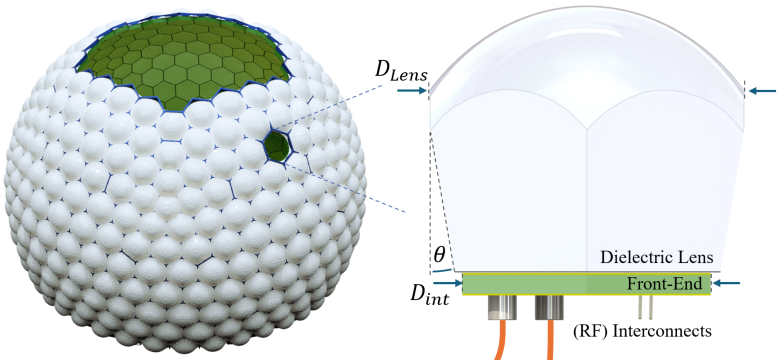

Figure 5.20: Schematic overview of the proposed spherically conformal Fly-Eye Array made of high-gain lens antennas. A cross-sectional conceptual view of a single element is shown on the right, visualizing the antenna front-end with its dielectric lens.

CONTINUOUS progress in > 100 GHz RFIC technologies has enabled the development of fully integrated, compact footprint, high-gain antenna systems with narrow radiation patterns. At such frequencies, new antenna systems are envisioned, combining both communications and sensing, where the need for thousands of simultaneous multi-beams are required [35]. The first two parts of this thesis were dedicated towards the development and measurement of such antennas. However, as was discussed in Chapter 1, challenges remain in the development of high-gain antenna systems possessing (near) hemispherical coverage. These challenges will be tackled in this upcoming part.

Chapter 1's introduction, in unison with Appendix A, demonstrated that the phased-array SNR was equivalent to that of a Fly's-Eye array, given the same number of elements. The latter offered an overall less complex design, as the implementation problems due to the required $\lambda/2$ inter-element spacing are not present; A Fly's-Eye system does not suffer from the $10\log(\cos(\theta))$ drop in power at large angles θ, avoids thermal problems, and provides access to simultaneous multi-beam capability without active electronic scanning. As each lens antenna element functions independently, the topology is scaled more easily to a simultaneous multi-beam system.

A conceptual view of the Fly-Eye system is shown in Fig. 5.20. The array consists of the lens antenna elements of Chapters 2 and 3, and leverages the obtained degrees-of-freedom of its design. This spherical array follows a so-called Goldberg polyhedral, that will be described and optimized in Chapter 6. The cross-sectional view of Fig. 5.20 illustrates the AiP front-end below the dielectric lens footprint. To enable this AiP integration, Chapter 7 ventures into the high-frequency characterization of the flip-chip interconnects. Finally, Chapter 8 presents the first steps towards the development of a fully integrated spherical Fly Eye system at D-band.

Chapter 6

Optimization of Spherically Conformal Antenna Arrays Using Goldberg Polyhedra

This chapter introduces a method for the optimization of spherically conformal antenna arrays using Goldberg polyhedron topologies. The method allows for the optimization of antenna systems consisting of potentially hundreds of elements. The antenna system is optimized for directivity, beam overlap and interference using cost functions based on analytically computed antenna radiation patterns. The method runs relatively fast, enabling scalability towards an even larger number of elements. Two antenna system design cases were then introduced. The first achieves a -3dB uniform beam overlap for full hemispherical coverage. The second includes interference analysis for a full multi-beam communication channel. The methodology can be further extended to a variety of mathematically-defined omnidirectional antenna systems.

6.1. Introduction

NUMEROUS applications require (near) omnidirectional or hemispherical coverage. Examples include the tracking of satellites, military/civilian radars and biomedical sensing [99]. In particular, the next generation of communication networks envisions antennas with multiple beams, such as MIMO arrays [100, 101], millimeter-wave phased arrays [102] and lens systems [35, 103]. Such antenna arrays have multiple degrees of freedom [104, 105] that can increase significantly the coverage in complex scenarios [106].

Unfortunately, the design of high-gain antenna systems that possess omnidirectional capability is not a trivial task. One of the main challenges is to achieve an even angular coverage when different beams cross-over, referred to as beam overlaps. As the antenna gain increases and beam widths become more narrow, an increasingly larger amount of antenna elements are necessary to fulfill minimum beam overlap requirements. Crucially, a low beam overlap could result in a decreased link budget or reduced radar range. For these reasons, the Fly's Eye antenna system envisions >1000 elements to provide near-omnidirectional angular coverage with highly directive beams [35].

While hemispherical coverage is also achievable using conical or elliptical arrays [107], a spherically conformal array layout is chosen, as the spherical surface is normal to any given hemispherical direction and could therefore provide a uniform radiation pattern in all directions without active scanning. In such a scenario, the distribution of the antennas over the sphere becomes as important as the performance of the antenna elements itself. The positioning of all antenna elements, their orientation and their radiation patterns must be optimized in order to achieve uniform coverage meeting the link requirements in all directions. Furthermore, for communication links, Co-Channel Interference ratio (C/I) could become another bottleneck for system performance if not properly addressed. Combining all these degrees of freedom, spherically conformal array optimization presents a computationally intensive task that becomes increasingly problematic as more antenna elements are required.

In literature, numerous spherically or cylindrically conformal arrays can be found at lower frequencies [108–110]. However, such works are limited in the number of elements to at most 52. In [111], a comparative study of spherically conformal antenna element layouts was performed, including a quasi-uniform design based on the truncated icosahedron. Such icosahedron-based design features a 60-fold symmetry, that offers significant fabrication benefits because it greatly reduces the number of unique antenna elements. The icosahedral design of [111] was, however, found to be less uniform than a comparative spherical spiral design, and no further design guidelines for an increased number of elements was provided. Other approaches, as in [108], use a sphere meshing method that approaches uniformity. But such technique does not take into account antenna radiation patterns, and does not make use of available symmetries found in an icosahedral approach.

In this work, the same icosahedron-based array architecture is used as in [111]. However, it is extended towards a Goldberg polyhedra topology, that provides some unique features. Using recent research in [112], the spherical array can now be further optimized for a myriad of mathematically-defined cost functions. This way, important antenna performance metrics, such as radiation uniformity, maximum directivity and channel interference can now be modeled and optimized.

This work is structured as follows. First, Section 6.2 introduces the Goldberg architecture and optimization methodology in more detail. Then, Section 6.3 intro-

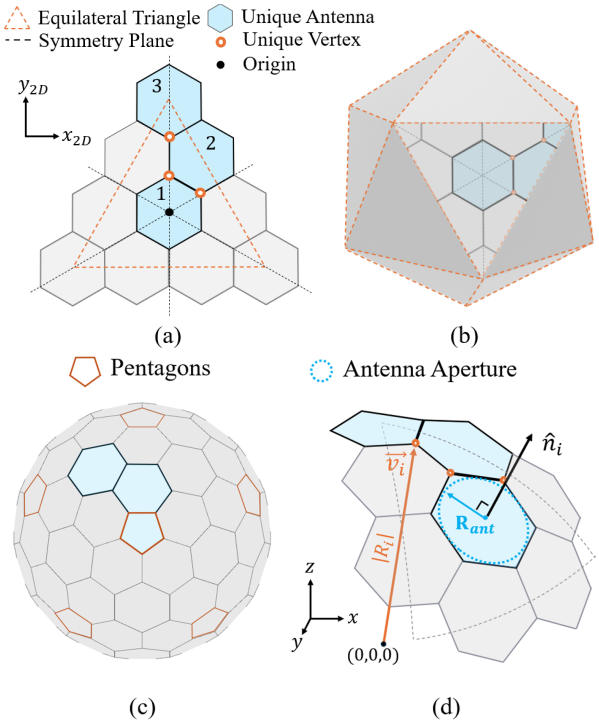

Figure 6.1: (a) Planar graph for the GP(3,0) topology. Such topology consists of three unique antennas (blue) and 3 unique vertices (dots). (b) The icosahedron into which the equilateral triangle of (a) is mapped. (c) The resulting GP(3,0) Goldberg polyhedron. (d) The reference geometry to define the antenna parameters.

duces the mathematically defined cost functions used for optimizing the spherical array. The array behavior and array initial guess are modeled in Section 6.4. Results are summarized in Section 6.5, followed by two design examples in Section 6.6.

6.2. Goldberg Antenna Array Architecture Optimization

6.2.1. General Methodology

The optimization methodology employed in this work relies upon the framework introduced in [112]. First, the Goldberg sphere is parameterized through the use of

independent variables that fully describe the geometry. Then, a set of user-defined cost functions is mathematically defined, that depend on these independent variables. Finally, these cost functions can be iteratively minimized to optimize the polyhedron geometry.

The parameterization of the geometry is fundamental for the method to work efficiency. A more comprehensive explanation can be found in [112], but the described process can be briefly summarized as follows:

First, a planar graph is generated according to the Goldberg construction method [113], characterized by a specific Goldberg topology denoted as GP(n, m), where n and m determine the number of hexagons in the polyhedron. Fig. 6.1a shows an example planar graph for GP(3,0). A regular hexagonal grid is formed, with vertices described by $x_{2\mathrm{D}}$ and $y_{2\mathrm{D}}$ coordinates. These graphs form equilateral triangles, which are subsequently mapped onto the faces of an icosahedron (Fig. 6.1b). Then, the triangular edges of the icosahedron are connected. Finally, all vertices are projected onto the surface of the Goldberg sphere, shown in Fig. 6.1c. After these mathematical mappings, the vertices now have 3D coordinates $\vec{v_i} = [x_\mathrm{i}, y_\mathrm{i}, z_\mathrm{i}]$, as indicated in Fig. 6.1d. Together they form the Goldberg polyhedron, shown in Fig. 6.1c.

For such polyhedra, it is essential to distinguish between the Goldberg topology and the Goldberg geometry. The topology defines the combinatorial structure of the polyhedron, including the number of unique vertices and faces (e.g. antenna elements). Fig. 6.2 shows three different topologies with increasing values of m. The number of faces in the Goldberg polyhedron is given by $9(m^2 + mn + n^2) + 12$, where 12 is the fixed number of regular pentagons in the topology. By contrast, the geometry specifies the spatial arrangement and dimensions of these faces. In this work, we restrict to the usage of a particular topology class called 'type I' with $n = 0$, that allows some additional constraints in the planar graph for improved computational efficiency. However, the method works equally well for the other topologies, as demonstrated in [112].

It takes 5 vertices to form each of the 12 pentagons, and 6 for the hexagons. The hexagonal and pentagonal faces form the apertures of the antennas. Due to the three-fold symmetry of the equilateral triangles and the 20-fold symmetry of the icosahedron, the resulting structure exhibits 60-fold rotational symmetry. Such symmetries greatly reduce the number of vertices and antennas required to optimize the antenna spheres. These are known as the unique vertices and unique antennas, respectively. For example, while a GP(6,0) configuration contains 336 faces in total, it is reduced only 7 unique antennas types and 9 unique vertices. This is shown in the planar graph in Fig. 6.1a, and in the 3D polyhedron in Fig. 6.1d. The total number of unique vertices is denoted as N_v, and the total number of unique faces (e.g., antennas) is denoted as N_a.

To be consistent with [112], the same independent variable definition is used: Each unique vertex v_i is parameterized by the coordinates of the planar graph (Fig.

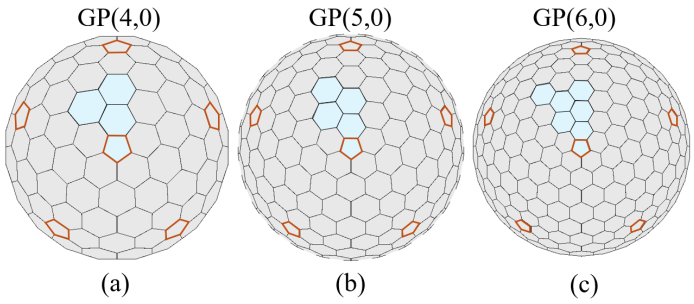

Figure 6.2: Different topologies for the Goldberg polyhedra. Unique antennas are indicated in blue. The pentagons are outlined in red for clarity.

6.1a) $(x_\mathrm{i}^{2\mathrm{D}}, y_\mathrm{i}^{2\mathrm{D}})$. Finally, since the vertices are not necessarily located on the surface of a sphere, an independent variable for the vertex radius is used, defined as $R_\mathrm{i} = \sqrt{x_\mathrm{i}^2 + y_\mathrm{i}^2 + z_\mathrm{i}^2}$ (indicated in Fig. 6.1d). These independent variables for each vertex fully parameterize the geometry, using the same mapping functions provided in [112].

Based on this parameterization, a range of cost functions can be formulated. As in [112], the optimization objective is defined as,

$$\min F = \sum_{p=1}^{q} w_p f_p^2(\mathbf{x}^{2\mathrm{D}}, \mathbf{y}^{2\mathrm{D}}, \mathbf{R}), \tag{6.1}$$

where F is the minimization objective, $\mathbf{x}^{2\mathrm{D}}$, and $\mathbf{y}^{2\mathrm{D}}$ are the lists containing all $x_\mathrm{i}^{2\mathrm{D}}$ and $y_\mathrm{i}^{2\mathrm{D}}$ vertices, respectively. $\mathbf{R}$ is the list containing all vertex radii R_i. ω_p is the weight associated to the particular cost function $f_p(x, y, R_v)$, described entirely by the parameterized Goldberg geometry.

6.2.2. Antenna Optimization Framework

With the antenna optimization objective in mind, this work extends the framework provided by [112] to antenna system applications by introducing far-field-based cost functions. These include criteria related to antenna directivity, beam crossover points, and co-channel interference. Such cost functions enable the optimization of the array layout to meet application system performance targets, such as the radar range equation or the Friis' transmission equation.

Fig. 6.1d shows schematically the 3D layout of the unique antennas for an example GP(3,0) topology. The geometry has unique vertices $\vec{v}_1 \dots \vec{v}_{N_v}$, whereas the other vertices follow from symmetry planes. Each unique hexagonal antenna element is constituted by 6 of these vertices. Since the hexagonal elements are not necessarily

regular, an algorithm is used that calculates the maximum inscribed circle within the 6 vertices (assuming a convex hull), described in [114]. The function returns the element radii $R_{\mathrm{ant},1} \dots R_{\mathrm{ant},\mathrm{N_a}}$, representing the unique antenna apertures. Since the pentagon is always regular due to icosahedral symmetries, its apothem or inner circle radius follows from

$$R_{\mathrm{ant}}^{\mathrm{pent}} = \frac{C_{\mathrm{pent}}}{2\sqrt{5-\sqrt{20}}}, \tag{6.2}$$

where C_{pent} is the chord length of the regular pentagon.

Each antenna element is oriented along a direction vector $\vec{n}_{\mathrm{i}}$ (see Fig. 6.1d), that is not necessarily collinear with respect to the mean of its constituent vertices. The normals form a set $\vec{n}_1 \dots \vec{n}_{\mathrm{N_a}}$. One additional complexity is that the hexagonal faces are not necessarily flat during the optimization process [112]. Therefore, a well-established definition of the antenna direction vectors is required to avoid errors for non-planar hexagonal faces. To calculate the face normals, the average cross products at all six edges are calculated using

$$\vec{n}_j = (\vec{v}_k - \vec{v}_j) \times (\vec{v}_k - \vec{v}_j), \quad \text{for } j = 1, \dots, 6, \tag{6.3}$$

where $k = (j-1) \bmod 6$ and $l = (j+1) \bmod 6$. Finally, the (mean) antenna direction vectors are calculated by:

$$\vec{n}_{\mathrm{i}} = \frac{1}{6} \sum_{i=1}^{6} \vec{n_j}. \tag{6.4}$$

For the unique pentagon, the normal is always along the z-axis direction.

Once the antenna direction vectors are obtained, the antenna cost functions can be defined. These are based on the far-field radiation patterns. These patterns are numerically approximated using

$$\mathrm{FF}(k_r) = C \int_0^{R_{\mathrm{ant}}} \exp\left(-\left(\frac{\rho}{w_0}\right)^2\right) J_0(k_r \rho)\, \rho \, d\rho, \tag{6.5}$$

where k_r is the radial spatial frequency, given by $k_r = k_0 \sin(\theta)$. Angle θ is the angular difference between the observation angle and the element normal vector $\vec{n}_{\mathrm{i}}$. J_0 is zeroth-order Bessel function of the first kind. ρ is the radial coordinate that is distributed linearly over the antenna element radius R_{ant}. Parameter w_0 introduces an amplitude tapering in the element aperture, as will be explained later. Finally, the constant C is added to normalize the pattern to its maximum at $\theta = 0°$. The patterns are calculated in 1D, assuming rotationally symmetric patterns. Finally, the antenna element directivities $D_1 \dots D_{N_a}$ are derived from these patterns. Depending on the desired application, the far-field distribution of (6.5) can be easily replaced

with a more accurate one, or even extended to rotationally asymmetric patterns. The effect of electromagnetic polarization could also be added here.

Using w_0, control of the far-field side lobe level (SLL) is enabled. This is critical when optimizing the array interference levels, as will be discussed in Section 6.3.4. For evaluating the interference, the spherical array is subdivided into a frequency reuse scheme with reuse factor N_f. This topic will be addressed in Section 6.3.4.

The next section describes in more detail how the cost functions for optimizing the directivity, beam overlaps and the interference are introduced.

6.3. Cost Function Definitions

6.3.1. Face Planarity

The first cost function is taken directly from [112], and calculates a cost function based on the planarity of the hexagonal faces. This planarity provides additional practicality to the implementation of the spherically conformal arrays.

It works as follows; Each hexagonal face is assigned to six vertices $v_i^1 \dots v_i^6$, ordered randomly. Vertices $v_i^1 \dots v_i^3$ are selected to form a plane P. Then, the three cost function for planarity are defined as

$$f(\mathbf{x}^{2\mathrm{D}}, \mathbf{y}^{2\mathrm{D}}, \mathbf{R}) = d_i = 0, \quad \text{for } i = 1, \dots, 3, \tag{6.6}$$

where d_i is the distance from vector v_{i+3} to P. The pentagonal faces are always flat.

From here on, the work defines the cost function based on the antenna far-field performance.

6.3.2. Directivity

The second cost function that will be discussed is the antenna directivity. Controlling the maximum directivity can be important for instance when the maximum Effective Isotropic Radiated Power (EIRP) needs to be fixed. It is also useful in controlling the dimensioning of the spherical array, as the maximum directivity depends on the size of the element aperture.

The following cost function for the antenna directivities was used,

$$f(\mathbf{x}^{2\mathrm{D}}, \mathbf{y}^{2\mathrm{D}}, \mathbf{R}) = \sum_{i}^{Na} \left| \mathrm{D}_{\mathrm{i}}^{\mathrm{dB}} - \mathrm{Dir}_{\mathrm{set}}^{\mathrm{dB}} \right|^2, \tag{6.7}$$

where $\mathrm{Dir}_{\mathrm{set}}^{\mathrm{dB}}$ is the user-defined desired directivity.

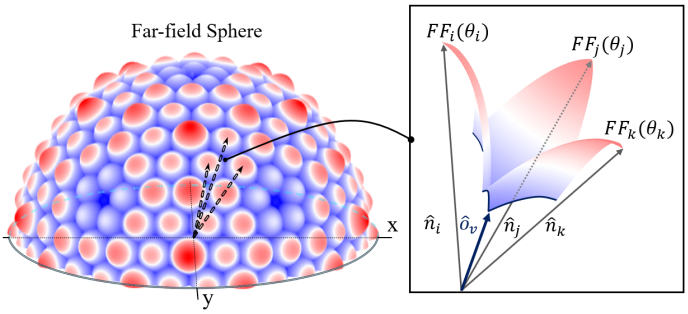

Figure 6.3: Example far-field directivity distribution of a GP(6,0) sphere. The inset shows a representation of finding the beam overlap direction $\hat{o}_v$, based on the three adjacent far-field patterns with normals $\hat{n}_{i,j,k}$

6.3.3. Beam Overlap Points

Control of the array radiation pattern uniformity is crucial for meeting the system requirements. Typically, a beam crossover of -3dB for two adjacent beams is used [115]. However, for a hexagonal grid, the lowest directivity is found at the overlap points of three adjacent beams. Fig. 6.3 shows an example far-field radiation distribution. Since all antenna triplets share a single beam overlap point, there are N_v number of overlap points to be found. The cost function for the overlap points is defined by

$$f(\mathbf{x}^{2\mathrm{D}}, \mathbf{y}^{2\mathrm{D}}, \mathbf{R}) = \sum_{i}^{N_v} \left| \mathrm{D}_{\mathrm{o},i}^{\mathrm{dB}} - \mathrm{D}_{\mathrm{o,set}}^{\mathrm{dB}} \right|^2 \tag{6.8}$$

Alternatively, when also optimizing for D_{set} (Section 6.3.2), the cost function is defined by taking the variance of the overlap points. In this case, $\mathrm{D}_{\mathrm{o,set}}^{\mathrm{dB}}$ is the mean of all $\mathrm{D}_{\mathrm{o},i}^{\mathrm{dB}}$.

To find these beam overlaps, first the three antennas closest to the overlap point are found using an adjacency list. The inset of Fig. 6.3 shows schematically the example geometry of three neighboring beams, each with direction vector $\hat{n}_{\mathrm{i,j,k}}$. The overlap points are then numerically found using an iterative solving technique. As shown in Fig. 6.3, we denote their positions by $\vec{o_v}$, and their corresponding directivity values by $D_{o,i}$. As an initial guess for the iterative solver, the mean direction of $\hat{n}_{\mathrm{i,j,k}}$ is used as $\vec{o}_0 = \frac{1}{3}\left(\hat{n}_\mathrm{i} + \hat{n}_\mathrm{j} + \hat{n}_\mathrm{k}\right)$. Then, the angular distances between the normal vectors and the solver input is found by using the dot product:

$$\theta_{i,j,k} = \arccos\left(\hat{n}_{i,j,k} \cdot \hat{o}\right). \tag{6.9}$$

For each of the three antennas, the radiation patterns are found using (6.5). The k_r input expression can be simplified further using the trigonometric identity

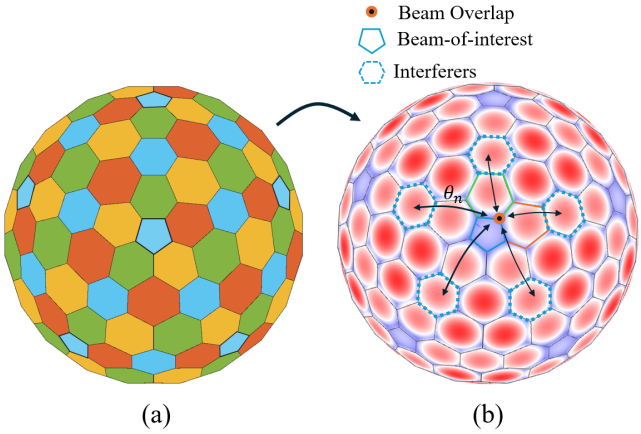

Figure 6.4: (a) Example frequency reuse scheme for a GP(4,0) Goldberg polyhedron. The different frequencies bands assigned to each antenna elements. (b) Far-field radiation sphere of (a). An example is shown for the five nearest interferers for the selected beam overlap point of one of three channels.

$\sin(\arccos(x)) = \sqrt{1-x^2}$, valid for $x \in [-1, 1]$. The input becomes $k_r = k_0\sqrt{1-(\hat{n}_{i,j,k} \cdot \hat{o})^2}$. The resulting far-field expression will be denoted by $FF_{i,j,k}$. This allows us to define the cost function to find the overlap points. The overlap is found when all three antennas have equal far-field directivity, e.g.

$$\begin{bmatrix} \mathrm{D}_{o,i}^{\mathrm{dB}} - \mathrm{D}_{o,j}^{\mathrm{dB}} \\ \mathrm{D}_{o,j}^{\mathrm{dB}} - \mathrm{D}_{o,k}^{\mathrm{dB}} \\ \mathrm{D}_{o,k}^{\mathrm{dB}} - \mathrm{D}_{o,i}^{\mathrm{dB}} \end{bmatrix} = 0 \tag{6.10}$$

Note that this cost function is to derive the overlap points only, and is not associated to the objective function in (6.1). The cost function $\vec{f}(\vec{o})$ is then iteratively optimized. The solution vector $\vec{o}_v$ then indicates the location of the overlap point and is stored for further processing. The corresponding overlap point directivity $D_{o,v}$ is then found by

$$D_{o,v} = D_i \left| FF\left(k_0\sqrt{1-(\hat{n}_i \cdot \hat{o_v})^2}\right)\right|^2, \tag{6.11}$$

where D_i is the directivity associated to the i^{th} antenna.

6.3.4. Interference

For telecommunication systems, mitigating interference is crucial for establishing reliable communication links. Also known as the Signal-to-Interference-plus-Noise Ratio

(SNIR), a balancing between the interference and signal strength is required. For the interference, the analysis performed in this work is based on the co-channel interference, or C/I. The co-channels are the channels that share the same frequency reuse index $f_1, \ldots, f_{N_f}$. An example $N_f = 4$ frequency reuse scheme for Goldberg polyhedra is visualized in Fig. 6.4a. As described in [115], a trade-off occurs between maximizing the antenna directivity coverage and maximizing C/I. A typical value for satellite application is a $\mathrm{C/I^{dB}}$ of 13 dB [115].

For the objective function in this work, the interference cost function is defined as

$$f(\mathbf{x}^{\mathrm{2D}}, \mathbf{y}^{\mathrm{2D}}, \mathbf{R}) = \begin{cases} 0, & \mathrm{C/I^{dB}} \geq \mathrm{C/I^{dB}_{set}} \\ \Sigma_i^{\mathrm{Nv}} \left| \mathrm{C/I^{dB}} - \mathrm{C/I^{dB}_{set}} \right|^2, & \mathrm{C/I^{dB}} < \mathrm{C/I^{dB}_{set}} \end{cases} \tag{6.12}$$

where $\mathrm{C/I_{set}}$ represents the user-defined threshold value for the interference, above which no cost is associated.

To calculate C/I, the directivity of the desired channel is divided by the sum-of-interferers. However, doing so over the full 3D radiation patterns would be computationally too expensive. Therefore, to optimize for the interference, a more efficient cost function is required. In [115], it was found that the worst-case interference (using Gaussian beam analysis) occurs at the beam crossover points $\vec{o}_v$. Fortunately, the location and directivity values $D_{o,v}$ of these crossover points has already been established in Section 6.3.3. Therefore, all that remains to obtain the C/I is to sum the contributions of all interfering co-channels at the unique overlap points.

The idea is visualized in Fig. 6.4. The $N_f = 4$ frequency reuse scheme is applied to an example GP(4,0) antenna sphere. The resulting far-field radiation patterns of the sphere are shown in Fig. 6.4b. The figure focuses on one out of N_v overlap point. Each overlap point has three adjacent channels, while each channel has its own set of interferers that collapse onto the overlap point. Therefore, this operation is repeated $3N_{\mathrm{v}}$ times.

The following procedure is followed to calculate the C/I. First, using mirroring and rotation operations, the unique antenna normals $\vec{n}_a$ with their associated frequency reuse index f_a are replicated over the whole antenna sphere for $a = 1, \ldots, N_{\mathrm{a}}$ (see Fig. 6.4a). Iteratively, there is one beam of interest, and the rest is considered as interfering. Then, for each unique overlap point $\vec{o}_v$, the three adjacent frequency channels with index $f^{i,j,k}$ are retrieved using an adjacency list. Then, the angles between the overlap points and all co-channel normals are found:

$$\theta_n^{i,j,k} = \angle(\vec{o}_v, \vec{n}_a^{i,j,k}) \mid n = 1, \ldots, N_c^{i,j,k}, \tag{6.13}$$

where $N_c^{i,j,k}$ is the total number of co-channels in frequency reuse index i, j, k. The resulting array of angles is then sorted in ascending order, resulting in $\theta_{\mathrm{n,sort}}^{i,j,k}$. In the sorted array, the first value will be the beam of interest, since it is located closest

to the overlap point. The others are interferers. In general, the largest contributors to total interference are the three closest co-channels [115]. For completeness, the angles with indices 2-13 are selected, and summed for their total interference:

$$I^{i,j,k} = \sum_{n=2}^{13} D_n^{i,j,k} \left| FF\left(k_0 \sin(\theta_{\mathrm{n,sort}}^{i,j,k})\right)\right|^2, \tag{6.14}$$

where $D_n^{i,j,k}$ is the maximum directivity associated to the n^{th} antenna of channels i, j, k. Finally, the C/I ratio at vertex v for frequency reuse subset i, j, k, is obtained by calculating

$$C/I_v^{i,j,k} = \min\left[10\log_{10}\left(D_{o,v}/I^{i,j,k}\right)\right]. \tag{6.15}$$

For the spherical Goldberg array the minimum reuse index is 4, due to the addition of pentagons inside the hexagonal grid, as shown in Fig. 6.4a. In most locations, the frequency reuse distances match the $N_f = 4$ case. However, close to the pentagons, reuse distances that approximate an $N_f = 3$ are unavoidable. Nevertheless, using sufficiently large element angular separation and controlling the SLL, decent C/I is attainable, as will be shown in Section 6.6.2.

6.4. Initial Guess Calculation

The previous sections derived the cost functions for the optimization tool. However, in order to efficiently optimize the geometry and limit convergence into local minima, good initial guesses are required for the parameter set (x_v, y_v, R_v). Like in [112], the initial guesses for the x_v and y_v coordinates are simply provided by the hexagonal grid of the planar cage, see Fig. 6.1. However, more effort is required for vertex radii R_{i}.

Their initial guess is based on estimating the element diameters $2R_{\mathrm{ant}}$, given the desired directivity D_{set}. The method start by calculating the average element area using $A_{\mathrm{elem}}^g = 4\pi R_{sph}^2/(N_a 2\sqrt{3}/\pi)$. A perfectly spherical system is assumed, setting the system radius R_{sph} equal to R_v. The factor $2\sqrt{3}/\pi$ is included to convert a regular hexagonal area to its inscribed circle area (roughly 10% smaller). The circular area is converted to element diameter using $2R_{\mathrm{ant}}^g = \sqrt{A_{\mathrm{elem}}^g/\pi}$. To take into account the effects of w_0 tapering, R_{ant}^g is fed into (6.5) to obtain the antenna far-field directivity. Finally, R_{sph} is numerically found by matching R_{ant}^g to the one required for D_{set}.

For estimation of the beam overlap points, we use the property of the icosahedron that all pentagons are separated angularly by 72°. The angle between two neighboring cells is then approximately $\theta_{\mathrm{est}} = 72°/m$, where m is one of the Goldberg topology parameters. Therefore, the directivity at the overlap point is estimated using

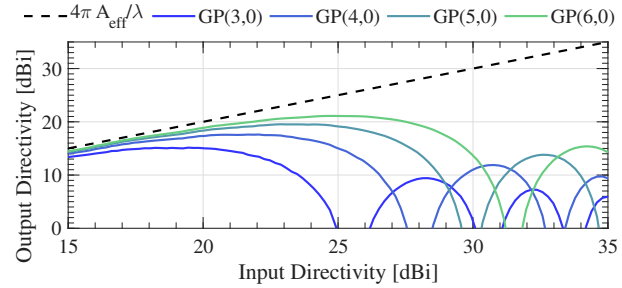

(a)

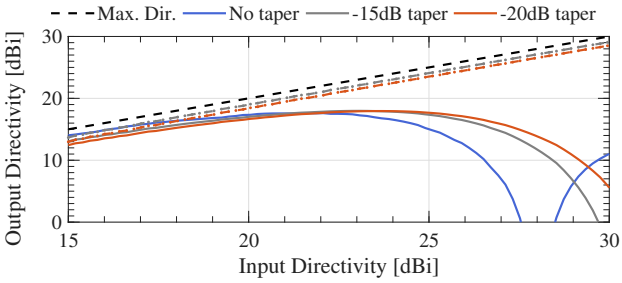

(b)

Figure 6.5: Modeling the behavior of the antenna spheres. (a) The relationship between the input (maximum) directivity and the directivity of the beam crossover points D_o, for various topologies. (b) The same modeled behavior of GP(4,0), but now after introducing different antenna amplitude taperings to reduce SLL.

$$D_o^{\mathrm{g,dB}} = D_{max}^{\mathrm{dB}} + FF_{\mathrm{norm}}^{\mathrm{dB}}\left(\theta_{est}/2\right). \tag{6.16}$$

This function is plotted as a function of input directivity in Fig. 6.5a for various topologies. Importantly, the figure is independent of frequency and therefore generally applicable. For low values of the antenna sphere radius R_{sph}, the overlap directivity D_o approaches the directivity associated to the maximum broadside directivity D_{max}, as makes intuitive sense. As R_{sph} is further increased, the overlap directivity D_o tends to increase gradually, until a maximum is reached. Beyond this maximum, the overlap directivity values decay faster than the increase in maximum directivity can compensate for. In this case, Scaling R_{sph} is counter-productive towards meeting system link budget requirements.

Instead, to achieve a higher overlap value, one option is to opt for a higher-order Goldberg topology, that has a smaller θ_{est}. Another way to increase D_o with respect to D_{max} is by changing the beam waist coefficients w_0 of the antenna apertures. Fig. 6.5b shows the effect of the input/output directivity behavior. By adding a taper, the main beam becomes wider, thereby increasing D_o. As shown, this comes at the cost of reducing the maximum directivity.

6.5. Performance Overview

The optimization procedure explained in Sections 6.3 and 6.4 can be performed for a variety of different Goldberg topologies. In this work, four topologies were investigated: GP(m, n) for $m = 3 \ldots 6$. As a higher-order topology is selected, more unique antennas and unique vertices are required, resulting in an increased amount of independent variables. This section studies the performance impact of the different topologies.

Table 6.1 summarizes the obtained performance for the various Goldberg topologies. The increasing amount of unique antennas and vertices are shown in the second and third columns. The time per iteration is shown in the 5^{th} column, indicating a growing runtime as higher-order topologies are used. The sixth column shows the runtime when the interference analysis is used, roughly doubling the required computation time. Note that these values depend on how well the optimizer is able to converge on the provided cost functions.

The listed runtimes indicate that the calculation of interference is computationally heavy. This is due to the calculation of the full sphere containing all antenna normals, and the subsequent sorting algorithm.

Table 6.1: Method time per iteration for various Goldberg topologies. The final column includes the calculation of the channel interferences.

GP	Unique Ants.	Unique Vertex	Total Ants.	time/iter (s)	time/iter (s) + C/I calc.
(3,0)	3	3	93	0.2039	0.5225
(4,0)	4	5	156	0.3294	0.9514
(5,0)	6	7	237	0.8246	1.3178
(6,0)	7	9	336	1.4798	2.6637

System: AMD Ryzen 7 7700 8-Core @3.80GHz, 64.0GB DDR5 RAM

6.6. Antenna System Design Examples

In this final section, two use-case scenarios are introduced, both operating at 150 GHz D-band frequency and using GP(6,0) topologies. The first aims to equalize the directivities of the beam overlap points at an approximate -3 dB with respect to the maximum directivity. Such scenario could be particularly useful when considering radar or sensing applications, as low directivity beam overlaps could result in 'blind' spots in the field-of-view.

The second case investigates a communication link scenario in a low-range indoor scenario (e.g. a concert hall or convention center). For communications, the interference also requires careful optimization.

6.6.1. Case I: Uniform Hemispherical Far-field Coverage

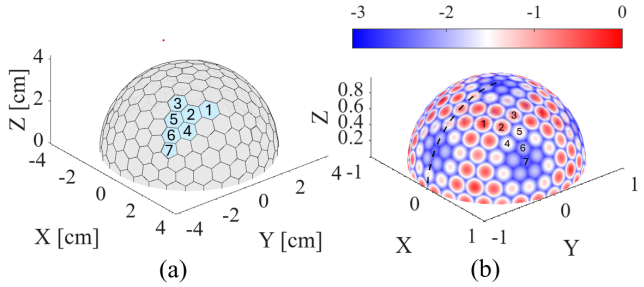

Figure 6.6: (a) The resulting GP(6,0) geometry of the optimization for minimum overlap directivity variance. Unique antennas have been marked in blue. (b) Far-field radiation sphere of the optimized array with roughly -3dB overlap points.

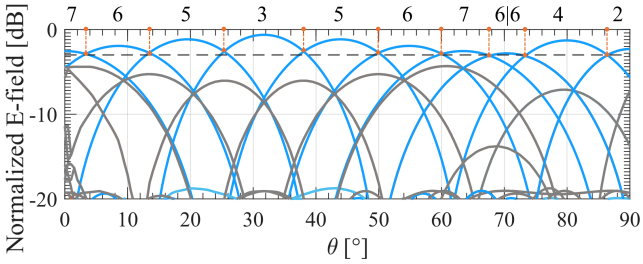

Figure 6.7: 1D cross-section of the patterns indicated in dotted line in Fig. 6.6b. As shown, the patterns achieve a -3dB overlap, indicated in the horizontal black dashed line. The blue lines are associated to the antennas directly along the cross-section, whereas the gray lines are their neighboring antennas. Associated unique antenna numbers of Fig. 6.6 are assigned to each angular cell.

Using the cost functions for the beam crossover points and the maximum directivity, the optimizer can solve towards a low variance of beam crossover points. The solver is initialized to solve for a $D_{\text{set}}^{\text{max}}$ of 21.1 dBi, providing a system radius initial guess of R_{v}^{g}= 3.6 cm. The weight for this maximum directivity is set a low 0.01 value, to allow the optimizer to sweep over different system radii. By contrast, the cost function weight for the minimum variance of D_{o} is set to 1. The interference cost function is not applied, and therefore amplitude tapering for reduced SLL is not applied (i.e, $w_0 = 1$).

The optimization took 24.73 seconds, using 10 iterations. Fig. 6.6a shows the final optimized array design, where the unique antennas are indicated in blue. Its

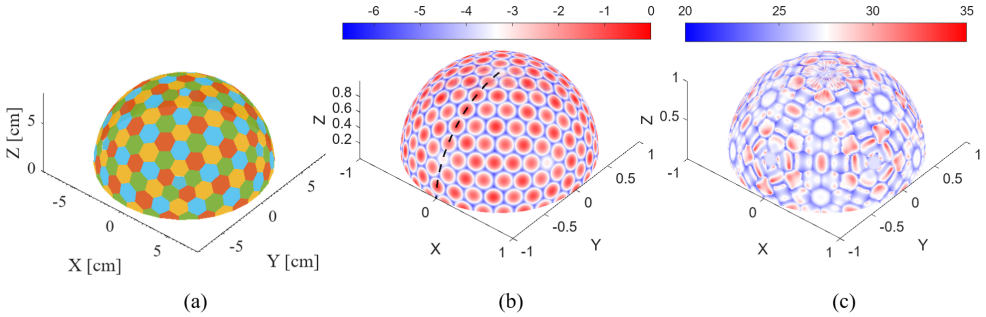

Figure 6.8: Example GP(6,0) communication scenario including the interference analysis. (a) The optimized antenna sphere. The colors represent the frequency reuse scheme. (b) The normalized far-field patterns in dB of the antenna sphere. (c) The far-field C/I ratio (in dB) for the sphere.

corresponding normalized far-field radiation sphere is shown in Fig. 6.6b. The black dashed line indicates the cross-section from $\theta = 0$ to $\theta = 90°$, shown in Fig. 6.7. The overlap points were established at -3.07 dB with respect to the maximum, with a standard deviation of only 0.09 dB. Interestingly, the method achieved uniformity by gradually reducing the antennas in size from the central element 1 (Fig. 6.6a) to outer pentagonal element 7. This is more clearly visible in Fig. 6.6b and the column 'Case I R_{ant}' of Table 6.2.

As shown in the 1D cross-section in Fig. 6.7, the pentagonal antennas have negligible contribution to the far-field patterns, as their angular cell sizes are only a few degrees in cross-section. For this reason, such array design would not work well when considering interference. For the central vertices that are in the middle of the hexagonal grid, the C/I is around 9 dB. These values match well to an analytical MBA analysis with $N_f = 4$ of [115] (8 dB C/I), where many assumptions are used (e.g. regular grid with fixed -3 dB overlap). The same assumptions were made in [35]. However, resulting C/I levels at the pentagonal overall point was found to be 0.97 dB. The next section therefore optimizes with C/I in mind.

A list of the parameters is shown in Table 6.2. The index in column 1 represents either the unique antenna or the unique vertex. The antenna indices correspond to those in Fig. 6.6a, with index 7 being the pentagonal antenna.

6.6.2. Case II: Communication Channels

For a realistic communication link scenario, a low-range 30 m communication link is envisioned. This case also considers the co-channel interferences, which can be a limiting factor to the SNIR. The same GP(6,0) topology was chosen, such that larger

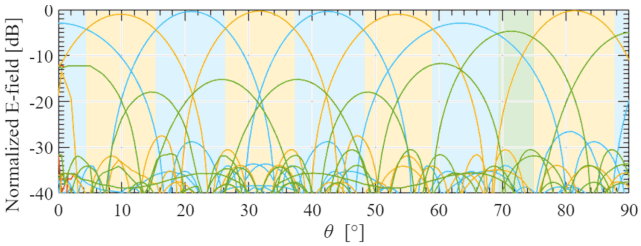

Figure 6.9: Normalized E-field patterns over the cross-section indicated in Fig. 6.8b. The colors are matching to the frequency reuse index of Fig. 6.8a. Different angular cells are indicated using the corresponding background colors.

antenna directivities can be attained without sacrificing too much the beam overlap points.

This time, the solver is initialized for a $D_{\text{set}}^{\max}$ of 27.72 dBi and a high w_0 of 0.45 (-10.72 dB taper). The high taper is required to reduce SLL. The initial guess of R_{v}^{g} was 8 cm and the weights for the maximum directivity, beam overlap variance and interference were all set equally to 1. $C/I_{\text{set}}^{\text{dB}}$ is set to 17 dB. The frequency reuse factor N_f was set to 4.

The optimized system geometry is shown in Fig. 6.8a. Fig. 6.8b shows the resulting normalized far-field sphere in dB, and Fig. 6.8c shows the C/I ratio of the antenna sphere in dB. At zenith, interpolation errors occur that are ignored for analysis. A worst-case C/I of 20.23 dB was obtained, located at the beam overlap point, confirming the assumption that C/I is worst at these locations.

Such high C/I was achieved by mainly utilizing two effects. First, the antennas rely on heavily reduced SLL to avoid co-channel interference. This becomes more evident in Fig. 6.9, indicating the normalized 1D cross-sectional patterns of the black dotted line in Fig. 6.8b. The colors used are those associated to the frequency reuse index of Fig. 6.8a. Highest levels of interference occurs in the vicinity of the pentagonal antennas. SLL lower than -25 dB were used to reduce significant summation of interferers at large angles.

Second, the antenna sphere has a large difference of up to 6.61 dB between its maximum directivity (26.54 dBi) and its minimum overlap directivity (19.93 dBi). This way, the interferers are less directive at the overlap points.

Both these effects combined make the antenna sphere less efficient in terms of volume occupied versus minimum directivity. Table 6.2 contains the optimized parameters for this case as well, under the columns 'II'. The resulting inefficiencies lead to a near doubling of the final required antenna sphere diameter, compared to case I. Despite the doubling in diameter, the overlap directivities are similar. A less strict requirement on C/I could help make the design more compact.

Table 6.2: Optimized parameters or output for case I (-3dB overlap), and case II (communication scenario).

Index	$\mathbf{D_i^{max}}$**[dB]**		$\mathbf{D_o}$**[dB]**		**C/I[dB]**		$\mathbf{R_v}$**[cm]**		$\mathbf{R_{ant}}$**[mm]**		$\mathbf{w_0}$		**Taper*****[dB]**	
	I	II	I	II	I	II	I	II	I	II	I	II	I	II
1	22.31	26.54	19.37	19.93	8.47	20.71	3.81	7.40	4.1	8.1	1	0.32	0	-21.2
2	22.00	25.68	19.33	20.05	8.54	21.71	3.81	7.40	4.0	7.7	1	0.30	0	-24.13
3	21.68	26.24	19.29	20.71	6.93	21.17	3.80	7.40	3.9	7.0	1	0.42	0	-12.31
4	21.02	26.31	19.30	20.28	7.43	20.23	3.80	7.41	3.6	7.3	1	0.37	0	-15.86
5	21.15	26.16	19.30	20.32	5.98	20.73	3.80	7.41	3.6	7.3	1	0.36	0	-16.75
6	20.37	25.54	19.44	19.73	9.20	22.04	3.80	7.41	3.3	6.6	1	0.39	0	-14.27
7	19.76	23.60	19.20	20.26	2.90	20.26	3.80	7.43	3.1	5.1	1	0.44	0	-11.22
8	-	-	19.36	19.19	3.75	20.99	3.79	7.44	-	-	-	-	-	-
9	-	-	18.94	19.22	0.97	20.34	3.79	7.44	-	-	-	-	-	-

$*$ Derived from $\mathbf{w_0}$, not an optimization parameter.

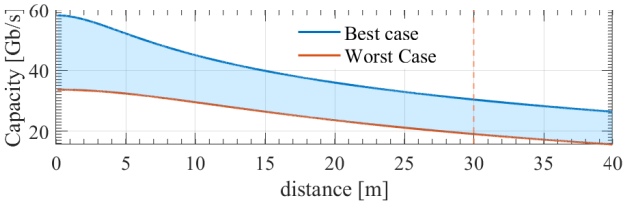

Figure 6.10: Shannon-Hartley maximum theoretical per-channel capacity for the GP(6,0) system of Fig. 6.8. Values are obtained as a function of distance. In red, the worst-case capacity, whilst blue indicates the best scenario.

From here, the overall system capacity can be calculated using the obtained far-field directivities and interferences. First, the interference and Signal to Noise Ratio (SNR) can be combined into the SNIR using

$$\mathrm{SNIR} = \left(\frac{1}{\mathrm{SNR}} + \frac{1}{C/I} \right)^{-1}. \tag{6.17}$$

Then, the SNR is calculated using the standard Friis' transmission equation. A frequency reuse scheme with $N_f = 4$ is used, and therefore the 20 GHz available bandwidth is subdivided into BW = 5 GHz per channel, as in [35]. A receiver antenna gain of 12 dBi is chosen, with a noise figure of 7 dB, and antenna temperature of 300 K. 15 dBm of transmission power is assumed. From here, the individual maximum theoretical channel capacities are obtained using the Shannon-Hartley limit, adapted for SNIR [116, 117]

$$C = \mathrm{BW} \log_2 (1 + \mathrm{SNIR}). \tag{6.18}$$

The per-channel capacity is calculated using (6.18) for the worst-case scenario at the beam crossover points, and for best-case scenario at the antenna element broadside. For the worst case, a C/I of 20.23 dB and $D = D_o = 19.93$ dBi were used. The best-case is represented by the maximum C/I of 35 dB and $D^{\max}$ of 26.54 dBi.

Fig. 6.10 shows the resulting theoretical per-channel capacity as a function of distance for both of these cases. At low distances, the system is interference dominated, whereas at larger distances the reduced signal power decreases overall system capacity. Multiplying the best and worst-case per channel capacities with the number of antennas in a hemisphere (128), gives the overall estimated system throughput of 3.9 and 2.4 Tb/s, respectively, at 30 m distance and a total bandwidth of $N_f \times \mathrm{BW} = 4 \times 5$ GHz. Such high throughputs are enabled by using the high-order spatial multiplexing properties of the system.

6.6.3. Discussion

Based on these two cases, the following recommendations can be made: First, when considering a radar and/or sensing scenario with uniform -3dB coverage, the pentagonal antennas have negligible impact and could even be omitted.

Second, as found empirically, with the current frequency reuse scheme an acceptable C/I with only -3dB beam overlap was not possible. If this is required, a higher order reuse scheme with e.g. $N_f = 7$ is recommended, sacrificing in turn some channel bandwidth in the process.

Finally, the GP(6,0) topology was restricted in minimum directivity to around 20 dBi, when also requiring sufficient C/I ratio and $N_f = 4$. To reach directivities of $>$ 30 dBi, it is estimated that a GP(17,0) is required, featuring a total of 1300 antennas in a hemisphere. Such large Fly-Eye arrays are only practically feasible due to the 60-fold icosahedral symmetries, since the unique antennas of a GP(17,0) are in the range of 22 units.

6.7. Conclusion

This chapter introduced a novel method to optimize the geometry of spherically conformal Goldberg antenna arrays, built upon the mathematical framework of recently published work. The method introduced three antenna-defined cost functions, that help optimize the array for directivity, beam crossover points and interference. A method for approximating an initial guess was described, providing additional intuition behind the behavior of such type of arrays. Finally, two cases for uniform far-field coverage and communication channels were discussed, indicating the tradeoffs that occur in such spherical designs.

The work can be extended to a range of other applications. One interesting example is converting the MBA to a hybrid phased-array or approach, where the individual antenna elements can be electronically scanned. This way, the number of elements in the spherical array can be reduced whilst maintaining the same performance. Another example could be to introduce panels with multiple passively scanned antenna elements, as in [22]. In addition, more complex antenna characteristics such as polarization, asymmetric radiation patterns and higher-order frequency reuse schemes can be included in the cost functions in the future.

Chapter 7

A Two-Tier TRL Calibration Technique to Assess Flip-Chip Interconnects at D-Band

In this chapter, a calibration technique is presented to evaluate flip-chip technology performance at D-band frequencies. The work was presented at the ARFTG conference and can be found in its proceedings. This section will provide an overview of that published work. The method involves the addition of a (second-tier) Thru-Reflect-Line (TRL) calibration within the flip-chip to extract the complex two-port S-parameters of the individual interconnects on back-to-back coplanar-wave (CPW) structures on a fused silica substrate. The calibration quality can be achieved by the high fabrication and assembly accuracy of the flip-chip interconnects and the thin-film technology. In addition, the TRL-based approach allows, without loss of accuracy, to offset the calibration reference plane from the vertical transition one, thus minimizing the impact of radiation losses during the modeling step.

7.1. Introduction

ASSESSING the impact of flip-chip interconnections up to sub-terahertz frequencies, relies conventionally on characterization approaches based on back-to-back cascading [118–121]. While these methods allow for a simple estimation of the overall back-to-back loss, they do however not provide information on the match level at the internal interfaces.

In this chapter, we present a technique for accurately assessing the performance of flip-chip interconnect technology at D-band frequencies. This method relies on the

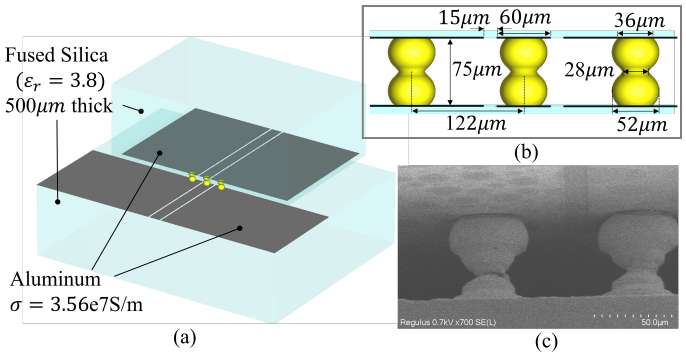

Figure 7.1: (a) Flip-chip simulation structure with a detailed view of the Au stud bumps in (b). (c) SEM micrograph of the Au stud bumps.

precise mechanical and lateral alignment achievable with the flip-chip bonding balls placement, together with the high resolution inherent in the thin-film technologies employed in the RF interposer/calibration structures. By leveraging these features, we enable the use of Thru-Reflect-Line (TRL)-like calibrations, known for their exceptional accuracy, even at such high frequencies. Thus, we propose the use of an additional TRL calibration alongside the conventional back-to-back CPW approach to effectively extract the complex two-port S-parameters of an individual flip-chip interconnect. This chapter is structured as follows: Section 7.2 introduces the flip-chip and thin-film technology utilized in this calibration. Section 7.3 outlines the calibration procedure, while Section 7.4 presents the measurements obtained through this methodology.

7.2. Flip-Chip Interconnect Technology

Back-to-back CPW transitions, discussed in this contribution, were all developed on a fused-silica substrate (ε=3.8 and $\tan\delta$=6e-4) of 500 µm with a front-side metallization of 1 µm of aluminum (σ=3.56e7 S/m). Thermal-compression gold stud-bumping technology was employed for all structures manufactured for this contribution. A chip-to-interposer height of approximately 75 µm was realized to reduce the influence of the bottom substrate on the top-chip CPW lines. The SEM photograph of the gold stud-bumping structures is shown in Fig. 7.1, each bump had a width of around 50 µm. Two stud bumps are bonded on top of each other, one attached to the interposer, and the other attached to the small chip. A 3D model of the physical structure, shown also in Fig. 7.1 was extracted from the SEM

measurements and was used in section 7.4 to correlate the measurement results with EM simulations.

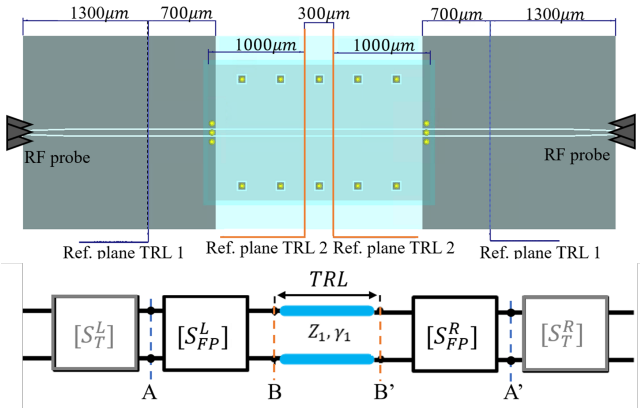

Figure 7.2: (a) CAD drawing of the back-to-back CPW calibration structure employed including physical dimensions. (b) Cascade of the S-parameter blocks of the back-to-back TRL.

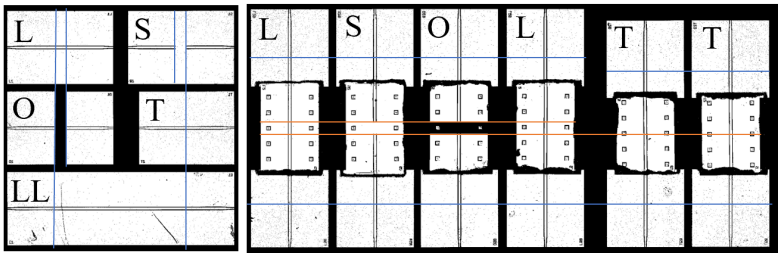

Figure 7.3: TRL1 (a) and TRL2 (b) calibration kits for de-embedding until plane A (blue) and B (red), respectively (Fig. 7.2).

7.3. Two-Tier TRL Calibration Technique

The characterization was realized on a back-to-back CPW structure, shown in Fig. 7.2. Since the TRL measurement is a 2-port measurement, it implies the use of two sets of flip-chip interconnections. A first TRL calibration kit, shown in Fig. 7.3, de-embeds the landing probe transitions until the reference plane A (Fig. 7.2). This first structure $[S_T]$ is a CPW with a conductor/gap width of 30/10 µm (70Ω),

which transitions to a CPW of 60/15 µm (64 Ω). The first CPW is designed with a minimum signal/gap to minimize the excitation of the common mode when landing the RF probe. The second CPW is designed to have a conductor width according to the flip-chip stud bump width, i.e. around 60 µm. Both CPW lines have been designed for minimum radiation losses. Fig. 7.4 presents the total loss characteristics of 50 Ω and 100 Ω CPW lines in relation to their overall width t (gap+signal+gap), including both ohmic and radiation contributions, calculated using [50]. As depicted, the radiation loss of the CPW lines is proportional to the line width t directly, while the ohmic loss depends on the impedance (i.e. on the central line width). If $t <$ 100 µm, the CPW lines exhibit radiation losses below 0.1 dB/mm. The reference plane A is placed at a distance of 0.5 λ_0, where λ_0 is the free space wavelength at the central frequency to enable smooth transition and minimize its coupling of the RF probe.

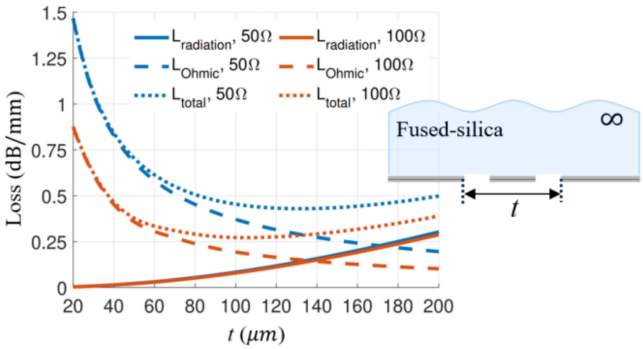

Figure 7.4: Losses of the CPW line in between air and infinite fused-silica medium versus the total CPW width t, as defined in the inset

A second TRL is implemented at reference plane B, on the top chip, shown in Fig. 7.3. This second TRL allows us to isolate the S-parameter matrices from the two flip-chips and obtain the CPW line characteristics of the top chip. The higher the top chip is placed, the less it is affected by the bottom substrate, but the higher is the radiation from the flip-chip interconnection. As mentioned, the top and bottom chips are positioned at 75 µm as a compromise. Finally, if the probe landings were too close to the flip-chip interface, coupling between the two (radiating) elements could influence the measurement results. To minimize this radiative coupling of the flip-chip to reference planes A and B, straight CPW lines of distance $\approx 0.36\ \lambda_0$ and $0.5\ \lambda_0$ are used respectively.

The flip-chip CPW calibration structures have been simulated using an EM full-wave simulator to verify the sensitivity of our calibration procedure. The comparison is shown in Fig. 7.5, where the simulation of the flip-chip interconnect

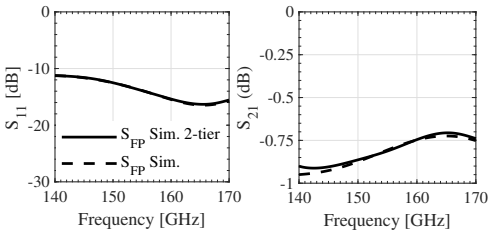

Figure 7.5: Simulated flip-chip transition S_{11} (a) and S_{21} (b) of the two-tier calibrated data (solid), versus the directly simulated transition (dashed).

$[S_{\mathrm{FP}}]$, is obtained via the 2nd-tier TRL calibration (solid line) and via a direct simulation of the transition (dashed line). As shown in the figure, a good agreement is obtained within 0.01 dB.

7.4. Measurements

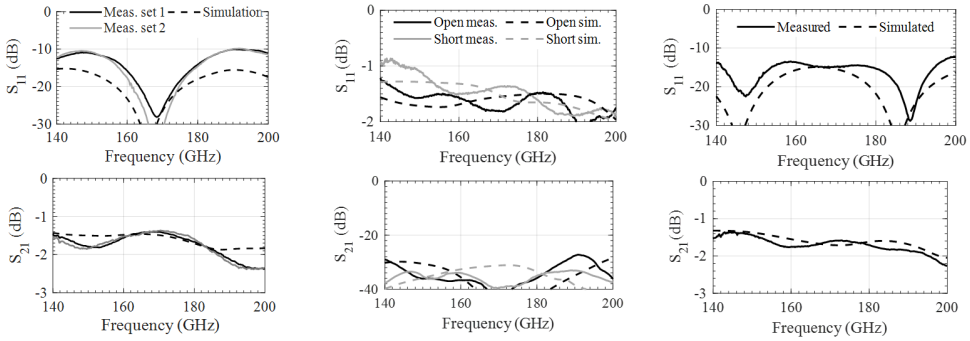

Figure 7.6: Measured (solid) and simulated (dashed) S_{11} (top) and S_{21} (bottom) parameters for the three TRL components.

In the following section, the proposed calibration approach to flip-chip assessment has been characterized and compared with simulations. The characterization was realized on a two-port probe-landing station using WR5.1 frequency extenders in combination with a vector network analyzer (VNA). All calibration structures were measured, and the subsequent section presents the results in detail.

7.4.1. First-Tier TRL Calibration Results

After the 1st tier TRL calibration, the landing probe transition structures $[S_T]$ were de-embedded and the reference planes were set to A (see Fig 7.2). The measured S-parameters from each structure are shown in Fig. 7.6 and are compared against their respective simulation. The reflection coefficients are better than -10 dB within the frequency band for both thru and LINE cases, as expected from the simulated interconnections. The insertion loss displays comparable performances to the simulated values, with an agreement within 0.5 dB for the thru and LINE cases. The return loss is within 0.4 dB for the REFLECT-short and open configurations.

7.4.2. Second-Tier TRL Calibration Results

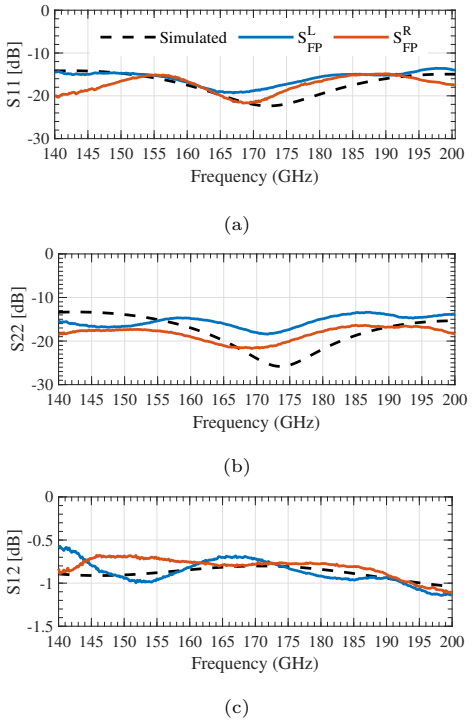

Figure 7.7: Measured (solid) and simulated (dashed) S-parameters of the flip-chip transition for the S_{11} (a), S_{22} (b) and S_{21} (c). Both the left and right transitions are indicated.

The second-tier TRL calibration is applied using the back-to-back configuration described in section 7.3, to extract the S-parameters of the flip-chip interconnect and the parameters of the transmission line β. Fig. 7.7 shows the magnitude of the S-parameters of the flip-chip interconnects $[S_{FP}]$, extracted from the TRL calibration structures shown in 7.3. The agreement with the simulated structures is fair, and the measured data shows a reflection coefficient below -13 dB across the band, and an average loss from the transition of 0.7 dB.

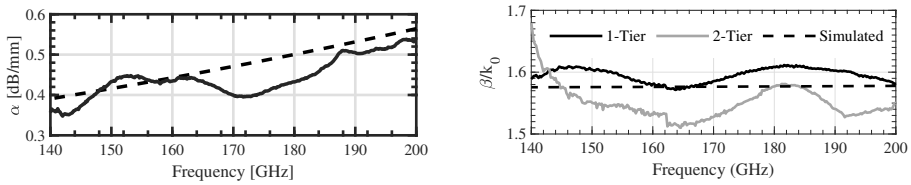

(a) (b)

Figure 7.8: Measured (solid) and simulated (dashed) normalized propagation constant β (a) and attenuation constant α (b).

The propagation constant of the CPW lines from the top and bottom chips has been extracted from the two TRLs and is shown in Fig. 7.8a. Both measurements obtain similar behavior across the band and have a fair agreement with the simulated value. As shown, the fused silica on the bottom of the chip has minimum impact on the top CPW line. The attenuation constant of the bottom CPW line was determined from the S_{21} measurement of a long line using the first TRL calibration (Fig. 7.8a), showing good agreement with the simulated value. Regrettably, the attenuation constant could not be extracted from the second TRL due to the short length of the line and its minimal loss ($\approx$. 0.13 dB).

Since this method allows the measurement of the propagation constant of the CPW lines, it allows to further de-embed the lines and isolate the flip-chip transition. For instance, in Fig 7.9, the total loss of the transition ($|S_{11}|^2 + |S_{12}|^2$) is depicted when 500 µm of the CPW line from reference plane A and 800 µm CPW from reference plane B are de-embedded ($S_{FP,D}$). As illustrated, the resultant loss attributed to the flip-chip transition is approximately 0.25 dB, showing a very good agreement with the simulations as well.

Overall, we can see that the 2nd-tier TRL provides consistent results with the simulated values, with an agreement of 0.1 dB across the band. The 1st-tier TRL is not affected by the presence of the chip, and the level of cross-talk between the CPW lines enables accurate de-embedding of the interconnection lines up to the flip-chip transition. The data measured with this approach validates the full-wave simulation of the 3D model which could be used to design chip-package transitions.

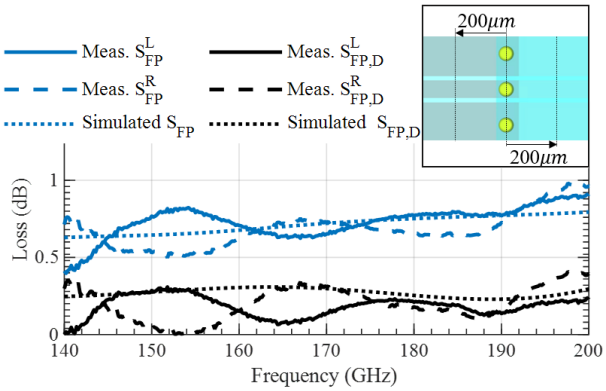

Figure 7.9: Total loss ($|S_{11}|^2 + |S_{21}|^2$) of the flip-chip transition SFP between interfaces A and B (Fig. 7.2) are shown in blue. In black, the transmission lines are de-embedded ($S_{FP,D}$) using ABCD matrix transfer until 20 µm away from the flip-chip stud bumps (see inset).

7.5. Conclusion

A calibration technique has been presented to assess the flip-chip interconnect at D-band frequencies. Calibration structures with long, thin, reference-plane-based CPW lines on low-permittivity packages, enable a low-cross talk between the three CPW lines and thus, an accurate measurement of the transition at such high frequencies.

The extracted results of the flip-chip interconnect have been compared with standard two-port back-to-back CPW transition measurements and full-wave simulations, showing the validity of the measurement techniques as well as the good estimation of the flip-chip loss. As expected, the flip-chip interconnects provide a low-loss and wideband transition, that will be used for the AiP integration in the upcoming Chapter 8.

Chapter 8

Integrated Front-End Prototype at D-Band Frequencies

This chapter presents the progress made towards a functional integrated Fly's-Eye Front-end. The antenna-in-package with fused-silica interposer will be combined with the dual-lens architecture, presented in Chapter 2. Various design strategies are followed to ensure compact form factor within the lens footprint. The technique uses standard PCB technologies, with specialized lithographically printed fused-silica interposers. Flip-chip technologies are used to combine RFICs with different functionalities onto a single low-loss interposer, forming a functionally heterogeneous approach. The prototype is currently in the final stages of fabrication.

8.1. Introduction

THE Goldberg architecture proposed in Chapter 6 aims to achieve full spherical coverage for a communication system with antenna architectures possessing many individual elements. Conformal arrays are an actively researched topic to overcome antenna scan limitations, where the positioning and orientation of the antenna elements follow a non-planar surface. Unfortunately, the implementation and design of such conformal arrays is in practice difficult to achieve, especially at higher frequencies. At lower frequencies, conformal array architectures are found in various configurations, with a wide variety of antenna element types. Fig. 8.1 provides a number of examples of conformal arrays found in literature, albeit at relatively low frequencies (max 18 GHz) and with limited number of elements (max 64). Strategies to aim for higher number of elements at higher frequencies are missing.

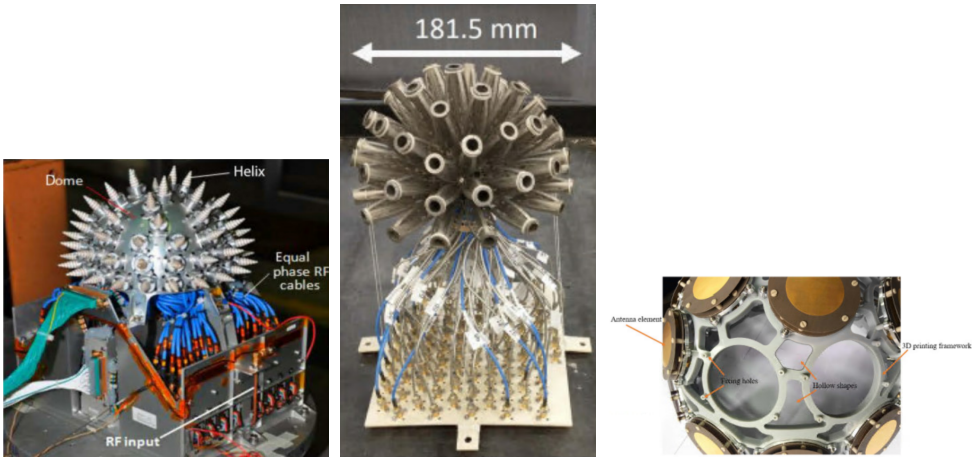

Figure 8.1: Examples of spherically conformal arrays found in literature. In (a), (b) and (c), the arrays consist of helix antennas [109], Vivaldi antennas [108], and patch antennas [122], respectively

In this chapter, we propose a novel front-end integration strategy to achieve a spherically conformal Fly-Eye system at D-band. The Goldberg architecture, proposed in Chapter 6, is realized here using the core-shell lens (presented in Chapter 2) as an array element, as shown in Fig. 8.2a, where the entire front-end is integrated under one shell lens footprint. The figure shows an example layout specified as G(10,0) with 2000 faces [123]. A shell lens diameter of 3.5 cm was chosen to meet the Fly's-Eye system power budget demands (Chapter 1), which sets the upper bound to the front-end dimensions. Integration below the lens footprint enables a vertical package and a complete modular architecture. To achieve full spherical coverage, both hexagons and pentagons are required to form the Goldberg polyhedron. Fig. 8.2b shows how such a mathematical entity may be filled with integrated core-shell antenna elements.

The chapter begins by providing a top-level overview of the electronics schematic in Chapter 8.2. Then, the integration concepts in section 8.2.1, followed by an in-detail explanation of the design phase for the fused-silica wafer in section 8.3.2 and the PCB in section 8.3.3.

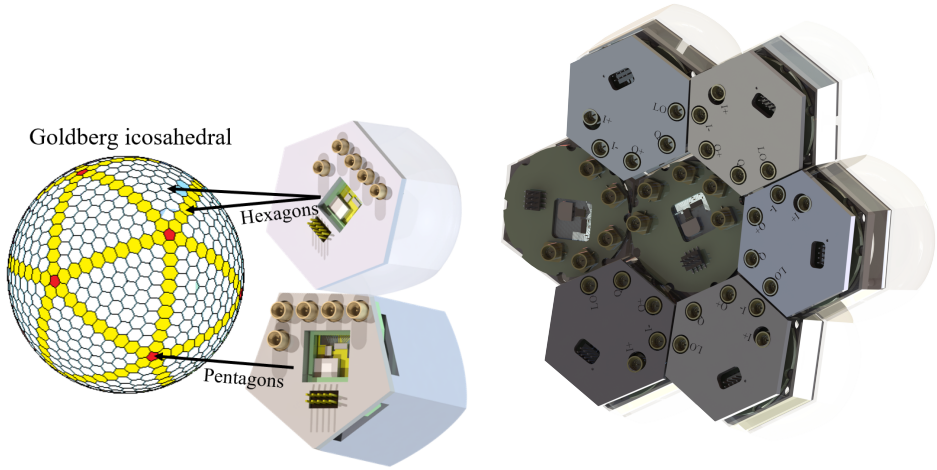

(a) (b)

Figure 8.2: (a) Example spherical Fly's-Eye system composed of hexagons and pentagons. (b) Artist impression of a 7-element subsection of the spherical Fly's-Eye communication system.

8.2. Single Element Front-End Technology

The envisioned integration concept is shown in Fig. 8.3a. The modular Fly's Eye front-end has a three-level integration. First, an RF PCB is used as a carrier board and routs the < 20 GHz signals and DC biasing lines from the external connectors to the AiP interposer using a standard Ball Grid Array (BGA) interface. Second, the fused-silica interposer is used as a high-frequency transition between the PCB and the two commercially purchased GaAs MMICs (forming the third layer), and also contains the double-slot feeding antenna. The RF front-end is composed of two commercially available MMICs; The first is an LO x6 multiplier chain, that multiplies the $\approx$ 12 GHz LO to a 71-86GHz signal. The second MMIC is a sub-harmonic mixer that up-converts the DC-6GHz IQ signal onto the frequency doubled carrier to 140-170GHz. For now, the antenna will be a single metallized layer (i.e. CPW-fed antenna of the previous year's report) since this design has now been well characterized and provides a less complex fabrication.

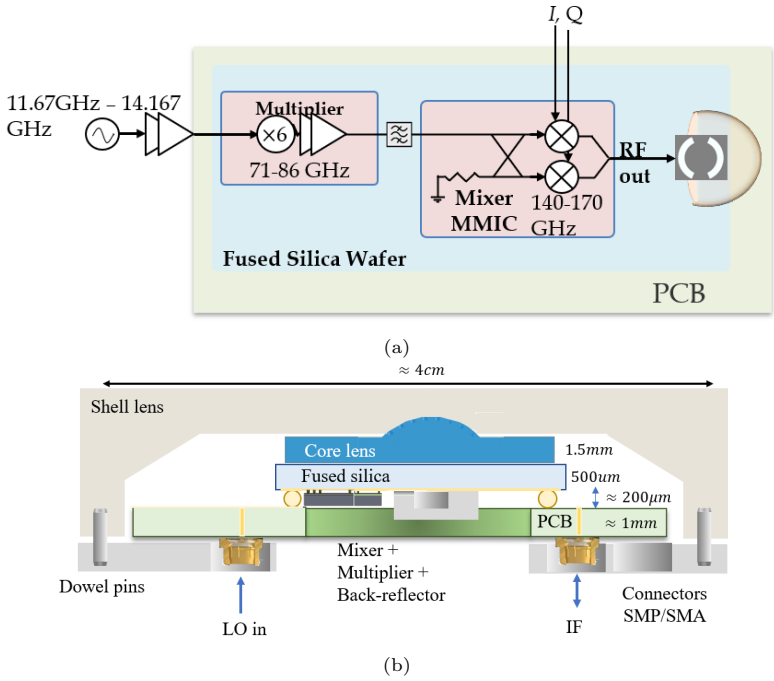

Figure 8.3: (a) Schematic overview of the proposed front-end integration in Tx mode. (b) Cross-sectional view of the front-end integration concept. The LO and IF signal paths are indicated, propagating through the RF PCB, through the fused-silica wafer, processed by the flip-chipped MMICs and finally arriving at the core-shell lens antenna.

8.2.1. Front-End Integration Technology

The integration technology, including flip-chip, will be provided and performed by the Chip Integration and Technology Center (CITC) in Nijmegen. Once the top-level technology has been fixed, a more detailed design strategy could be developed. Fig. 8.3b shows a cross-sectional view of the proposed front-end. The RF PCB of laminate type RO4350B provides interconnection for LO and IF sources using Sub miniature Push-on Micro (SMPM) connectors. These connectors provide both the compactness necessary for integration on limited footprint, and the ability to quickly connect or reconnect external interfaces. The BGA interconnect with a standard pitch of 500 µm is located at the center of the PCB. To allocate clearance for the Surface-Mount Devices (SMDs) on the fused-silica once flip-chipped, the PCB has a routed cut-out section that enables the RFICs and antenna back-reflector to be positioned unobstructed.

Key to the AiP integration concept is the placement of the multiplier on the fused silica, to avoid the need for ≈ 80 GHz signals passing through the PCB or BGA packaging. The lack of a thermal sink on the flip-chipped interposer, however, leads to thermal management problems that will need to be addressed. The multiplier MMIC has a typical power dissipation of 0.5 W, and could result in the possibility of heat buildup inside the device due to the poor thermal dissipation of the small flip-chip bonds. To overcome this problem, a copper heat sink will be glued onto the silicon carrier of the GaAs MMIC (Fig 8.4). The heat can then be dissipated from the heat sink by thermal convection.

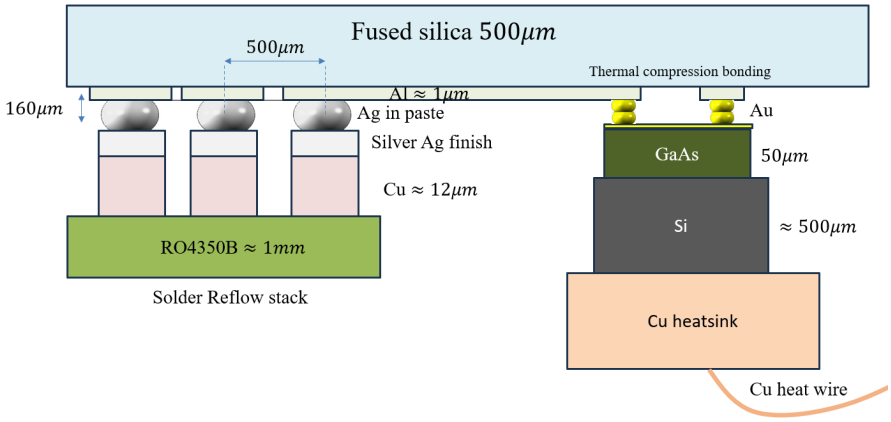

Figure 8.4: Bonding stack for both the BGA-package on the left and the thermal compression bonding for the MMICs on the right.

Fig. 8.4 shows the bonding stack and the different involved materials. The PCB to fused silica interconnect is made using the BGA interconnect (left), and the fused silica to GaAs using flip-chip thermal compression bonding (right). For the metal finishing of the fused-silica wafer, the choice was made to go with Immersion Silver (ImAg). This is to avoid having to grow a thick nickel layer on the fused silica when using gold patterning (Electroless Nickel Immersion Gold (ENIG)) since this process would require outsourcing to an external company. Instead, the silver finish allows a direct connection between the ImAg PCB and fused silica, by bonding using Ag sintered paste. The MMICs will be thermal compression bonded to the silver-plated fused-silica wafer using the flip-chip technique described and characterized in Section 7. For structural support, silicon carriers are added to the back of the GaAs MMICs, after which the copper heat sink can be added for convective thermal dissipation.

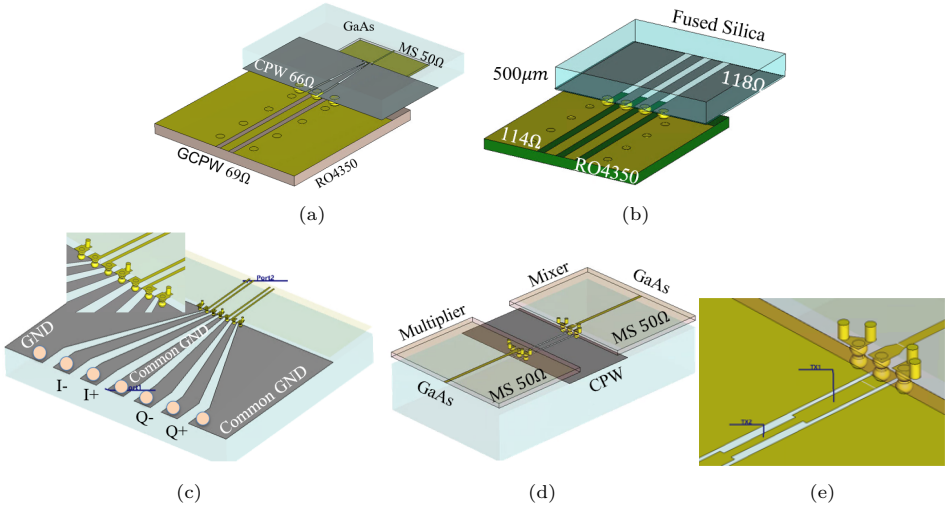

Figure 8.5: RF interconnections for the MMIC integration with the antenna. (a) The LO transition from PCB to FS to GaAs at ≈14GHz. (b) The Differential IF transition from PCB to FS at DC-6GHz. (c) Differential IF transition from FS to GaAs at DC-6GHz. (d) Transition from GaAs multiplier to FS to GaAs mixer at WR10 frequencies. (e) The transition from GaAs to Fused-silica at WR5 with a matching structure included.

8.3. Prototype Design

8.3.1. Interconnects and Transitions Design

As shown in Fig. 8.3, various interconnections are required in the different signal paths, these include the LO and differential IQ IF from PCB to fused silica to GaAs at 15GHz and DC-6GHZ, respectively. Each interconnection was designed in CST microwave studio and is shown in Fig. 8.5. Refer to the caption of this figure for specifications. All interconnections were designed for $S_{11} < -10$ dB for matching. Once fully designed, they were placed on the fused-silica interposer design to accommodate the BGA packaging and MMIC components. Fig. 8.6a shows the preliminary 3D view of the fused-silica wafer with the integrated MMICs, back-reflector, and antenna. The BGA interface with 500 μm pitch is visualized, interconnecting the LO, IF, and several DC transmission lines. The aluminum back-reflector will be glued onto the wafer as a standard SMD.

Not shown in the overview is the decoupling and filtering network required for the MMIC multiplier. To limit the effects of voltage ripples on the MMIC's internal amplifiers and multipliers, parallel capacitors and series resistors are positioned close

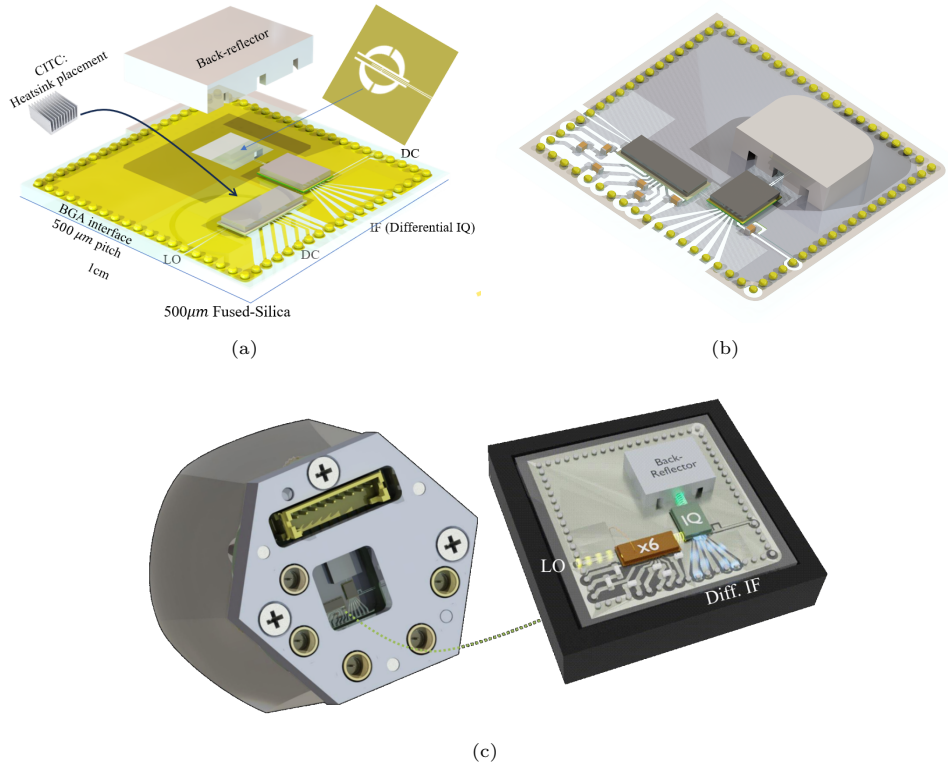

Figure 8.6: (a) 3D conceptual view of the integrated antenna front-end with fused-silica interposer (b) Final version including the capacitors for the decoupling network. (c) The integrated front-end below a shell lens.

to the input terminals of the device. However, since there is only limited space on the fused-silica interposer, we decided to place only the most critical high-frequency noise-filtering capacitors on the wafer. Lower frequency filtering structures are then allocated to the PCB, where more space is available. The final wafer design incorporating these networks, the RFICs, the back-reflector and the BGA interface is shown in Fig. 8.6b. The capacitors are very small 0402M components (0.4 mm $\times$ 0.2 mm), which cannot be soldered by hand but will instead be placed by CITC on the interposer. Finally, Fig. 8.6c shows the full CAD design of the front-end, all positioned below a core-shell lens footprint.

8.3.2. Fused-Silica Mask Design

The designs are placed on a 4" fused-silica wafer for lithographic processing, together with various other test structures, as shown in Fig. 8.7a. Fig. 8.7b shows the individual elements that constitute the mask design. Note that the mask is vertically mirrored because the metal layer will be positioned on the bottom side, connected to the BGA package. They include: (1) the 10 µm integrated antenna of [64], which was slightly modified to improve S_{11} matching performance. (2) The 5 µm integrated antenna, designed for improved radiation pattern quality with lower cross-polarization. (3) The same 10 µm antenna as in (1), but now replacing the multiplier MMIC with a WR10 probe landing for improved redundancy in case of problems with the IC. (4) Standalone multiplier MMIC for testing with probe landing. For characterization, we have included both WR-5 (5) and WR-10 (6) TRL calibration structures. (7) provides us with an additional 10 μm CPW-fed antennas for probe-fed characterization of the antenna, in case the situation requires. Finally, (8) and (9) are the probe-fed multiplier + mixer and standalone mixer test structures. All components have been distributed evenly over the 4-inch wafer to reduce the risk of wafer imperfections, such as photo-resist residues.

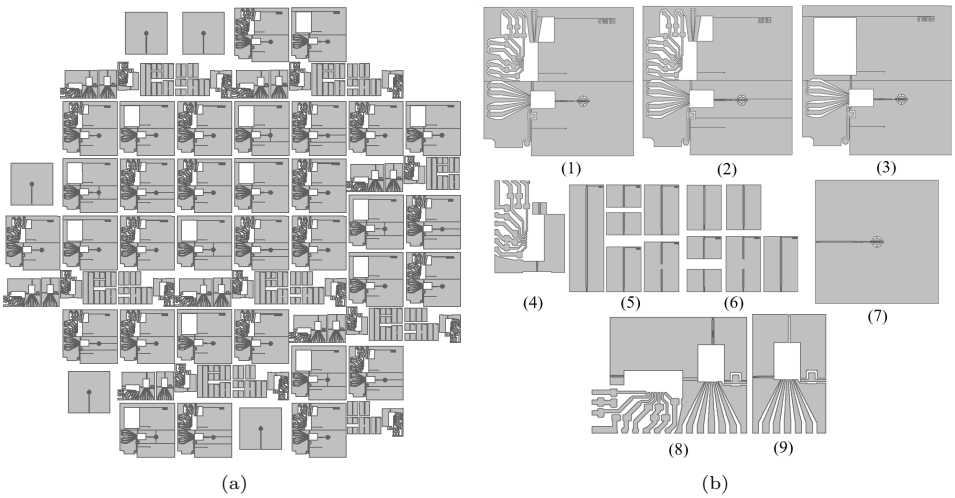

Figure 8.7: (a) Mask design for 4-inch fused-silica wafer with 500μm thickness. The mask includes various elements that are repeated over in the 4-inch circle. (b) An overview of the different structures in (a).

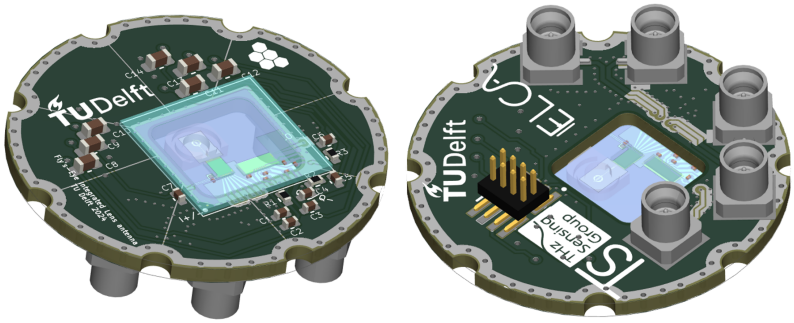

(a) (b)

Figure 8.8: Preliminary PCB design for the integrated front-end. The board diameter is only 2.7cm to allow for a compact integration below the shell lens.

8.3.3. PCB Design

The previous section described the design process for the fused-silica interposer. Its BGA interfaces were the DC biasing lines, and the LO and IF transmission lines at ≈14 GHz and 6 GHz, respectively. Also, the CPW-fed double slot antenna can be considered as an interface of the WR5 signal to the two lenses. This section discusses how these interfaces are integrated into a new Fly's-Eye antenna prototype.

The purpose of the PCB is to integrate the fused-silica interposer with external components, such as the filtering capacitors and SMPM RF board connectors, which would not fit on the fused-silica wafer. It also adds structural rigidity to the thin, fragile glass interposers. Fig. 8.8 shows the top and bottom view of the preliminary PCB design. The fused-silica wafer, back-reflector, SMT and MMIC components have also been included for reference. Key to integration is the compactness of the PCB since the board needs to fit under the shell-lens footprint (≈ 3.5 cm diameter). For this reason, the board is chosen to be 4 layers with RO4350B material, suitable for 15 GHz signals whilst still presenting a cost-effective solution using standard PCB manufacturing. As shown in the top view of Fig. 8.8a, the aforementioned PCB cutout is located in the center of the BGA footprint, where the ICs, back-reflector, and SMD capacitors have enough clearance from the board. Next to the BGA, the PCB includes the capacitors and resistors for the remainder of the decoupling and filtering networks, positioned as close as possible to the ICs. After filtering, the DC lines are connected by a compact 1mm pitch 2×4 DC connector. The LO and IF connections are transitioned to the other side of the board (see Fig. 8.8b), and connected by SMPM connectors that provide a very miniaturized footprint of only 3.7 mm × 3.7 mm. This allows the board diameter to shrink to 2.8 cm, compact enough to fit under a shell lens of 3.5 cm. The LO and IF lines are via stitched to

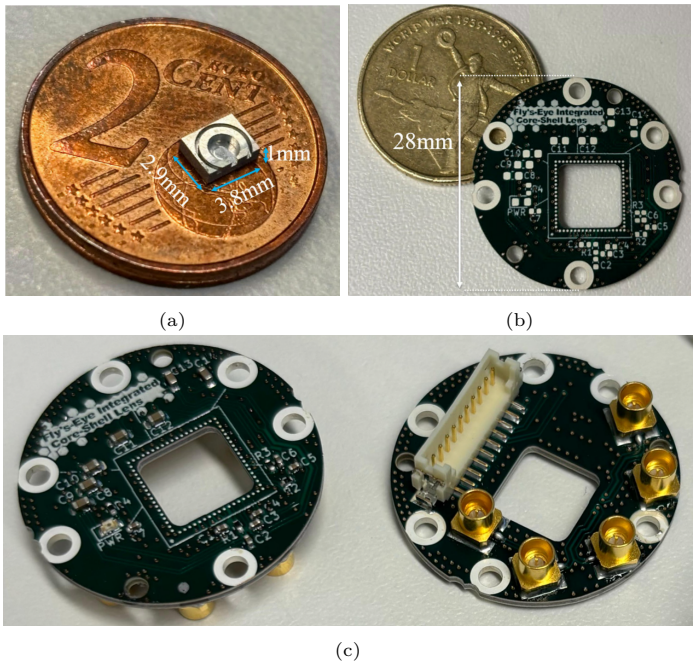

(a) (b)

(c)

Figure 8.9: (a) CNC machined aluminum back-reflector. (b) Fabricated Ag-finished PCB before assembly and (c) the PCB after fully assembled.

provide an enclosed signal path. Finally, the IF is both differentially and I/Q length matched to limit mismatches in the mixer MMIC.

8

8.3.4. Prototype Development

Fig. 8.9a shows the CNC fabricated back-reflector and its dimensions. For reference, a 2 cent Euro coin is added in the background to indicate its small scale. The pre-assembled ImAg PCB is shown in Fig. 8.9b, and finally the assembled boards are shown in Fig. 8.9c.

Unfortunately, during the integration of the front-end prototype, the bonding of the MMICs and capacitors to the interposer did not perform as intended. Although the initial flip-chip bonding of the MMICs onto the fused-silica interposer was successful, the assembly failed after the placement of the decoupling capacitors. The curing of the assembly on the hot plate after the placement of the capacitors

introduced mechanical stress at the flip-chip bonding interfaces of the MMICs, causing both the multiplier and IQ mixer to detach from the fused-silica substrate.

These results highlight the need for further technical development of the bonding technology to achieve a fully functional front-end module. In particular, using gold metallization on the fused-silica interposer instead of aluminum could enhance the adhesion strength between the bumps and the substrate. Moreover, it would be convenient to avoid the direct placement of capacitors on the fused-silica interposer and integrate them only on the PCB. These redesigns of the assembly minimize the thermal exposure after the flip-chip bonding step and consequently also reduce the risk of MMIC detachment.

Chapter 9

Conclusion and Future Work

This thesis was dedicated to the development of novel sub-THz antenna architectures, measurement techniques, and integration techniques. Below, a brief conclusion is provided for every part, followed by recommendations for future lines of research. Finally, the impact of the research in terms of scientific contributions will then be stated.

D-Band Integrated Lens Antenna Design

The first part of this doctoral thesis focused on the development of novel integrated lens-antenna architectures for high-frequency wireless communication and sensing. A novel core-shell lens design was proposed in Chapter 2, which combines the high front-to-back ratio of a dense core lens, with the electrically large and low-loss properties of the shell lens. The latter provides the bulk of the required directivity for the Fly's-Eye system. A spherical interface between the core and shell lenses with an anti-reflective layer minimized the impact of the transition between the two. The architecture enables in-package integration of the electronic front-end within the shell lens footprint, by positioning a double-slot antenna and its feeding lines on a low-loss fused-silica interposer. Its design was both theoretically demonstrated, and optimized using full-wave solvers.

Then, Chapter 3 presented an improvement on the spherical core lens of Chapter 2. Difficulties in integration of the spherical interfaces were addressed by adjusting the architecture towards a physically flat interface, which has the same electrically spherical transition as the earlier work. The lens was able to achieve similar performance, whilst mitigating many alignment problems. This allows the architecture to be more easily scalable towards Fly's-Eye arrays beyond 1000 lens elements. Fur-

thermore, a variation of the spherically conformal lens was proposed by extending the spherical lens surface in the vertical direction. This so-called hyper-hemispherical lens was shown to be able to trade off the directivity with reduced sidelobe levels, a property that becomes particularly useful in later chapters on system integration.

A flat core lens prototype was developed with cross-compatibility with the previous prototype in mind, to enable direct measurement comparison later on. Both flat and spherical core lenses were fabricated using 5-axis CNC machining techniques. The resulting compact lens prototypes have a height of only 2.2 mm (1.13 λ_0) and a diameter of 6.6 mm (3.4 λ_0). The compactness enables such a core lens to fit directly inside an RFIC encapsulation. Both antennas have been added to Table 9.1 for comparison to the state-of-the-art. The used feeding technologies, lens materials, and their losses are shown in columns 3-6. Good bandwidth and gain have been obtained, when compared to the other works.

QO Measurement Techniques

The second part of this thesis focused on quasi-optical measurement systems for the characterization of both high-gain probe-fed antennas and dielectric materials. In Chapter 4, a planar near-field measurement scheme using quasi-optical elements was devised to measure probe-fed antennas at D-band frequencies. To achieve this, first, a 45-degree mirror was used to isolate the probe landing site from the mechanical vibrations of the planar scanner. Then, a two-tier TRL calibration method was introduced to calibrate the antenna-under-test until the desired antenna reference plane. Two lens antennas of Chapters 2 and 3 were characterized, providing good agreement between simulations and measurements. The measured antennas were compact, well-performing, and with high degree of integration, suitable for the Fly's-Eye system.

Then, Chapter 5 proposed a new lens architecture for high-frequency material characterization purposes. High purity plane-waves with high Gaussicisity were generated in the near-field using hyperboloid dielectric lenses. These plane waves propagated in a dense dielectric material, allowing for significant suppressing of field spreading effects, compared to standard free-space setups. The flat lens interface allowed for a high-accuracy QO TRL calibration, and additional ease-of-assembly when measuring materials-under-test. Samples can be positioned between the lens interfaces, and extraction of full-matrix S-parameters over a 140-220 GHz frequency band was possible. Using a full-wave simulation approach, direct plane-wave generation was found to have a Gaussicity of > 94 % was achieved from 160 GHz to 215 GHz. A high port-to-port coupling of up to -3 dB was achieved. The wideband antenna properties allow the usage of time-gating techniques to mitigate the impact of multiple reflections. Two MUTs were characterized using full-wave simulations with high ac-

curacy. Prototype development is currently being performed. The lens design could also enable applications in other fields, such as near-field telecommunications.

Spherical Fly-Eye System Design, Optimization & Integration

The third and final part of this thesis tackled the overall Fly-Eye design and integration aspects. In Chapter 6, a novel spherically conformal antenna architecture was introduced, built upon a mathematical Goldberg polyhedron. Such architecture was shown to provide numerous advantages over standard phased-array topologies, such as reduced complexity, no scan loss, wideband performance, easy scalability and mitigation of thermal buildup. The chapter utilized a novel method to optimize the geometry given a series of analytically-defined antenna cost functions, including directivity, beam crossover points and interference. A method for approximating an initial guess was described, providing further intuition behind the array behavior. Finally, two cases for uniform far-field coverage and communication channels were discussed, indicating the tradeoffs that occur in such spherical designs. Due to the 60-fold symmetries, a reduction in the number of unique elements could be made, making design of the array less intensive and enabling mass manufacturing.

Then, the thesis focused on the integration of the front-end within a single lens element footprint. Chapter 7 started by providing a calibration and measurement technique for the characterization of sub-THz flip-chip interconnects using full S-parameter matrices. A high-accuracy two-tier TRL technique was used to isolate the interconnect, enabling de-embedding of all other parts of non-interest. A flip-chip interconnect used for the Fly-Eye system was measured and simulated, indicating good agreement between both. The interconnect has been shown to be suitable for use in high-frequency systems, owing to its low loss and wideband performance.

Finally, Chapter 8 made an attempt at combining all previous works, by integrating the electronic front-end into the AiP fused-silica interposer. For this purpose, different RFICs were combined using the aforementioned flip-chip technology of Chapter 7 onto the interposer, which was specially designed to house the leaky-wave feeding antenna of Chapter 2. CNC machined back-reflectors were added as a surface-mount device for improved compactness. The fused-silica interposer could then be combined with the core-shell lenses onto an RF PCB using standard ball-grid-array technology. The whole design could fit within the designated 3.5 cm diameter footprint of the shell lens, making a vertically integrated and modular package possible. While the prototypes were not yet complete at the time of writing, the chapter concluded with several design improvements based on challenges encountered during fabrication.

Future Work

The research lines of the present dissertation can be further developed according to the following statements

D-Band Integrated Lens Antenna Design

For the core-shell lens architecture of chapters 2 and 3, further exploitation of the added degrees-of-freedom could be performed. This way, different antenna behaviors could be achieved, such as reduced SLL or pattern shaping into Gaussian or 'top hat' forms. While the work implemented both a CPW- and microstrip-fed printed antenna, the latter was not fully functioning. The microstrip-fed double-slot antenna has shown potential for reduced transmission line loss and improved pattern quality, and could be further developed. Such a multilayer approach could also enable dual-polarized antenna radiation, key to many communication scenarios. On the fabrication side, further efforts could be dedicated towards the design of such lens architectures towards even higher frequencies. To make the flat core lens more suitable for mass manufacturing, special drilling tools could be ordered, such that instead of drilling + milling, a single drill could extrude the matching-layer cavities. However, to make all these optimizations possible, of particular interest would be a theoretical model that describes RF performance of such core-shell lens, instead of relying on time-consuming full-wave solvers.

QO Measurement Techniques

The chapters 4 and 5 related to RF measurement and characterization could also be further developed. For the near-field planar QO measurement setup of chapter 4, overall improvements could be made to reduce the scattering in between the AUT, mirror and RF measurement probe. For instance, by including additional RF absorbing material, and a larger mirror aperture, such rippling effects could be further reduced. Also, the setup could be improved by adding the possibility for measuring active RF components alongside the antenna, instead of measuring a passive antenna only. Due to the decoupling of the front-end with the mechanical scanner, such options are available. In the future, the characterization of array front-ends at D-band will become important. The measurement techniques developed in this thesis could be extended towards a system characterization with over-the-air measurement of multiple simultaneous modulated signals.

For Chapter 5, the most obvious future development would be the measurement of the fabricated prototype. At the time of writing, this is in process. The potential of the high-efficiency lens with flat interface could be further explored in other research or application fields, such as wireless connectivity or near-field communications and sensing scenarios. After measurement validation, the hyperboloid lens design could be potentially further optimized by improving the Gaussicity of the lens, for instance, by allowing a more rigorous fit of the lens to the feeding antenna phase distribution.

Spherical Fly-Eye System Design, Optimization & Integration

Finally, for the third part related to the Fly's Eye system integration and optimization, several recommendations for future research can be made. In the system optimization of Chapter 6, the cost functions could also include different radiation properties (e.g. top hat patterns, fan beams or polarization) to allow for a more realistic communication scenario. The link to the core-shell lens could be made, thereby exploiting the degrees-of-freedom offered by the core-shell lens architecture. Furthermore, hybrid Fly's-Eye arrays with active scanning elements could be implemented, thereby meeting the middle ground between the compactness of phased arrays and the reduced complexity of Fly's-Eye arrays. In addition, the research has shown that for the Fly's Eye, 1000 elements are necessary, therefore techniques to simplify the modeling of such large arrays is needed to be efficiently integrated in the code. Finally, future work could also include a full-wave simulated or technological demonstration of the proposed optimized beam properties, such as the overlap points and obtained interference levels.

For Chapter 7, more rigorous testing of the effects of the radiative coupling between the RF landing probes and the flip-chip interconnects could be made. Comparison to theoretical models of the flip-chip interconnect could also provide further insight into the accuracy of the RF probe landing whilst measuring. Finally, whilst Chapter 8 presented the design and initial fabrication of the front-end, more development is needed to realize the flip-chip-based packaging of the MMICs onto the fused-silica interposer. After reliable flip-chip processing is completed, a full experimental validation of the proposed Fly-Eye system can then be realized. Such validation is currently not possible at D-band without the integrated front-end. Future validation could demonstrate the potential of the D-band Fly-Eye system for communication and sensing applications.

9.1. Impact of the Research

The work described in this dissertation has led to numerous scientific contributions. An overview of all journal and conference contributions is provided in 'List of Publications' on page 179.

The conference contribution numbered C.3 was awarded for the *Best Antenna Theory & Design Paper Award*, at the European Conference on Antennas and Propagation EuCAP 2022. The conference contribution numbered C.4 was nominated for the *Best Applied Technology Antenna Paper Award*, also at the EuCAP 2022.

Table 9.1

State-of-the-Art of High Gain Antennas at D-Band Frequencies

Ref #	Antenna architecture	Feed technology	Feed Loss[d]	Lens Material	Lens Loss[d]	η_{ap}^{a} (%)	Dir. (dBi)	Gain (dBi)	f_c (GHz)	BW (%)
[17]	Transmit array with horn	Waveguide (CNC)	-	3-layer PCB (Rogers)	<1dB	38.3[b]	-	33[b]	145	11.7[c]
[18]	Transmit array with horn	Waveguide (CNC)	-	3-layer PCB (Rogers)	<1dB	32[b]	-	32[b]	150	16.8[c]
[19]	24x16 slot array	Gap waveguide (CNC)	-	-	-	78	-	33.8	145.8	5.5
[23]	Integrated lens with LW waveguide feed	Waveguide (CNC)	1.6	HDPE	0.3	83	33.8	31.9	165	50
[27]	Integrated lens with 2×2 patch array	High-density interconnect process with 4 metal layers	2.6	ABS-M30	3.2	48	34.6	28.5	127	20
This work	Core-shell integrated lens with LW double slot	Fused silica with 1 metal layer	1.2	HDPE, PPE950	0.5	66	33.2	30.1	155	32
This work	Core-shell integrated lens with LW double slot	Fused silica with 2 metal layers	0.4	HDPE, PPE950	0.5	66	33.2	30.5	155	25
This work	Flat Core-shell integrated lens with LW double slot	Fused silica with 1 metal layer	1.2	HDPE, PPE950	0.5	66	33	29.8	155	32

[a]Aperture efficiency of the lens without the lens feed, [b]Peak value,
[c]3dB gain bandwidth, [d]in dB.

IV

Appendices

Appendix A

SNR Analysis for Fly's-Eye and Phased-Array Architectures

Phased-array antenna systems are seen as a promising architecture for D-band for flexibly reconfigurable antenna patterns. Their ability to achieve both high antenna gains whilst combining the power of a large number of elements makes them suitable for achieving the required link budgets. While this is true when phased-array systems only target a limited number simultaneous beams, the concept does not hold for true multibeam system requirements. To demonstrate this, we analytically solve for the SNR for both the phased-array and the SNR for the proposed Fly's-Eye array.

When comparing the multi-beam Fly's-Eye array to an actively electronically scanned phased array, we can analytically demonstrate that the two architectures achieve similar SNR, when evaluating with the same number of elements. To do this, we use the general Friis' transmission equation for SNR [124]

$$\mathrm{SNR} = \frac{P_t G_t G_r \left(\frac{\lambda}{4\pi R}\right)^2}{k_B T \mathrm{BW}}, \tag{A.1}$$

where k_B is the Boltzmann constant, T is the antenna temperature (in Kelvin), BW is the system bandwidth, G_t and G_r are the antenna gains for transmitters and receivers, respectively. P_t is the total transmitted power, and, finally, the term $(\lambda/(4\pi R))^2$ is the spherical spreading factor at distance R using wavelength λ. In [29], it was found that atmospheric absorption was negligible for small distances, and will therefore also not be included here.

We will now demonstrate, first for a phased-array topology, and then for a Fly-Eye architecture, the obtained SNRs per cell. This demonstration will be performed over a full sphere, with a solid angle Ω_s of 4π sr.

A

For the analysis, a number of assumptions are made. First, both topologies use N number of elements, where each element has a transmit power of P_e. The total transmit power P_t then equals NP_e. Furthermore, we assume fully symmetric beams, without any scan loss. To simplify analysis, both topologies are assumed to have no antenna loss, e.g. $G = D$ for both transmit and receive antennas. Furthermore, the directivity of the receiving antenna D_r is fixed.

A.0.1. Phased array SNR analysis

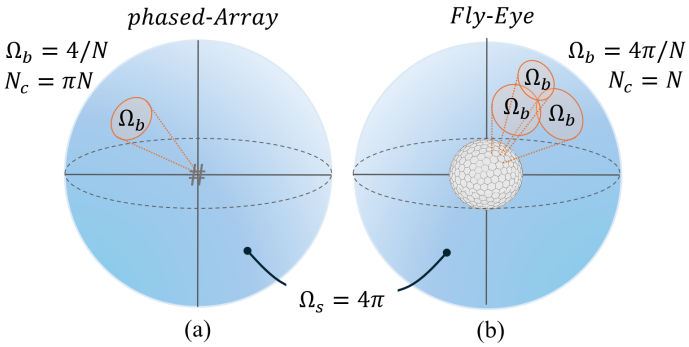

Figure A.1: Far-field solid angle for the (a) phased-array topology, and (b) the Fly-Eye topology.

For the phased-array topology, an inter-element spacing of $\lambda/2$ is used, resulting in an aperture size of $A = N\lambda^2/4$, assuming a square planar array with $N_x = N_y = \sqrt{N}$. From this aperture size, the phased-array directivity is estimated using $D_{\text{pa}} \approx 4\pi A/\lambda^2 = \pi N$. We can now estimate using the directivity, the number of cells or, equivalently, the number of beams in the full sphere. Since the directivity is related to the beam solid angle, we derive $\Omega_{\text{c}} \approx 4\pi/D_{\text{pa}} = 4/N$ [15]. The number of cells is therefore equal to $N_{\text{c}} = \Omega_s/\Omega_c = 4\pi/\Omega_{\text{c}} = \pi N$. The phased-array system has to either simultaneously transmit in all these directions, if possible, or the cells are divided in time (or a combination of the two). The former results in a drop in transmit power per cell by P_t/N_c, whereas the latter effectively requires an increase of N_c in BW to compensate for the reduction in dwell time and achieve the same capacity.

Combining all above-mentioned observations into (A.1) provides

$$\text{SNR}_{\text{Phased-Array}} = \frac{\pi N^2 P_e D_r \left(\frac{\lambda}{4\pi R}\right)^2}{N_c k_B T \text{BW}} = \frac{4\pi N P_e D_r \left(\frac{\lambda}{4\pi R}\right)^2}{\Omega_s k_B T \text{BW}} \tag{A.2}$$

A.0.2. SNR for a Fly's-Eye Multi-Beam Array

For the Fly's-Eye scenario, the entire sphere is subdivided into N_c cells, which is assigned to a single element, therefore $N_c = N$. Since there is no active scanning, the power each cell transmits is equivalent to $P_t = P_e$. The beam solid angle then follows from $\Omega_b = \Omega_s/N$, from which the directivity is approximated using $D = 4\pi/\Omega_b = N$ (assuming no power outside the main-lobe).

Again using (A.1), the SNR for a single cell of the Fly's-Eye array can be rewritten towards

$$\mathrm{SNR}_{\text{Fly-Eye}} = \frac{4\pi N P_e D_r \left(\frac{\lambda}{4\pi R}\right)^2}{\Omega_s k_B T \mathrm{BW}} = \mathrm{SNR}_{\text{Phased-Array}} \tag{A.3}$$

Now, comparing (A.3) to (A.2), we observe that the two are theoretically equivalent. This interesting observation permits us to start investigating under which practical circumstances, one architecture is preferred over the other.

The key takeaway message is that for the both the phased-array and the Fly's-Eye topologies, the SNR increases linearly as a function of the number of elements. For the phased-array, the individual elements must adhere to the $\lambda/2$ spacing. For the Fly's-Eye, the number of elements dictates the required antenna element directivity, and therefore aperture size. Therefore, its directivity enhancement comes from the (passive) volume of the lenses and the time-integration, whereas the phased-array relies on active components to superimpose the energies of all array elements. The downside to a Fly's Eye is then the resulting loss of compactness by relying on large lens apertures. However, this compactness is counteracted by moving towards higher frequencies, where phased-array implementations struggle.

Using a similar approach, a simplified SNR for the radar range equation can be extracted for both the Fly's-Eye and the phased-array topologies. Here, the receiver directivity is equal to the transmitter directivity, e.g. $D_r = D_t$. can be derived using

$$\mathrm{SNR} = \frac{P_t G^2 \lambda^2 \sigma}{(4\pi)^3 R^4 k_B T \mathrm{BW}} = \frac{4\pi P_e N^2 \lambda^2 \sigma}{\Omega (4\pi)^3 R^4 k_B T \mathrm{BW}}, \tag{A.4}$$

where a similar behavior occurs due to the increased dwell time of the Fly's-Eye, compared to the phased-array. The Fly's-Eye system trades of time resolution (increased integration time) and beam solid angle ($\Omega_c = \Omega_s/N$ versus $\Omega_s/\pi N$), in return obtaining a much less complex system that potentially enables more easily bi- or multi-static radar.

Appendix B

PREPERM Characterization at D-band frequencies

The performance of D-band high-gain lens antennas relies heavily on the electrical characteristics of the lens dielectric materials. Such materials are electromagnetically characterized by their complex relative permittivity given by

$$\varepsilon_r = \varepsilon_r' - j\varepsilon_r'', \tag{B.1}$$

where ε_r' is the real component of the permittivity, associated to the energy storage in the dielectric, whereas ε_r'' is associated to the dielectric loss. Both terms allow for the calculation of the dielectric loss tangent, obtained using $\tan\delta = \varepsilon_r''/\varepsilon_r'$. This appendix explains the measurement process and results of some of the D-band material characterization. Throughout this work, the relative permeability (μ_r) of all materials is assumed to be 1 (i.e. non-magnetic).

For characterization, a near-field lens-to-lens coupled measurement setup was used, shown in Fig. B.1a. The setup includes two corrugated leaky-wave lens antennas developed in [23], each generating a plane-wave-like aperture field in the WR-5.1 band, that couples well to the other lens once both are aligned in the near-field as in Fig. B.1a. The transmit and receive antenna are aligned using a CNC machine until the $S_{21,ref}$ coupling is maximized, thereafter serving as the reference for de-embedding antenna non-idealities. Similar to [125], a free-space TRL is performed to calibrate the system and to position the reference planes at the MUT boundaries.

Then, a Sample Under Test (SUT) is positioned at broadside incidence between the two antennas, and its $S_{21,SUT}$ is measured. Both $S_{21,ref}$ and $S_{21,SUT}$ are time-gated to limit the impact of the reflections in the test bench. Subsequently, we measure the relative difference between the reference and the sample under test

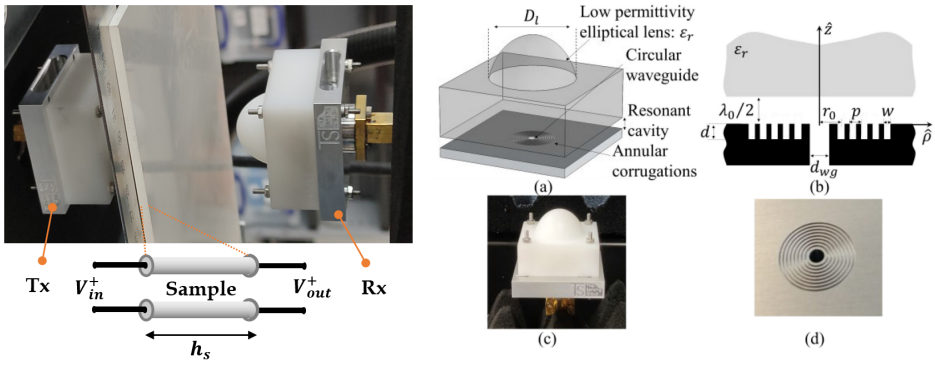

Figure B.1: (a) Lab setup for material characterization at WR5.1 frequency band. Bottom transmission line models the sample dielectric interface assuming plane-wave incidence. Different PREPERM thermoplastic samples with d=3mm were tested. (b) The lens antenna with corrugated ground-plane, taken from [23].

by taking $\Delta S_{21}^{meas} = S_{21,SUT}/S_{21,ref}$. To extract the ε'_r and $\tan\delta$ parameters, we solve the corresponding transmission line shown in Fig. B.1a, using the known sheet thickness h_s.

$$\frac{V^+_{in}}{V^+_{out}} = \frac{(1+\Gamma_B e^{-j2k_{zs}h_s})e^{jk_{zs}h_s}e^{-jk_{z0}h_s}}{(1+\Gamma_a)(1+\Gamma_B)}, \tag{B.2}$$

where k_{zs} and k_{z0} are the wavenumbers in the dielectric medium and in free space, respectively. The reflection parameters Γ_B and Γ_A are given by

$$\Gamma_A = Z_s \frac{Z^A_{in} - Z_s}{Z^A_{in} - +Z_0}, \tag{B.3}$$

$$\Gamma_B = \frac{Z_0 - Z_s}{Z_0 + Z_s}. \tag{B.4}$$

The input impendance is given by the following expression

$$Z^A_{in} = Z_s \frac{Z_0 + jZ_s\tan(k_{zs}h_s)}{Z_s + jZ_0\tan(k_{zs}h_s)}, \tag{B.5}$$

where Z_0 and Z_s are the impedances of free-space and of the dielectric medium, respectively. Ideal RF transmission of a loss-less dielectric slab is obtained when the thickness matches an integer amount of half-wavelengths:

$$n_1 l_1 = \frac{m\lambda_0}{2}. \tag{B.6}$$

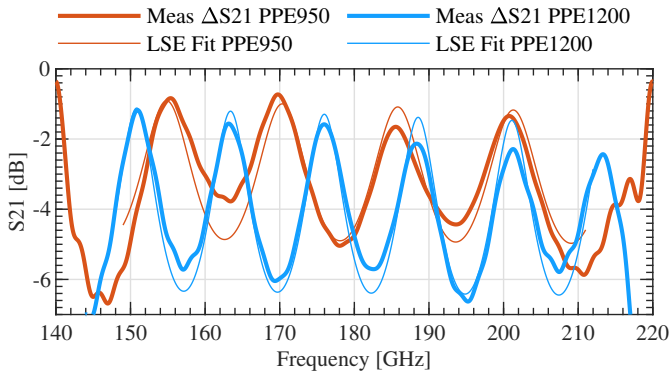

Figure B.2: The measured and fitted ΔS_{21} parameters for the PPE950 (orange) and PPE1200 (blue) materials.

TABLE B.1

PREPERM CHARACTERIZATION AT WR5.1

Material	Property	Datasheet (2.4 GHz)	Measured at WR5.1
PPE1200	Permittivity	12±0.5	14±0.4
	$\tan\delta$	0.001	0.006±0.002
PPE950	Permittivity	9.5±0.3	9.2±0.15
	$\tan\delta$	0.0009	0.005±0.002
PPE400	Permittivity	4±0.1	3.8±0.1
	$\tan\delta$	0.0009	0.004

where l_1 is the thickness of the slab, n_1 is the refractive index of the slab material, λ_0 is the wavelength in free space at the used frequency. Due to the wideband nature of the VNA and the WR-5 antennas, multiple peaks are observable in the allocated bandwidth.

Three sample sheets of 3x150x300mm of PREPERM were measured: PPE400, PPE950 and PPE1200, with permittivity and loss tangents as defined in Table B.1. The sheets were measured in a 4×8cm grid with intervals of 2cm. A Least Square Error (LSE) fit between the analytical transmission line S_{21} and the measured ΔS_{21}^{meas} over the 140-220 GHz bandwidth provides ε_r' and $\tan\delta$. Fig. B.2 shows the measured ΔS_{21} for both the PPE950 and the PPE1200 materials in red and blue, respectively. The results are summarized in Table B.1. The PPE1200 sheet showed a large offset in ε_r' (14 instead of 12) with some spatial variation in the order of 0.4.

The measured PPE950 sheet had ε'_r of 9.2, close to the documented value of 9.5. Only limited spatial variation in ε'_r of 0.15 was observed. Its $\tan\delta$ fluctuates over the different spatial locations, with values around 0.005 ± 0.002. PPE400 had ε'_r and $\tan\delta$ close to the datasheet with only minor spatial variation.

Bibliography

[1] C. E. Shannon, "A mathematical theory of communication," *The Bell System Technical Journal*, vol. 27, no. 3, pp. 379–423, 1948.

[2] S. Z. Aslam, A. Wilcher, B. Chatterjee, Y. K. Yoon, D. P. Arnold, and S. Sinha, "Challenges and opportunities in d-band transmitter architectures and antenna design, integration, and scalability for 6g communications: A brief review," *IEEE Access*, vol. 13, pp. 33 849–33 873, 2025.

[3] T. Kürner and S. Priebe, "Towards thz communications - status in research, standardization and regulation," *J Infrared Milli Terahz Waves*, no. 35, p. 53–62, 2014.

[4] T. S. Rappaport, Y. Xing, O. Kanhere, S. Ju, A. Madanayake, S. Mandal, A. Alkhateeb, and G. C. Trichopoulos, "Wireless communications and applications above 100 GHz: Opportunities and challenges for 6G and beyond," *IEEE Access*, vol. 7, pp. 78 729–78 757, 2019.

[5] T. S. Rappaport, S. Sun, R. Mayzus, H. Zhao, Y. Azar, K. Wang, G. N. Wong, J. K. Schulz, M. Samimi, and F. Gutierrez, "Millimeter wave mobile communications for 5g cellular: It will work!" *IEEE Access*, vol. 1, pp. 335–349, 2013.

[6] K. Rasilainen, T. D. Phan, M. Berg, A. Pärssinen, and P. J. Soh, "Hardware aspects of sub-thz antennas and reconfigurable intelligent surfaces for 6g communications," *IEEE Journal on Selected Areas in Communications*, vol. 41, no. 8, pp. 2530–2546, 2023.

[7] A. Karakuzulu, W. A. Ahmad, D. Kissinger, and A. Malignaggi, "A four-channel bidirectional d-band phased-array transceiver for 200 gb/s 6g wireless communications in a 130-nm bicmos technology," *IEEE Journal of Solid-State Circuits*, vol. 58, no. 5, pp. 1310–1322, 2023.

[8] S. Kueppers, T. Jaeschke, N. Pohl, and J. Barowski, "Versatile 126–182 ghz uwb d-band fmcw radar for industrial and scientific applications," *IEEE Sensors Letters*, vol. 6, no. 1, pp. 1–4, 2022.

[9] F. Liu, Y. Cui, C. Masouros, J. Xu, T. X. Han, Y. C. Eldar, and S. Buzzi, "Integrated sensing and communications: Toward dual-functional wireless networks for 6g and beyond," *IEEE Journal on Selected Areas in Communications*, vol. 40, no. 6, pp. 1728–1767, 2022.

[10] B. Razavi, *RF Microelectronics (2nd Edition) (Prentice Hall Communications Engineering and Emerging Technologies Series)*, 2nd ed. USA: Prentice Hall Press, 2011.

[11] T. Maiwald, T. Li, G.-R. Hotopan, K. Kolb, K. Disch, J. Potschka, A. Haag, M. Dietz, B. Debaillie, T. Zwick, K. Aufinger, D. Ferling, R. Weigel, and A. Visweswaran, "A review of integrated systems and components for 6G wireless communication in the D-Band," *Proceedings of the IEEE*, vol. 111, no. 3, pp. 220–256, 2023.

[12] J. Joung, C. K. Ho, K. Adachi, and S. Sun, "A survey on power-amplifier-centric techniques for spectrum- and energy-efficient wireless communications," *IEEE Communications Surveys & Tutorials*, vol. 17, no. 1, pp. 315–333, 2015.

[13] M. de Kok, A. B. Smolders, and U. Johannsen, "A review of design and integration technologies for d-band antennas," *IEEE Open Journal of Antennas and Propagation*, vol. 2, pp. 746–758, 2021.

[14] R. Chen, B. Yan, and M.-C. F. Chang, "A review of circuits and systems for advanced sub-thz transceivers in wireless communication," *Electronics*, vol. 14, no. 5, 2025. [Online]. Available: https://www.mdpi.com/2079-9292/14/5/861

[15] C. A. Balanis, *Antenna Theory: Analysis and Design*, 3rd ed. NJ, USA, John Wiley Sons, 2005.

[16] S. Shahramian, M. J. Holyoak, M. Sayginer, M. Zierdt, C. Adams, M. W. Mansha, J. Weiner, A. Rai, I. Kartam, and Y. Baeyens, "D-band radio-on-glass modules for spectrally-efficient fd & fdd multi-kilometer wireless backhaul links," in *2025 IEEE Radio Frequency Integrated Circuits Symposium (RFIC)*, 2025, pp. 47–50.

[17] F. Foglia Manzillo, A. Clemente, and J. L. González-Jiménez, "High-gain D-Band transmitarrays in standard PCB technology for beyond-5G communications," *IEEE Transactions on Antennas and Propagation*, vol. 68, no. 1, pp. 587–592, 2020.

[18] W. Saleh, Y. Letestu, R. Sauleau, and E. M. Cruz, "Design and measurements of a high-performance wideband transmitarray antenna for D-Band communications," *IEEE Antennas and Wireless Propagation Letters*, vol. 20, no. 9, pp. 1765–1769, 2021.

[19] D. Zarifi, A. Farahbakhsh, and A. U. Zaman, "A gap waveguide-based D-band slot array antenna with interdigital feed network," *IEEE Transactions on Antennas and Propagation*, vol. 71, no. 9, pp. 7124–7131, 2023.

[20] M. A. Campo, G. Carluccio, S. Bruni, and N. Llombart, "Dielectric gratings enhancing the field of view in low dielectric permittivity elliptical lenses," *IEEE Transactions on Antennas and Propagation*, vol. 69, no. 11, pp. 7308–7322, 2021.

[21] S. K. Karki, J. Ala-Laurinaho, and V. Viikari, "Low-profile scanloss-reduced integrated metal-lens antenna," *IEEE Transactions on Antennas and Propagation*, vol. 70, no. 2, pp. 876–887, 2022.

[22] M. Arias Campo, D. Blanco, S. Bruni, A. Neto, and N. Llombart, "On the use of fly's eye lenses with leaky-wave feeds for wideband communications," *IEEE Transactions on Antennas and Propagation*, vol. 68, no. 4, pp. 2480–2493, 2020.

[23] S. Bosma, N. van Rooijen, M. Alonso-delPino, and N. Llombart, "A wideband leaky-wave lens antenna with annular corrugations in the ground plane," *IEEE Antennas and Wireless Propagation Letters*, vol. 21, no. 8, pp. 1649–1653, 2022.

[24] J. R. Costa, M. G. Silveirinha, and C. A. Fernandes, "Evaluation of a double-shell integrated scanning lens antenna," *IEEE Antennas and Wireless Propagation Letters*, vol. 7, pp. 781–784, 2008.

[25] M. Kokkonen, A. Ghavidel, N. Tervo, M. Nelo, S. Myllymäki, and H. Jantunen, "An ultralight high-directivity ceramic composite lens antenna for 220–330 GHz," *IEEE Access*, vol. 9, pp. 156 592–156 598, 2021.

[26] K. Konstantinidis, A. P. Feresidis, C. C. Constantinou, E. Hoare, M. Gashinova, M. J. Lancaster, and P. Gardner, "Low-THz dielectric lens antenna with integrated waveguide feed," *IEEE Transactions on Terahertz Science and Technology*, vol. 7, no. 5, pp. 572–581, 2017.

[27] A. Bisognin, N. Nachabe, C. Luxey, F. Gianesello, D. Gloria, J. R. Costa, C. A. Fernandes, Y. Alvarez, A. Arboleya-Arboleya, J. Laviada, F. Las-Heras, N. Dolatsha, B. Grave, M. Sawaby, and A. Arbabian, "Ball grid array module with integrated shaped lens for 5G backhaul/fronthaul communications in F-Band," *IEEE Transactions on Antennas and Propagation*, vol. 65, no. 12, pp. 6380–6394, 2017.

[28] S. Li, Z. Zhang, and G. M. Rebeiz, "An eight-element 136–147 GHz wafer-scale phased-array transmitter with 32 dBm peak EIRP and >f16 Gbps 16QAM and 64QAM operation," *IEEE Journal of Solid-State Circuits*, vol. 57, no. 6, pp. 1635–1648, 2022.

[29] J. C. F. Zandboer, G. Federico, U. Johannsen, and A. Bart Smolders, "A review on antenna technology developments for sub-thz wireless communication: Application, challenges and opportunities," *IEEE Open Journal of Antennas and Propagation*, vol. 6, no. 3, pp. 645–663, 2025.

[30] A. Singh, M. Sayginer, M. J. Holyoak, J. Weiner, J. Kimionis, M. Elkhouly, Y. Baeyens, and S. Shahramian, "A D-Band radio-on-glass module for spectrally-efficient and low-cost wireless backhaul," in *2020 IEEE Radio Frequency Integrated Circuits Symposium (RFIC)*, 2020, pp. 99–102.

[31] M. G. L. Frecassetti, J. F. Sevillano, D. del Río, M. I. Saglam, A. Lamminen, and V. Ermolov, "D-band backhaul and fronthaul solutions for 5g radio access network," in *2022 52nd European Microwave Conference (EuMC)*, 2022, pp. 772–775.

[32] A. Bisognin, N. Nachabe, C. Luxey, F. Gianesello, D. Gloria, J. R. Costa, C. A. Fernandes, Y. Alvarez, A. Arboleya-Arboleya, J. Laviada, F. Las-Heras, N. Dolatsha, B. Grave, M. Sawaby, and A. Arbabian, "Ball grid array module with integrated shaped lens for 5g backhaul/fronthaul communications in f-band," *IEEE Transactions on Antennas and Propagation*, vol. 65, no. 12, pp. 6380–6394, 2017.

[33] S. van Berkel, E. S. Malotaux, C. De Martino, M. Spirito, D. Cavallo, A. Neto, and N. Llombart, "Wideband double leaky slot lens antennas in cmos technology at submillimeter wavelengths," *IEEE Transactions on Terahertz Science and Technology*, vol. 10, no. 5, pp. 540–553, 2020.

[34] Z. Zheng, Y. Zhang, L. Shi, L. Wu, and J.-F. Mao, "An overview of probe-based millimeter-wave/terahertz far-field antenna measurement setups [measurements corner]," *IEEE Antennas and Propagation Magazine*, vol. 63, no. 2, pp. 63–118, 2021.

[35] N. Llombart, D. Emer, M. A. Campo, and E. McCune, "Fly's eye spherical antenna system for future Tbps wireless communications," in *The 11th European Conference on Antennas and Propagation (EuCAP 2017), (Paris, France)*, March. 2017.

[36] M. Arias Campo, K. Holc, R. Weber, C. De Martino, M. Spirito, A. Leuther, S. Bruni, and N. Llombart, "H-Band quartz-silicon leaky-wave lens with airbridge interconnect to GaAs front-end," *IEEE Transactions on Terahertz Science and Technology*, vol. 11, no. 3, pp. 297–309, 2021.

[37] J. Romeu, S. Blanch, L. Pradell, A. Barlabé, J.-M. Rius, M. Albert-Gali, L. Jofre-Roca, C. Mazzucco, and R. Flamini, "Lens-based switched-beam an-

tenna for a 5G smart repeater," *IEEE Antennas and Wireless Propagation Letters*, vol. 22, no. 10, pp. 2482–2486, 2023.

[38] O. Yurduseven, N. Llombart Juan, and A. Neto, "A dual-polarized leaky lens antenna for wideband focal plane arrays," *IEEE Transactions on Antennas and Propagation*, vol. 64, no. 8, pp. 3330–3337, 2016.

[39] "PREPERM low loss dielectric thermoplastics," accessed 2023-11-15. [Online]. Available: https://www.avient.com/products/engineered-polymer-formulations/conductive-signal-radiation-shielding-formulations/preperm-low-loss-dielectric-thermoplastics

[40] A. Paraskevopoulos, F. Maggiorelli, I. Gashi, C. D. Giovampaola, M. Albani, and S. Maci, "3-D printed all-dielectric GRIN lens antenna with an integrated feeder," *IEEE Open Journal of Antennas and Propagation*, vol. 4, pp. 528–536, 2023.

[41] S. Bosma, A. Neto, and N. Llombart, "On the near-field spherical wave formation in resonant leaky-wave antennas: Application to small lens design," *IEEE Transactions on Antennas and Propagation*, vol. 70, no. 2, pp. 801–812, 2022.

[42] N. van Rooijen, M. Alonso delPino, M. Spirito, and N. Llombart, "Core-shell leaky-wave lens antenna for 150GHz fly's eye communication systems," in *2022 47th International Conference on Infrared, Millimeter and Terahertz Waves (IRMMW-THz)*. IEEE, 2022, pp. 1–2.

[43] N. van Rooijen, M. Alonso-delPino, J. Bueno, M. Spirito, and N. Llombart, "Electrically small high permittivity lens antenna using artificially loaded thermoplastics at 170 GHz," in *2023 48th International Conference on Infrared, Millimeter, and Terahertz Waves (IRMMW-THz)*. IEEE, 2023, pp. 1–2.

[44] A. Ludwig, "The definition of cross polarization," *IEEE Transactions on Antennas and Propagation*, vol. 21, no. 1, pp. 116–119, 1973.

[45] D. R. Jackson, C. Caloz, and T. Itoh, "Leaky-wave antennas," *Proceedings of the IEEE*, vol. 100, no. 7, pp. 2194–2206, 2012.

[46] N. Llombart, G. Chattopadhyay, A. Skalare, and I. Mehdi, "Novel terahertz antenna based on a silicon lens fed by a leaky wave enhanced waveguide," *IEEE Transactions on Antennas and Propagation*, vol. 59, no. 6, pp. 2160–2168, 2011.

[47] N. Llombart, A. Neto, G. Gerini, M. Bonnedal, and P. De Maagt, "Impact of mutual coupling in leaky wave enhanced imaging arrays," *IEEE Transactions on Antennas and Propagation*, vol. 56, no. 4, pp. 1201–1206, 2008.

[48] H. Zhang, S. O. Dabironezare, G. Carluccio, A. Neto, and N. Llombart, "A Fourier optics tool to derive the plane wave spectrum of quasi-optical systems [EM programmer's notebook]," *IEEE Antennas and Propagation Magazine*, vol. 63, no. 1, pp. 103–116, 2021.

[49] N. T. Nguyen, N. Delhote, M. Ettorre, D. Baillargeat, L. Le Coq, and R. Sauleau, "Design and characterization of 60-GHz integrated lens antennas fabricated through ceramic stereolithography," *IEEE Transactions on Antennas and Propagation*, vol. 58, no. 8, pp. 2757–2762, 2010.

[50] S. L. van Berkel, A. Garufo, N. Llombart, and A. Neto, "A quasi-analytical tool for the characterization of transmission lines at high frequencies [EM programmer's notebook]," *IEEE Antennas and Propagation Magazine*, vol. 58, no. 3, pp. 82–90, 2016.

[51] L. Ferrari, O. Yurduseven, N. Llombart, S. J. C. Yates, J. Bueno, V. Murugesan, D. J. Thoen, A. Endo, A. M. Baryshev, and J. J. A. Baselmans, "Antenna coupled MKID performance verification at 850 GHz for large format astrophysics arrays," *IEEE Transactions on Terahertz Science and Technology*, vol. 8, no. 1, pp. 127–139, 2018.

[52] P. Focardi, W. McGrath, and A. Neto, "Design guidelines for terahertz mixers and detectors," *IEEE Transactions on Microwave Theory and Techniques*, vol. 53, no. 5, pp. 1653–1661, 2005.

[53] A. Garufo, P. M. Sberna, G. Carluccio, J. R. Freeman, D. R. Bacon, L. Li, J. Bueno, J. J. A. Baselmans, E. H. Linfield, A. G. Davies, N. Llombart, and A. Neto, "A connected array of coherent photoconductive pulsed sources to generate mw average power in the submillimeter wavelength band," *IEEE Transactions on Terahertz Science and Technology*, vol. 9, no. 3, pp. 221–236, 2019.

[54] T. Chaloun, S. Brandl, N. Ambrosius, K. Kröhnert, H. Maune, and C. Waldschmidt, "RF glass technology is going mainstream: Review and future applications," *IEEE Journal of Microwaves*, vol. 3, no. 2, pp. 783–799, 2023.

[55] H. Zhang, S. O. Dabironezare, J. J. A. Basemmans, and N. Llombart, "Focal plane array of shaped quartz lenses for wide field-of-view sub-millimeter imaging systems," *IEEE Transactions on Antennas and Propagation*, vol. Accepted, 2023.

[56] S. Bosma, N. Van Rooijen, M. Alonso-Delpino, M. Spirito, and N. Llombart, "First demonstration of dynamic high-gain beam steering with a scanning lens phased array," *IEEE Journal of Microwaves*, vol. 2, no. 3, pp. 419–428, 2022.

[57] S. Zhang, R. K. Arya, W. G. Whittow, D. Cadman, R. Mittra, and J. C. Vardaxoglou, "Ultra-wideband flat metamaterial grin lenses assisted with additive manufacturing technique," *IEEE Transactions on Antennas and Propagation*, vol. 69, no. 7, pp. 3788–3799, 2021.

[58] A. Paraskevopoulos, F. Maggiorelli, I. Gashi, C. D. Giovampaola, M. Albani, and S. Maci, "3-d printed all-dielectric grin lens antenna with an integrated feeder," *IEEE Open Journal of Antennas and Propagation*, vol. 4, pp. 528–536, 2023.

[59] Y. Guo, F. Meng, K. Ma, J. Ma, and Y. Luo, "A terahertz wide-angle beam-steering 3d-printed dual-polarized grin lens with planar focal surface," *IEEE Transactions on Terahertz Science and Technology*, vol. 15, no. 3, pp. 519–525, 2025.

[60] P. Kaděra, J. Sánchez-Pastor, M. Sakaki, R. Jakoby, N. Benson, A. Jiménez-Sáez, and J. Lacik, "Alumina 3-d printed wide-angle partial maxwell fish-eye lens antenna," *IEEE Antennas and Wireless Propagation Letters*, vol. 23, no. 7, pp. 2051–2055, 2024.

[61] J. Chen, S. X. Huang, K. F. Chan, G. Wu, and C. H. Chan, "3d-printed aberration-free terahertz metalens for ultra-broadband achromatic super-resolution wide-angle imaging with high numerical aperture," *Nat Commun*, vol. 16, no. 363, 2025.

[62] M. Imbert, A. Papió, F. De Flaviis, L. Jofre, and J. Romeu, "Design and performance evaluation of a dielectric flat lens antenna for millimeter-wave applications," *IEEE Antennas and Wireless Propagation Letters*, vol. 14, pp. 342–345, 2015.

[63] C. M. Coco Martin, W. Hu, and D. Cavallo, "Design of wideband flat artificial dielectric lenses at mmwave frequencies," *IEEE Transactions on Antennas and Propagation*, vol. 72, no. 2, pp. 1418–1428, 2024.

[64] N. v. Rooijen, M. Alonso-delPino, J. Bueno, A. Bechrakis Triantafyllos, P. M. Sberna, M. Spirito, and N. Llombart, "A core-shell lens for antenna on-package integration at d-band," *IEEE Transactions on Antennas and Propagation*, vol. 72, no. 8, pp. 6195–6208, 2024.

[65] W. Hu, C. M. Coco Martin, and D. Cavallo, "Design formulas for flat gradient index lenses with planar or spherical output wavefront," *IEEE Transactions on Antennas and Propagation*, vol. 72, no. 3, pp. 2555–2563, 2024.

[66] F. Maggiorelli, A. Paraskevopoulos, J. C. Vardaxoglou, M. Albani, and S. Maci, "Profile inversion and closed form formulation of compact grin lenses," *IEEE Open Journal of Antennas and Propagation*, vol. 2, pp. 315–325, 2021.

[67] D. Filipovic, S. Gearhart, and G. Rebeiz, "Double-slot antennas on extended hemispherical and elliptical silicon dielectric lenses," *IEEE Transactions on Microwave Theory and Techniques*, vol. 41, no. 10, pp. 1738–1749, 1993.

[68] M. G. L. Frecassetti, J. F. Sevillano, D. del Río, M. I. Saglam, A. Lamminen, and V. Ermolov, "D-band backhaul and fronthaul solutions for 5g radio access network," in *2022 52nd European Microwave Conference (EuMC)*, 2022, pp. 772–775.

[69] G. Engen and C. Hoer, "Thru-reflect-line: An improved technique for calibrating the dual six-port automatic network analyzer," *IEEE Transactions on Microwave Theory and Techniques*, vol. 27, no. 12, pp. 987–993, 1979.

[70] D. F. Williams, P. Corson, J. Sharma, H. Krishnaswamy, W. Tai, Z. George, D. Ricketts, P. Watson, E. Dacquay, and S. P. Voinigescu, "Calibration-kit design for millimeter-wave silicon integrated circuits," *IEEE Transactions on Microwave Theory and Techniques*, vol. 61, no. 7, pp. 2685–2694, 2013.

[71] S. Padmanabhan, L. Dunleavy, J. Daniel, A. Rodriguez, and P. Kirby, "Broadband space conservative on-wafer network analyzer calibrations with more complex load and thru models," *IEEE Transactions on Microwave Theory and Techniques*, vol. 54, no. 9, pp. 3583–3593, 2006.

[72] H. Xu and E. Kasper, "A de-embedding procedure for one-port active mm-wave devices," in *2010 Topical Meeting on Silicon Monolithic Integrated Circuits in RF Systems (SiRF)*, 2010, pp. 37–40.

[73] "IEEE standard test procedures for antennas," *ANSI/IEEE Std 149-1979*, pp. 1–144, 1979.

[74] E. Gandini, A. Tamminen, A. Luukanen, and N. Llombart, "Wide field of view inversely magnified dual-lens for near-field submillimeter wavelength imagers," *IEEE Transactions on Antennas and Propagation*, vol. 66, no. 2, pp. 541–549, 2018.

[75] C.-Y. E. Tong, K. Carter, and J. Connors, "Quasi-optical characterization of low-loss polymers at 300 ghz for vacuum window applications," *IEEE Transactions on Terahertz Science and Technology*, vol. 10, no. 6, pp. 713–720, 2020.

[76] A. Souliman, M. Kahl, D. Stock, M. Möller, B. Engel, and P. H. Bolívar, "Defect detection in bidirectional glass fabric reinforced thermoplastics based on 3-d-thz imaging," *IEEE Transactions on Terahertz Science and Technology*, vol. 13, no. 3, pp. 209–220, 2023.

[77] F. Taleb, G. G. Hernandez-Cardoso, E. Castro-Camus, and M. Koch, "Characterization of building materials for thz communications," in *2021 46th International Conference on Infrared, Millimeter and Terahertz Waves (IRMMW-THz)*, 2021, pp. 1–1.

[78] D. Ghodgaonkar, V. Varadan, and V. Varadan, "Free-space measurement of complex permittivity and complex permeability of magnetic materials at microwave frequencies," *IEEE Transactions on Instrumentation and Measurement*, vol. 39, no. 2, pp. 387–394, 1990.

[79] Y. Wang, X. Shang, N. M. Ridler, M. Naftaly, A. I. Dimitriadis, T. Huang, and W. Wu, "Material measurements using vna-based material characterization kits subject to thru-reflect-line calibration," *IEEE Transactions on Terahertz Science and Technology*, vol. 10, no. 5, pp. 466–473, 2020.

[80] S. Sahin, N. K. Nahar, and K. Sertel, "A simplified nicolson–ross–weir method for material characterization using single-port measurements," *IEEE Transactions on Terahertz Science and Technology*, vol. 10, no. 4, pp. 404–410, 2020.

[81] J. Lee, M. Fujita, and M. Kim, "Characterization of antireflection absorber films using wr-3.4 waveguide fixtures," *IEEE Transactions on Terahertz Science and Technology*, vol. 13, no. 5, pp. 565–568, 2023.

[82] D. Bourreau, A. Peden, and S. Le Maguer, "A quasi-optical free-space measurement setup without time-domain gating for material characterization in the *w*-band," *IEEE Transactions on Instrumentation and Measurement*, vol. 55, no. 6, pp. 2022–2028, 2006.

[83] N. I. Lesack, N. V. Fredeen, A. Jirasek, and J. F. Holzman, "A methodology for dynamic material characterizations via terahertz time-domain spectroscopy," *IEEE Transactions on Terahertz Science and Technology*, vol. 10, no. 3, pp. 282–291, 2020.

[84] D. Liu, T. Lu, and F. Qi, "A reliable method for removing fabry–perot effect in material characterization with terahertz time-domain spectroscopy," *IEEE Transactions on Terahertz Science and Technology*, vol. 10, no. 5, pp. 443–452, 2020.

[85] Z. Akhter and M. J. Akhtar, "Free-space time domain position insensitive technique for simultaneous measurement of complex permittivity and thickness of

lossy dielectric samples," *IEEE Transactions on Instrumentation and Measurement*, vol. 65, no. 10, pp. 2394–2405, 2016.

[86] J. A. Hejase, E. J. Rothwell, and P. Chahal, "A multiple angle method for thz time-domain material characterization," *IEEE Transactions on Terahertz Science and Technology*, vol. 3, no. 5, pp. 656–665, 2013.

[87] M. Mrnka, R. Appleby, and E. Saenz, "Accurate s-parameter modeling and material characterization in quasi-optical systems," *IEEE Transactions on Terahertz Science and Technology*, vol. 12, no. 2, pp. 199–210, 2022.

[88] N. Gagnon, J. Shaker, P. Berini, L. Roy, and A. Petosa, "Material characterization using a quasi-optical measurement system," *IEEE Transactions on Instrumentation and Measurement*, vol. 52, no. 2, pp. 333–336, 2003.

[89] G. Friedsam and E. Biebl, "A broadband free-space dielectric properties measurement system at millimeter wavelengths," *IEEE Transactions on Instrumentation and Measurement*, vol. 46, no. 2, pp. 515–518, 1997.

[90] A. Diepolder, M. Mueh, S. Brandl, P. Hinz, C. Waldschmidt, and C. Damm, "A novel rotation-based standardless calibration and characterization technique for free-space measurements of dielectric material," *IEEE Journal of Microwaves*, vol. 4, no. 1, pp. 56–68, 2024.

[91] A. Kazemipour, M. Hudlička, S.-K. Yee, M. A. Salhi, D. Allal, T. Kleine-Ostmann, and T. Schrader, "Design and calibration of a compact quasi-optical system for material characterization in millimeter/submillimeter wave domain," *IEEE Transactions on Instrumentation and Measurement*, vol. 64, no. 6, pp. 1438–1445, 2015.

[92] L. Dussopt, K. Medrar, and L. Marnat, "Millimeter-wave gaussian-beam transmitarray antennas for quasi-optical s -parameter characterization," *IEEE Transactions on Antennas and Propagation*, vol. 68, no. 2, pp. 850–858, 2020.

[93] L. Petersson and G. Smith, "An estimate of the error caused by the plane-wave approximation in free-space dielectric measurement systems," *IEEE Transactions on Antennas and Propagation*, vol. 50, no. 6, pp. 878–887, 2002.

[94] P. F. Goldsmith, "Quasioptical systems: Gaussian beam quasioptical propagation and applications," *IEEE Press Series on RF and Microwave Technology*, pp. 9–68, 1998.

[95] C. S. Williams, "Gaussian beam formulas from diffraction theory," *Appl. Opt.*, vol. 12, no. 4, pp. 872–876, Apr 1973. [Online]. Available: https://opg.optica.org/ao/abstract.cfm?URI=ao-12-4-872

[96] J. Bueno, S. Bosma, T. Bußkamp-Alda, M. Alonso-delPino, and N. Llombart, "Lossless matching layer for silicon lens arrays at 500 ghz using laser ablated structures," *IEEE Transactions on Terahertz Science and Technology*, vol. 12, no. 6, pp. 667–672, 2022.

[97] Z. Hatab, M. E. Gadringer, and W. Bösch, "Propagation of linear uncertainties through multiline thru-reflect-line calibration," *IEEE Transactions on Instrumentation and Measurement*, vol. 72, pp. 1–9, 2023.

[98] Z. Hatab, M. Gadringer, and W. Bösch, "Improving the reliability of the multiline trl calibration algorithm," in *2022 98th ARFTG Microwave Measurement Conference (ARFTG)*, 2022, pp. 1–5.

[99] D. Nikolayev, I. V. Soares, A. Mazzinghi, and A. K. Skrivervik, "Conformal beam-scanning arrays: Survey, analysis, and benchmarking," *IEEE Antennas and Propagation Magazine*, pp. 2–14, 2024.

[100] F. Rusek, D. Persson, B. K. Lau, E. G. Larsson, T. L. Marzetta, O. Edfors, and F. Tufvesson, "Scaling up mimo: Opportunities and challenges with very large arrays," *IEEE Signal Processing Magazine*, vol. 30, no. 1, pp. 40–60, 2013.

[101] E. G. Larsson, O. Edfors, F. Tufvesson, and T. L. Marzetta, "Massive mimo for next generation wireless systems," *IEEE Communications Magazine*, vol. 52, no. 2, pp. 186–195, 2014.

[102] S. Wang and G. M. Rebeiz, "Dual-band 28- and 39-ghz phased arrays for multi-standard 5g applications," *IEEE Transactions on Microwave Theory and Techniques*, vol. 71, no. 1, pp. 339–349, 2023.

[103] P. Afanasyev, S. Matitsine, V. Sledkov, P. Lagoiski, L. Matytsine, T. DeMarco, and T.-T. Chia, "Multi-beam luneburg lens antenna for cellular communications," in *2015 9th European Conference on Antennas and Propagation (EuCAP)*, 2015, pp. 1–4.

[104] R. Ozzola, D. Cavallo, A. Freni, N. Llombart, and A. Neto, "A benchmark for the number of independent line of sight links on a given volume platform," *IEEE Transactions on Antennas and Propagation*, vol. 70, no. 12, pp. 12 071–12 080, 2022.

[105] F. Puggelli, B. Biscontini, E. Martini, and S. Maci, "Maximizing independent channels and efficiency in bts array antennas via em degrees of freedom," *IEEE Transactions on Antennas and Propagation*, vol. 73, no. 6, pp. 3444–3458, 2025.

[106] A. Neto, A. F. Bernardis, D. Emer, A. Freni, and N. Llombart, "The observable field in complex scattering scenarios," *IEEE Transactions on Antennas and Propagation*, vol. 68, no. 7, pp. 5544–5555, 2020.

[107] L. Josefsson and P. Persson, 2006, pp. 1–13.

[108] C. Pfeiffer and J. Massman, "A uwb low-profile hemispherical array for wide angle scanning," *IEEE Transactions on Antennas and Propagation*, vol. 71, no. 1, pp. 508–517, 2023.

[109] B. Pavan Kumar, C. Kumar, V. Senthil Kumar, and V. V. Srinivasan, "Active spherical phased array design for satellite payload data transmission," *IEEE Transactions on Antennas and Propagation*, vol. 63, no. 11, pp. 4783–4791, 2015.

[110] P. Knott, "Design and experimental results of a spherical antenna array for a conformal array demonstrator," in *2007 2nd International ITG Conference on Antennas*, 2007, pp. 120–123.

[111] L. Marantis, E. De Witte, and P. V. Brennan, "Comparison of various spherical antenna array element distributions," in *2009 3rd European Conference on Antennas and Propagation*, 2009, pp. 2980–2984.

[112] R. J. A. L. Yuanpeng, L. Ting-Uei and X. Y. Min, "Extending goldberg's method to parametrize and control the geometry of goldberg polyhedra," *R. Soc. Open Sci.*, vol. 9:220675, 2022.

[113] M. Goldberg, "A class of multi-symmetric polyhedra," *Tohoku Mathematical Journal, First Series*, vol. 43, pp. 104–108, 1937.

[114] R. Warrier, "Max inscribed circle," MATLAB Central File Exchange. Retrieved June 26, 202, 2025. [Online]. Available: https://www.mathworks.com/matlabcentral/fileexchange/71995-max_inscribed_circle

[115] S. Rao, L. Shafai, and S. Sharma, *Handbook of Reflector Antennas and Feed Systems Volume III: Applications of Reflectors*. Artech House, 2013.

[116] C. E. Shannon, "A mathematical theory of communication," *The Bell System Technical Journal*, vol. 27, no. 3, pp. 379–423, 1948.

[117] N. B. Plug, J. Tan, S. Bosma, G. Carluccio, A. Neto, and N. Llombart, "Optimal current distributions for antenna arrays in radiative near-field communication links," *IEEE Open Journal of Antennas and Propagation*, pp. 1–1, 2025.

[118] W. T. Khan, A. C. Ulusoy, R. L. Schmid, and J. Papapolymerou, "Characterization of a low-loss and wide-band (dc to 170 ghz) flip-chip interconnect on an organic substrate," in *2014 IEEE MTT-S International Microwave Symposium (IMS2014)*, 2014, pp. 1–4.

[119] N. G. Weimann, S. Monayakul, S. Sinha, F.-J. Schmückle, M. Hrobak, D. Stoppel, W. John, O. Krüger, R. Doerner, B. Janke, V. Krozer, and W. Heinrich, "Manufacturable low-cost flip-chip mounting technology for 300–500-ghz assemblies," *IEEE Transactions on Components, Packaging and Manufacturing Technology*, vol. 7, no. 4, pp. 494–501, 2017.

[120] S. Monayakul, S. Sinha, C.-T. Wang, N. Weimann, F. J. Schmückle, M. Hrobak, V. Krozer, W. John, L. Weixelbaum, P. Wolter, O. Krüger, and W. Heinrich, "Flip-chip interconnects for 250 ghz modules," *IEEE Microwave and Wireless Components Letters*, vol. 25, no. 6, pp. 358–360, 2015.

[121] H.-C. Lu, C.-C. Kuo, P.-A. Lin, C.-F. Tai, Y.-L. Chang, Y.-S. Jiang, J.-H. Tsai, Y.-M. Hsin, and H. Wang, "Flip-chip-assembled *w*-band cmos chip modules on ceramic integrated passive device with transition compensation for millimeter-wave system-in-package integration," *IEEE Transactions on Microwave Theory and Techniques*, vol. 60, no. 3, pp. 766–777, 2012.

[122] S. Yu, N. Kou, J. Jiang, Z. Ding, and Z. Zhang, "Beam steering of orbital angular momentum vortex waves with spherical conformal array," *IEEE Antennas and Wireless Propagation Letters*, vol. 20, no. 7, pp. 1244–1248, 2021.

[123] Wikipedia, "List of geodesic polyhedra and goldberg polyhedra," https://en.wikipedia.org/wiki/List_of_geodesic_polyhedra_and_Goldberg_polyhedra, accessed: 2024-9-13.

[124] H. Friis, "A note on a simple transmission formula," *Proceedings of the IRE*, vol. 34, no. 5, pp. 254–256, 1946.

[125] D. Bourreau, A. Peden, and S. Le Maguer, "A quasi-optical free-space measurement setup without time-domain gating for material characterization in the *w*-band," *IEEE Transactions on Instrumentation and Measurement*, vol. 55, no. 6, pp. 2022–2028, 2006.

Acknowledgements

This thesis could not have been created without the help of a great number of great people. Not only could I rely upon the help, expertise and supervision of many colleagues at the TU Delft, I have also been fortunate enough to be surrounded by supportive family and friends.

First, I want to thank my promotor, prof. dr. ir. Nuria Llombart. Not only for your great expertise in anything related to the field of antennas, but also for your patience and willingness to guide me through this inspiring field of engineering and art. The way you dedicate time and effort to your PhD students despite your busy time schedule is a source of admiration for all.

Next, I offer my great thanks to my daily supervisor dr. ir. Maria Alonso-DelPino. We have spent countless hours working on all elements of this thesis. I greatly admire your 'jack of all trades' knowledge. From writing research papers, designing antennas, mechanical modeling or many other aspects of electrical engineering, you were always there to help as a great mentor.

The Mediterranean supervisory team would not be complete without dr. ir. Marco Spirito. Your critical thinking, reaching into the far corners of measurement and characterization, has no doubt had a large impact on this thesis. Your passion in the art of measurement is unrivaled. I remember my first time walking into the 'EKL lab', entering a complex and mysterious world full of noisy equipment (literally and figuratively) and the fascinating interaction between mathematics and measurements. These lab efforts have been invaluable in translating the abstract designs into working devices. All in all, I feel very fortunate to have had the three of you as my supervisory team.

This list would not be complete without offering my gratitude towards Ir. Ulrik Imberg. The frequent meetings we have had have helped me keep the PhD in track, and have bolstered a collaborative relationship. Furthermore, the help from CITC, in particular Sander Dorrestein and Francesa Chiappini, has been invaluable towards the sections relating to the front-end integration. My gratitude also goes to dr. ir. S. Bosma, who has introduced me to the world of antenna science. Whilst guiding me

through the COVID-19 era, his work and friendliness have inspired me to pursue a PhD myself. I hope that, perhaps one day, we could join forces again.

My deepest gratitude goes to all my colleagues at the Terahertz Sensing Group. With the help of prof. dr. A. Neto and many others, the coffee corner at the 18^{th} floor was always a place where the engineering work could be left aside for a while, and the serious and not-so serious aspects of life would be discussed. Although a humble place (I hope to erase the coffee bucket from memory soon), I hold fond memories of the breaks there. I am also indebted to the excellent quality of education and the nurturing intellectual culture found within the group. To all the co-authors found in the list of publications, it has been a pleasure venturing in this antenna world together.

I also thank the Terahertz Sensing group for all the conferences and courses that we have been to. Without a doubt, these voyages that we have embarked upon together have been one of the great perks of the PhD life. The traveling has been a source of many adventures and inspiration. The EuCAP in Madrid has been an amazing time, and demonstrated that human perseverance can triumph over lack of sleep. I thank in particular Dr. Martijn Sr. and Caspar for the intellectual advances made during the cultural nights in Florence and Glasgow.

Furthermore, I would like to thank dr. ir. Juan Bueno for his role in being a lab manager, PhD counselor and life coach. There was no lab task that 'Juandalf the Grey' could not overcome. But also outside the lab, I thank you for all the nice conversations we have had about life inside and outside of engineering. Dr. ir. Paolo Sberna, your help, sense of humor, clean-room skills, and BBQ wizardry have been vital ingredients to this thesis.

I also would like to thank Jeroen, Bert, Leon and their team of skilled technicians from the mechanical workshop DEMO at the TU Delft. Visiting their office has always been an insightful journey into a whole other scientific discipline, where computer-aided designs could be transformed into real-life prototypes. I realize that the designs and incredible tolerances that we requested would have been outright rejected at other workshops. However, DEMO's expertise and pragmatism have been critical to the success of this thesis.

My friends from *t 'Zoldertje*, you have provided the foundations upon which this thesis is built. Our (near) weekly meetings and yearly travels have been essential to refresh the mind, and maintain a healthy balance. I hope we can continue our flourishing friendship until we join again in the 'Singelhof'.

To my family (and roommates) at the Stationsstraat and beyond. Thank you for your patience in these abstract times. I would not be here without you.

Nick van Rooijen
Delft, July 2025

About the Author

Nick van Rooijen was born on November 25th, 1995 in Delft, The Netherlands. He received his B.Sc degree in electrical engineering from the Eindhoven University of Technology in 2019, and the M.Sc. degree (cum laude) in electrical engineering from the Delft University of Technology (TU Delft), Delft, The Netherlands, in 2021. During his master's, he worked on a first-time demonstration of a high frequency scanning-lens phased-array.

In July 2021, he started pursuing a Ph.D. degree with the Terahertz Sensing Group at the TU Delft. His PhD research focuses on the development of a Fly's-eye lens array for high frequency communication and sensing applications. His research interests include the analysis, design, and measurement of integrated lens antennas. This work was supervised by prof. dr. Nuria Llombart, dr. Maria Alonso-delPino and dr. Marco Spirito.

His research work has led to the publication of 4 journal contributions, and 13 conference contributions.

Mr. van Rooijen was the co-recipient of the Best Theory And Design Antenna Paper Award and was also co-nominated for the Best Applied Technology Antenna Paper Award, both at the 16th European Conference on Antennas and Propagation (EuCAP) in 2022.

List of Publications

Journal Papers

J.1 S. Bosma, N. van Rooijen, M. Alonso-delPino, and N. Llombart, “A Wideband Leaky-Wave Lens Antenna with Annular Corrugations in the Ground Plane,” *IEEE Antennas and Wireless Propagation Letters*, vol. 21, no. 8, pp. 1649-1653, Aug. 2022, doi: 10.1109/LAWP.2022.3176884.

J.2 S. Bosma, N. Van Rooijen, M. Alonso-Delpino, M. Spirito and N. Llombart, "First Demonstration of Dynamic High-Gain Beam Steering With a Scanning Lens Phased Array," in *IEEE Journal of Microwaves*, vol. 2, no. 3, pp. 419-428, July 2022, doi: 10.1109/JMW.2022.3179953.

J.3 N. v. Rooijen et al., "A Core-Shell Lens for Antenna On-Package Integration at D-Band," in *IEEE Transactions on Antennas and Propagation*, vol. 72, no. 8, pp. 6195-6208, Aug. 2024, doi: 10.1109/TAP.2024.3417628.

J.4 N. v. Rooijen, M. Alonso-Delpino, J. Bueno and N. Llombart, "Flat Lens-in-Package Architecture Using Multi-Axis Machining in D-Band," in *IEEE Open Journal of Antennas and Propagation*, doi: 10.1109/OJAP.2025.3613605.

J.5 N. van Rooijen, M. Alonso-Delpino and N. Llombart, "Design of Near-Field Coupled Leaky-Wave Lens Antennas with Flat Interfaces for Material Characterization at Sub-THz Frequencies," in *IEEE Journal of Microwaves*, doi: 10.1109/JMW.2026.3668936, accepted

J.6 N. van Rooijen, A. Bechrakis Triantafyllos, M. Alonso-Delpino and N. Llombart, "On the Optimization of Spherically Conformal Fly-Eye's Lens Antenna Arrays using Goldberg Topologies and Field Matching Techniques," in *IEEE Transactions on Antennas and Propagation*, under review

Conference Papers

C.1 M. Alonso-delPino, N. van Rooijen, S. Bosma and N. Llombart, "A Wideband Corrugated Leaky-Wave Feed with Low Cross-Pol for High Efficiency Lens Illumination," in *15th European Conference on Antennas and Propagation (EuCAP)*, Düsseldorf, Germany, Mar. 22-26 2021.

C.2 S. Bosma, N. van Rooijen, M. Alonso-delPino and N. Llombart, "High Aperture Efficiency Plastic Lens Antenna for Scanning Lens Phased Array at 180 GHz," *2021 46th International Conference on Infrared, Millimeter and Terahertz Waves (IRMMW-THz)*, Chengdu, China, 2021, pp. 1-2, doi: 10.1109/IRMMW-THz50926.2021.9567550.

C.3 N. van Rooijen, M. Alonso-delPino, M. Spirito and N. Llombart, "Core-Shell Leaky-Wave Lens Antenna for 150GHz Fly's Eye Communication Systems," in *16th European Conference on Antennas and Propagation (EuCAP)*, Madrid, Spain, Mar. 27 - Apr. 1 2022.
Award for Best Antenna Theory and Design

C.4 S. Bosma, N. van Rooijen, M. Alonso-delPino, M. Spirito and N. Llombart, "On the Demonstration of Dynamic Beam-Steering with a Scanning Lens Phased Array at W-Band," in *16th European Conference on Antennas and Propagation (EuCAP)*, Madrid, Spain, Mar. 27 - Apr. 1 2022.
Finalist for Best Applied Technology Antenna Paper Award

C.5 S. Bosma, N. van Rooijen, M. Alonso-delPino, M. Spirito and N. Llombart, "W-Band Demonstration of Dynamic, High-Gain Beam Steering with a Scanning Lens Phased Array" in *47th International Conference on Infrared, Millimeter and Terahertz Waves (IRMMW-THz)*, Delft, Netherlands, IEEE, pp. 1-2, 28 Aug. - 2 Sep. 2022. DOI: 10.1109/IRMMW-THz50927.2022.9895677

C.6 N. van Rooijen, M. Alonso-delPino, M. Spirito and N. Llombart, "Core-Shell Leaky-Wave Lens Antenna for 150GHz Fly's Eye Communication Systems," in *47th International Conference on Infrared, Millimeter and Terahertz Waves (IRMMW-THz)*, Delft, Netherlands, IEEE, pp. 1-2, 28 Aug. - 2 Sep. 2022. DOI: 10.1109/IRMMW-THz50927.2022.9895815
Invited Keynote Session

C.7 M. Alonso-delPino, S. Bosma, N. van Rooijen, M. Spirito and N. Llombart, "On the Development of Scanning Lens Phased Arrays at 100 GHz," In *Proc. IEEE International Symposium on Antennas and Propagation*, Portland, OR, USA, 23-28 Jul. 2023.

C.8 N. van Rooijen, R. Bokhorst, J. Bueno, M. Spirito, N. LLombart and M. Alonso-delPino, "140-170GHz Integrated Core-Shell Lens Antenna Front-End for High-Speed Communications", in *Proc. 17th European Conference on Antennas and Propagation, (EuCAP)*, Florence, Italy, 26-31 of Mar. 2023

C.9 N. van Rooijen, M. Alonso-delPino, J. Bueno, M. Spirito and N. Llombart, "Electrically Small High Permittivity Lens Antenna Using Artificially Loaded Thermoplastics at 170 GHz" in *2023 48th International Conference on Infrared, Millimeter, and Terahertz Waves (IRMMW-THz)* Montreal, QC, Canada, 2023. DOI: 10.1109/IRMMW-THz57677.2023.10299096

C.10 N. van Rooijen, M. Alonso-delPino, J. Bueno, M. Spirito and N. Llombart, "Experimental Characterization of a Core-Shell Lens for Antenna On-Package Integration at D-Band," in *Proc. 18th European Conference on Antennas and Propagation, (EuCAP)*, Glasgow, UK, Mar. 17-22 2024.

C.11 N. van Rooijen, R. Bokhorst, S. Dorrestein, F. Chiappini, P. Sberna, N. Llombart, M. Spirito and M. Alonso-delPino, "A 2-Tier TRL Calibration Technique to Assess Flip-Chip Interconnects at D-Band" in *2024 103rd ARFTG Microwave Measurement Conference (ARFTG)*, Washington, DC, USA, Jun. 21 2024.

C.12 N. van Rooijen, M. Spirito, A. B. Triantafyllos, N. Llombart and M. Alonso-delPino, "A Near-Field Quasi-Optical Measurement Technique for Probe-Fed High-Gain Backside-Radiating Antennas," in *2024 IEEE/MTT-S International Microwave Symposium - IMS 2024*, Washington, DC, USA, 2024, pp. 904-907, doi: 10.1109/IMS40175.2024.10600366.

C.13 N. van Rooijen, M. Alonso-Delpino and N. Llombart, "Flat Lens Concept Using Multi-Axis Machining for D-Band Core-Shell Lens-In-Package Integration," in *The 20th European Conference on Antennas and Propagation (EuCAP 2025)*, (Stockholm, Sweden), pp. 3952-3956, Apr. 2025.

Co-Supervised Master Theses

T.1 Z. Gao, “Wideband Mixer EVM Characterization through a VNA Setup at Sub-THz Frequencies,” M.S. thesis, Fac. EEMCS, Delft Univ. Technol., Delft, The Netherlands, 2024.